DEVELOPMENT OF GENETICALLY ENCODED TEMPERATURE INDICATORS FOR INTRACELLULAR THERMOMETRY AT THE SUBCELLULAR LEVEL

BY

CONG QUANG VU

SEPTEMBER 2021

A THESIS SUBMITTED TO

GRADUATE SCHOOL OF FRONTIER BIOSCIENCES

OSAKA UNIVERSITY FOR

THE DEGREE OF

DOCTOR OF PHILOSOPHY

ACADEMIC YEAR 2021

ABSTRACT

Genetically encoded temperature indicators (GETIs) allow the measurement of temperature dynamics at a subcellular resolution in live cells. However, GETIs have suffered from low temperature sensitivity when comparing to other nanothermometers, e.g., chemical-based fluorescent nanothermometers. To clearly visualize heat production from a biological process, it is highly desirable to develop GETIs that exhibit high temperature sensitivity for accurate temperature measurement as well as high specificity to temperature. In this thesis, I present two GETIs: (1) **E**lastin-**L**ike **P**olypeptide based **TEMP**erature indicator (**ELP-TEMP**) with the highest ever temperature sensitivity among the existing fluorescent nanothermometers, and (2) **B**lue-excited **g**enetically encoded **TEMP**erature indicator (**B-gTEMP**) that responded specifically to the temperature. ELP-TEMP is comprised of a temperature-responsive elastin-like polypeptide (ELP) fused with a cyan fluorescent protein (FP), mTurquoise2 (mT), and a yellow FP, mVenus (mV), as the donor and acceptor, respectively, of Förster resonance energy transfer (FRET). At elevated temperatures, the ELP moiety in ELP-TEMP undergoes a liquid-liquid phase transition leading to an increase in the FRET efficiency. In HeLa cells, ELP-TEMP responded to the temperature from 33 to 40 °C with a maximum temperature sensitivity of 45.1 ± 8.1 percent signal change per one degree Celsius (%/°C), which was the highest ever temperature sensitivity among the existing fluorescent nanothermometers. Although ELP-TEMP showed sensitivity not only to temperature but also to macromolecular crowding and self-concentration, I was able to correct the output of ELP-TEMP to achieve accurate temperature measurements at a subcellular resolution. I successfully applied ELP-TEMP to measure temperature changes in live cells induced by a local heat spot, even if the temperature difference was as small as <1°C, and to visualize heat production from Ca^{2+} influx induced by a chemical stimulation. Furthermore, I investigated temperatures in the nucleus and cytoplasm of live HeLa cells and found that their temperatures were almost the same within the temperature resolution of the measurement. This result would provide important information to shed light on a controversy about a discrepancy between a theoretical calculation and experimental measurements of intracellular temperature changes in single cells. On the other hand, B-gTEMP is a chimera of a green FP, mNeonGreen (mNG), showing low

temperature sensitivity of −0.7%/°C, and a red FP, tdTomato (tdT), showing the highest temperature sensitivity of −2.9%/°C among the examined FPs. B-gTEMP is the improved version of gTEMP, a GETI composed of a blue FP, Sirius, and a green FP, mT-Sapphire (mT-Sap). B-gTEMP showed a response in a wide temperature range of 15–50 °C with an average temperature sensitivity of 2.2 ± 1.2%/°C, comparable to that of gTEMP (2.6%/°C). Because B-gTEMP utilized a visible light excitation whereas gTEMP utilized ultraviolet excitation, temperature imaging with B-gTEMP showed lower phototoxicity and autofluorescence background than that of gTEMP. Additionally, B-gTEMP showed higher temperature resolution than gTEMP. Furthermore, temperature measurement with B-gTEMP was not affected by macromolecular crowding and self-concentration, which are the advantages over ELP-TEMP. Using B-gTEMP, I successfully monitored quick temperature rises induced by a local heat spot with a temporal resolution of 10 ms. In addition, I demonstrated the functionality of B-gTEMP in conventional temperature imaging to measure heat production in mitochondria induced by a chemical stimulation, and investigated temperature in the nucleus and cytoplasm of live HeLa cells, and found that the temperature was almost the same between them within the temperature resolution of the measurement, consistent with the result of ELP-TEMP. Altogether, ELP-TEMP and B-gTEMP are useful GETIs for future investigation of cell thermobiology.

TABLE OF CONTENTS

LIST OF ABBREVIATIONS

Symbols/Abbreviations	Terms
ATP	Adenosine triphosphate
BAT	Brown adipose tissue
B-gTEMP	Blue-excited genetically encoded temperature indicator
Ca^{2+}	Calcium ion
CNT	Carbon nanotube
crGE	A crowding indicator that is genetically-encoded
DMEM	Dulbeccco's modified Eagle's medium
ELP	Elastin-like polypeptide
ELP-REF	ELP-reference indicator
ELP-TEMP	ELP-based temperature indicator
FCCP	Carbonyl cyanide 4-(trifluoromethoxy)phenylhydrazone, an uncoupling reagent
FI	Fluorescence intensity
FNT	Fluorescence nanothermometry
FP	Fluorescent protein
FRET	Förster resonance energy transfer
GETI	Genetically encoded temperature indicator
GFP	Green fluorescent protein
gTEMP	Genetically encoded ratiometric fluorescent temperature indicator
LCST	Lower critical solution temperature

LED	Light emitting diode
mNG	mNeonGreen
mS	mScarlet
mT	mTurquoise2
mT-Sap	mT-Sapphire
mV	mVenus
NST	Non-shivering thermogenesis
PBS	Phosphate buffered saline solutions
ROI	Region of interest
SD	Standard deviation
tdT	tdTomato
T_t	Phase transition temperature
UCP	Uncoupling protein

CHAPTER 1
GENERAL INTRODUCTION

1.1 Temperature, an important parameter that governs biological processes

Temperature is a key physical parameter that is relevant to biological processes, because it can change the equilibrium and kinetics of biochemical reactions occurring in cells. Many biological activities such as cell division, gene expression, enzymatic reaction, and metabolism are accompanied by temperature changes[1-4]. Thus, it would be essential to understand how the temperature regulates the activities of cells, as a basic unit of life, that would help us to comprehend the effect of temperature on the whole human body.

Mammals including human need to maintain their body temperature despites the fluctuations of ambient temperature. For example, when exposing to a cold environment, the human body will quickly respond by shivering to generate heat, which has been known as shivering thermogenesis. However, this shivering is not last for long and may not be sufficient to heat up the whole body, and thus the body needs to produce heat by another mechanism so called non-shivering thermogenesis (NST)[4]. Brown adipose tissue (BAT) is arguably the main heat-producing tissue for NST that mediated by mitochondrial uncoupling protein 1 (UCP1)[5]. However, BAT is not present in all animals, e.g., birds or pigs[6], and it is just a minor component with a small amount in adult large mammals including human[6], suggesting that there may be other NST mechanisms that have not been discovered yet. Although heat production from muscle has been hypothesized as a NST mechanism, whether muscle can produce heat independently of contraction remains controversial[7]. Understanding the thermogenesis in the human body would be preciously beneficial, especially to the treatment of obesity, a worldwide epidemic caused by the imbalance between food intake and energy expenditure[8]. For example, utilization of BAT and molecular target drugs that activate BAT has been considered as a great strategy for the treatment of obesity[8,9].

Despite the importance of thermogenesis, the mechanism details behind heat production processes in organism and cells remain incompletely understood. One of the reasons may due to the lack of a tool to study the temperature-related processes at the cellular/subcellular level. Conventional thermometers (i.e., bar thermometers) are not

applicable for this purpose, because their size is larger than that of mammalian cells, whose size is generally 10–100 μm. Infrared thermometers are useful in large-scale temperature measurement from a distance, but having low spatial resolution that may not be sufficient to resolve the temperature measurement at a subcellular level[10]. Although micro-thermocouples have been applied to measure temperature inside cells, they are required the insertion into the cells that could damage cells, and the temperature readout is only at the contact site of the micro-thermocouple[11,12]. The limitation of classic thermometers has led to the requirement of a new method that can measure intracellular temperature at the cellular/subcellular level without interrupting cellular functions.

1.2 Fluorescence nanothermometry

Fluorescence nanothermometry (FNT) enables us to monitor temperature dynamics at a high spatial and temporal resolution inside live cells in a noninvasive manner. FNT uses a temperature-sensitive fluorescent indicator to measure the temperature through the fluorescence readout. Because the size of most fluorescent nanothermometers is in a scale of hundreds of nanometers to single molecules, fluorescent nanothermometers are useful to visualize temperature in live cells at a high spatial resolution[13,14]. In addition, because of their small sizes, they have a low heat capacity and thus minimally affect sample temperature to achieve temperature measurement with a rapid response and high accuracy. There have been efforts in developing fluorescent temperature indicators for FNT using different temperature-responsive materials such as fluorescent proteins (FPs)[15], chemical dyes[16], nanoparticles[17], nanodiamonds[18], polymers[19], and single-stranded DNA[20] (**Table 1**). Applications of FNT have led to exciting reports such as heterogeneous temperature distribution of neural cells[21], temperature difference between the nucleus and cytoplasm in COS7 cells[19] and HeLa cells[15,22], heterogeneous temperature distribution in mitochondria[19,23], hot mitochondria[24], and the low thermal conductivity in cells[25,26]. In addition, FNT enabled *in vivo* imaging for mapping intracellular temperature in live *C. elegans*[27], real-time monitoring of heat production in flight muscle of live *D. derbyana* beetles[17], and *in vivo* detection of ischemia[28], early-stage tumor[29], and inflammation-induced temperature increment in mice[30].

Table 1. List of some fluorescent nanothermometers for intracellular thermometry

Materials	Nanothermometers	Measurement method	Temperature range (°C)	$\|S_T\|$ (%/°C)*	Ref.
FPs	EGFP	Intensity	20–60	2.1	[3]
		Fluorescence polarization anisotropy	20–60	0.4	[31]
	tsGFP1	Ratio	35–40	3.9	[32]
	gTEMP	Ratio	5–50	2.6	[15]
	emGFP-Mito	Peak shift	23-39	2.2	[23]
Fluorescent dyes	ER thermo yellow	Intensity	32–37	3.9	[33]
	Mito thermo yellow	Intensity	37–42	2.0–2.8	*[16]*
	Mito-RTP	Ratio	25–45	2.7	*[34]*
	Mito-TEMP 2.0	Ratio	25–55	5.4	[35]
	Eu-TTA within micropipette	Intensity	25–50	2.7	[36]
	Thermosensitive nanovesicles	Intensity	20–30; 33–36; 35–40; 42–45; 51–55	10–22	[37]
Inorganic materials	Quantum dot (QD655)	Peak shift	30–40	6.2	[21]
	AuNCs	Lifetime	15–45	-	[38]
	NaYF4 nanothermometer	Ratio	25–46	1.9	[39]
	Nanodiamonds	Spin states with microwave excitations	-73–327	-	[18]
Polymers	FNT	Intensitiy	27–33	-	[40]

	FPT	Lifetime	20–50	4.8	[19]
	Walking nanothermometer	Ratio	20–60	2.2	[41]
	Ratiometric nanothermometer	Ratio	25–40	2.2	[42]
	Fluorescent thermometer nanosheets	Ratio	25–40	3.4	[43]
	Ultra-long-lived luminescent nanocapsule	Lifetime	20–45	7.5	[44]
DNA	L-MB	Intensity	25-55	-	[20]
	ssDNA FT	Ratio	0-100	7.0	[45]

*S_T: relative temperature sensitivity (see **Box 1** for more detail). Ref. stands for references.

1.2.1 Typical temperature-sensing strategies and designs of fluorescent nanothermometers

Fluorescence intensity

Fluorescence intensity (FI) based temperature measurement is arguably the most straightforward and versatile approach for developing nanothermometers (**Figure 1A**). The change of temperature can be directly measured from fluorescence changes, and thus allows temperature measurement at high-speed imaging with a conventional fluorescence microscope. This based on the fact that the FI is generally decreased as the temperature increased (see **Box 2**). A number of FI-based nanothermometers have been developed using different materials such as fluorescent dyes[16,33,36], polymers[40], DNA[20], and FPs[3]. However, this approach is only suitable for rough estimation of the temperature rises and falls. The FI-based nanothermometers may not be reliable for absolute temperature measurement, since the FI is dependent on the nanothermometer's concentration, inhomogeneous illumination and power of excitation light.

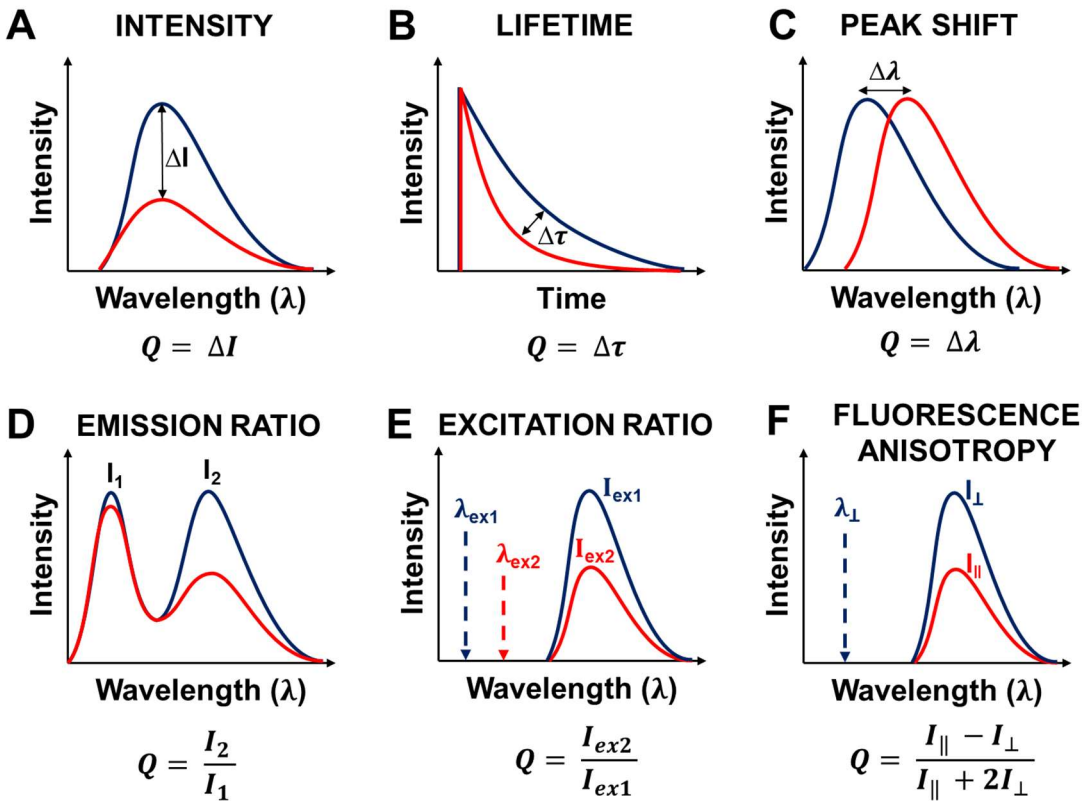

Figure 1. Schematic illustration of typical temperature-sensing mechanisms of fluorescent nanothermometers. (A) Intensity, (B) Lifetime, (C) Peak shift, (D) Emission ratio, (E) Excitation ratio, (F) Fluorescence anisotropy. Q represents experimental parameters used for temperature determination. Red and blue color represent high and low temperature, respectively.

Florescence lifetime

Fluorescence lifetime based nanothermmetry is also straightforward way for intracellular temperature measurement, because fluorescence lifetime is temperature-dependent (**Figure 1B**). Unlike intensity, fluorescence lifetime is independent on the concentration, providing concentration-independent readout. Serval fluorescence lifetime-based nanothermometers have been developed for FNT[19,38,44]. Despite the advantages, there are some limitations that would hinder this method for temperature measurement, e.g., fluorescence decay is often non-single component, fluorescence lifetime of some endogenous compounds such as NADH, FAD, etc. is similar to that of some nanothermometers[46], and the acquisition time of some lifetime-based nanothermometers

is slow, e.g. fluorescent nanogel thermometer (FNT) took 60 s for data collection of an image of 64x64 pixels[19]. In addition, fluorescence lifetime imaging microscopy (FLIM) may arguably less common than wide-field fluorescence microscopy in the laboratory.

Box 1: Terms of common parameters used in FNT.

In general, fluorescent nanothermometers are employed to measure temperature through changes in fluorescence intensity, fluorescence ratio, lifetime, peak shift, and fluorescence polarization anisotropy. These changes can be quantified as Q.

Absolute temperature sensitivity (S_A): the rate of changes of Q with temperature.

$$S_A = \left|\frac{\Delta Q}{\Delta T}\right|, \quad (1)$$

where Q is experimental parameters that corresponds to a change of temperature (T), and Δ represents a change of a parameter value. The unit of S_A is 1/°C or 1/K.

Relative temperature sensitivity (S_T): a parameter used in order to compare the temperature sensitivity with other nanothermometers.

$$S_T = \left|\frac{\Delta Q}{Q}\frac{1}{\Delta T}\right| \times 100(\%), \quad (2)$$

The unit of S_T is consistent as %/°C or %/K for all nanothermometers.

Temperature resolution (δT): the minimal temperature that can be resolved with a nanothermometer.

$$\delta T = \left|\frac{\Delta T}{\Delta Q}\right| \sigma(Q), \quad (3)$$

where $\sigma(Q)$ represents the standard deviation of an experimental parameter used for temperature determination. The unit of δT is °C or K.

Peak shift of the emission spectrum

In some semiconducting quantum dots (QDs)[21,47], the fluorescence peak emission is shifted, in which the bandgap of the QDs changes with temperature (**Figure 1C**). Unlike the intensity, spectral shift is independent on the QDs concentration, but showing a dependence on the particle size of the QDs[47]. Wild-type green FP (wt-GFP) was found to exhibit the temperature-induced spectral shift, which was suggested to be due to the change in hydrogen network of the chromophore with temperatures[23,48].

Box 2. Correlation between fluorescence intensity and temperature

In general, the FI of a fluorophore often decreases to an increase of temperature, which is most likely due to the decrease of fluorescence quantum yield, as the FI of a fluorophore is proportional to its fluorescence quantum yield. The fluorescence quantum yield, a ratio of the number of photons emitted to the number of photons absorbed, can be defined by:

$$QY = \frac{k_r}{k_r + k_{nr}}, \quad (4)$$

where QY is quantum yield, k_r and k_{nr} are the rate constants of radiative decay and non-radiative decay of the excited state, respectively. The decrease of fluorescence quantum yield with temperature is arguably due to the increase of k_{nr}[49,50]. Meng *et al.,* reported that increasing the temperature resulted in an increase of k_{nr} accompanied with a decrease of k_r, leading to the decrease of the fluorescence quantum yield of a fluorescent dye[51].

Emission and excitation ratios

A typical and common strategy for developing fluorescent nanothermometers is relied on emission ratio of two different fluorophores having different emission wavelengths and temperature sensitivities, i.e., one shows high temperature sensitivity corresponding to the temperature readout, and the other shows low temperature sensitivity as the internal reference (**Figure 1D**). Taking the emission ratio of two wavelengths can correct for the inhomogeneous distribution of the nanothermometers' concentration, resulting in absolute temperature measurement. In addition, if the two fluorescence compounds can be excited by a single excitation light, the two emission wavelengths can be simultaneously monitored by using a dual view optics[52], enabling high-speed imaging. Several ratiometric fluorescent nanothermometers have been reported including chemical dyes[34,35], nanoparticles[39,51], polymers[41-43], DNA[45], and FPs[15]. In a similar approach, some fluorophores, e.g., wt-GFP[32] can be excited by two different wavelengths showing different temperature dependence, so that excitation-based nanothermometers can be devised from excitation intensity ratio (**Figure 1E**).

Fluorescence anisotropy

Some fluorophores excited with vertically polarized light exhibit different fluorescence emission intensity in a parallel (∥) or perpendicular (⊥) to the direction of excitation light in a temperature dependence manner (**Figure 1F**). For example, green FP (GFP) has been utilized as a nanothermometers to measure intracellular temperature in live cells and a living organism using fluorescence polarization anisotropy[27,31].

1.2.2 Genetically encoded temperature indicators (GETIs)

Among the fluorescent nanothermometers, FP-based indicators can be expressed in target cells and tissues by transfection. These genetically encoded temperature indicators (GETIs) can specifically target to an organelle via fusion with a targeting peptide or protein. However, only a few of GETIs have been developed so far as follows. (1) Enhanced green FP (EGFP) based intensiometric nanothermometer[3], as the fluorescence emission of EGFP was reported to be inversely correlated with temperatures. Correction of photobleaching of EGFP was essentially required that would limit its application. In another approach, Donner *et al.* utilized EGFP for the measurement of fluorescence polarization anisotropy[31] for mapping intracellular temperature in live mammalian cells and *C. elegans*[27]. (2) GFP-based thermosensors (tsGFPs) were developed by flanking wild-type green FP (wt-GFP) with dual copies of the *Salmonella* thermosensing protein TlpA[32]. Upon temperature-dependent dimerization of TlpA, conformation change of the sandwiched wt-GFP led to a shift in its excitation peaks, giving a temperature readout. tsGFPs have been applied to visualize thermogenesis in brown adipocytes and skeletal muscle myotubes. (3) Genetically encoded ratiometric fluorescent temperature indicator (gTEMP)[15] that reported temperature with fluorescence intensity ratio between a temperature-sensitive blue FP, Sirius, and a temperature-less-sensitive green FP, mT-Sap. gTEMP showed a rapid response to temperature with a temporal resolution of 50 ms, and a wide detection temperature range from 5 to 50 °C. gTEMP has been demonstrated its temperature-sensing performance in measuring intracellular temperature rise in mitochondria, temperature difference between the nucleus and cytoplasm, and temperature in a living medaka embryo. Despite the advantages, the requirement of UV excitation (~370 nm) would limit the application of gTEMP for live biological samples

(see **Chapter 4** for more detail). (4) emGFP-Mito[23] by measuring the shift of fluorescence peak of Emerald green FP (em-GFP) in responding to temperature changes. The emGFP-Mito has been demonstrated to visualize heterogeneous temperature distribution in mitochondria and a temperature rise in mitochondria by treatment with a chemical stimulation. Recently, Maksimov *et al.* reported a new strategy to develop a GETI derived from the photoactive orange carotenoid protein, which showed a strong temperature dependence of photoconversion rates[53]. However, this work has not been completed and still under optimization. Although GETIs are advantageous for live cell imaging, their low temperature sensitivity (S_T, as defined in **Box 1)** including EGFP (S_T = 2.1%/°C[3]), EGFP in fluorescence polarization anisotropy (S_T = 0.4%/°C[31]), tsGFP1 (S_T = 3.9%/°C[32]); gTEMP (S_T = 2.6%/°C[15]), and emGFP-mito (S_T = 2.2%/°C[23]) is considered to be a main drawback of GETIs for FNT. Thus, it is desirable to develop a new GETI having high temperature sensitivity for accurate intracellular temperature measurement.

1.3 "The 10^5 gap issue" in single-cell thermometry

Although several studies applied FNT to measure intracellular temperature in single cells and reported heterogonous temperature distribution in non-stimulated cells[15,19,21-24], and temperature increase in mitochondria[15,19,23,24,32,35] or endoplasmic reticulum (ER)[33,36,54,55] by stimulating with a chemical drug, a theoretical calculation[56] suggested that intracellular temperature increment (ΔT) in single cells could not exceed 10^{-5} °C. This has led to a great controversy so called "the 10^5 gap issue" between the theoretical calculation and experimental measurements in single-cell thermometry[57-59]. This controversy was firstly proposed in 2014 by Baffou *et al.*[56], who criticized the temperature measurement with FNT reporting an endogenous heat production ΔT > 1 °C that would be more far unrealistic to their theoretical estimation. They estimated the expected temperature increase in single cells by a simple heat-diffusion equation in the steady state:

$$\Delta T = \frac{P}{\kappa L}, \qquad (5)$$

where ΔT is the temperature increase (in K), P is the power of the heat source (in Watts, W), κ is the thermal conductivity (in $Wm^{-1}K^{-1}$), and L is typical size of the heat source (in meter, m). Accordingly, for a cell with a typical length L = 10 μm with a typical power P = 100 pW (which was reported from a microcalorimetry measurement) in a watery

environment ($\kappa \sim 1$ W m^{-1} K^{-1}), temperature increase was expected to be $\Delta T \sim 10^{-5}$ °C. In response to the critique, Mori[58] and Ishiwata[57] group argued against the applicability of the heat diffusion equation in the steady state at submicroscopic scale, especially in living cells containing several biomolecular complexes. Additionally, the parameter values used in the calculation for heat source, thermal conductivity of cells, and the length scale of the heat source in the estimation of heat diffusion equation should be reconsidered to be more realistic. In reply, Baffou *et al.*[59] disputed the argument of Mori and Ishiwata group, and the controversy has still remained.

I am interested in "the 10^5 gap issue" and I hope I could partly contribute to find the answer of this controversy. I am curious whether single cells can produce heat in order to regulate their biological activities, and if they are, I question when, how, and how much heat can be produced in a single cell. I realize that the drawback of low temperature sensitivity of conventional GETIs may not be sufficient to clearly visualize a small heat production in cells. Thus, I aim to develop a highly-sensitive GETI to solve this limitation. In addition, I also performed characterization of B-gTEMP, which was developed by a former lab member, and demonstrated its performance of temperature imaging in live cells.

CHAPTER 2
DEVELOPMENT OF ELASTIN-LIKE POLYPEPTIDE BASED GENETICALLY ENCODED TEMPERATURE INDICATOR

2.1 Introduction

Elastin-like polypeptides (ELPs) are polypeptides that consist of a primary sequence of $(VPGXG)_n$, where X is a guest amino acid residue except proline[60] and n is the number of pentapeptide repeats[61]. One of their unique characteristics is the thermal responsiveness displaying the lower critical solution temperature (LCST) in an aqueous solution: they are in the soluble state below the transition temperature (T_t) whereas they undergo a self-assembly process to form coacervate at an elevated temperature above T_t[60,61]. The T_t of ELPs can be manipulated by changing the guest residue X and the number of the repeats n: T_t lowers as the guest residue X becomes more hydrophobic, and vice versa[62]; T_t lowers as the number of the repeats n becomes larger, and vice versa[61]. Additionally, ELPs can be genetically encoded and expressed in live cells. Thus, ELPs should be potential candidates as temperature-sensing domains for the development of GETIs.

Previously, Mackay *et al.* utilized ELPs fused with a green FP (GFP) to detect intracellular temperature through ELP coacervation as observed by fluorescence microscopy[63]. However, this approach was able to detect only a temperature at which the ELP converted into the coacervate, and thus, did not provide the quantitative measurement of temperature. Chen *et al.* reported an ELP labeled with a hydrophobicity-sensitive fluorescent dye, which showed high fluorescence upon the coacervation of ELP caused by the elevation of temperature above its T_t[64]. Because this approach needed fluorescence labeling of the ELP to produce the temperature indicator and its delivery into cells, the scope of the application was rather limited. To move a step forward from the ELP-derived fluorescent temperature indicators thus far, it is desirable to develop a novel GETI that takes the advantage of the highly temperature-sensitive behavior of ELPs to perform quantitative temperature measurement at a high accuracy, and is ready to be observed after expression in cells without any chemical modification.

Förster resonance energy transfer (FRET) has been extensively applied to the development of various types of genetically-encoded fluorescent indicators. A general design of genetically-encoded FRET-based indicators involves two FPs of different excitation and emission wavelengths as the donor and acceptor of FRET, and a sensor domain that detects a factor of interest, e.g., ions, macromolecular crowding, or temperature. Upon excitation of the donor, the excited-state energy is partly or entirely transferred from the donor to the acceptor to undergo fluorescence emission of the acceptor as well as that of the donor, depending on the FRET efficiency[65]. Because the FRET efficiency is dependent on parameters such as the distance and relative orientation between the donor and acceptor, if the conformation of the sensor domain changes upon the detection of a factor, the distance or the relative orientation is expected to change so that the FRET efficiency alters, leading to changes of the fluorescence intensities of the donor and acceptor. It should be noted that the ratio of the fluorescence intensities between the donor and acceptor can be a measure of the FRET efficiency, and thus, FRET-based indicators are useful to perform ratiometric imaging with the donor and acceptor fluorescence. In fact, a number of genetically encoded indicators have applied FRET to sense ions (Ca^{2+} [66], Mg^{2+} [67], K^{+} [68], and H^{+} [69]), membrane potential[70], and macromolecular crowding[71]. Thus, if donor and acceptor FPs are fused with an ELP, this fusion protein is most likely to show a large change of FRET efficiency in response to temperature changes around its T_t to achieve a high sensitivity to temperature.

Here, I aim to develop a GETI from an ELP and a FRET pair of a cyan FP, mTurquoise2 (mT)[72], and a yellow FP, mVenus (mV)[73]. The ELP moiety in the present GETI undergoes a phase transition around a physiological temperature of mammalian cells and this would lead to a large change of FRET efficiency, allowing quantitative temperature measurement in cells. I demonstrate its temperature-sensing performance to monitor quick temperature rises at a subcellular resolution caused by transient heat supply from a local heat, and to visualize heat production from Ca^{2+} influx induced by a chemical stimulation. In addition, I investigate temperatures in the nucleus and cytoplasm of live HeLa cells.

2.2 Materials and methods

Gene construction. I obtained plasmids harboring ELP genes from Addgene (ELP[V-60][74] containing the sequence of $(VPGVG)_{60}$, #67013; ELP[AV-60][74] containing the sequence $(VPGAG\text{-}VPGVG)_{30}$, #67012). To create a doubly repeated ELP[V-60] (ELP[V-60]-ELP[V-60]), I amplified the whole cDNA of ELP[V-60] with both forward and reverse primers containing a *Xho*I restriction enzyme site (*Xho*I-ELP[V-60]-*Xho*I). Meanwhile, I also amplified the cDNA of ELP[V-60] with a forward primer containing a *Sal*I site and a reverse primer containing a *EcoR*I site (*Sal*I-ELP[V-60]-*EcoR*I). I then ligated these two amplified fragments with the *Xho*I-*Sal*I restriction enzyme sites. Because the cut site of *Xho*I (C/TCGAG) and *Sal*I (G/TCGAC) produces compatible cohesive ends, their ligation product can be either GTCGAG or CTCGAC, which cannot be cut by either *Xho*I or *Sal*I restriction enzymes. To create ELP[AV-60]-ELP[AV-60], a similar procedure was conducted. To construct an ELP-TEMP gene, I enzymatically cut the whole cDNA of ELP[V-60]-ELP[V-60] with *Xho*I and *EcoR*I restriction enzymes (*Xho*I-ELP[V-60]-ELP[V-60]-*EcoR*I), and ligated with mVenus (mV) and mTurquoise2 (mT) genes at the 5'- and 3'-ends of the ELP[V-60]-ELP[V-60] gene, respectively. The restriction enzymes for the mV gene were *BamH*I and *Xho*I (*BamH*I-mV-*Xho*I), while those for the mT gene were *EcoR*I and *Hind*III (*EcoR*I-mT-*Hind*III). I then inserted the ELP-TEMP gene into the $pRSET_B$ vector (Invitrogen) for bacterial expression or the pcDNA3.1(-) vector (Invitrogen) for mammalian expression. To construct a reference indicator (ELP-REF), I replaced the ELP[V-60]-ELP[V-60] sequence in the ELP-TEMP gene with that of ELP[AV-60]-ELP[AV-60]. A plasmid containing a crowding indicator gene (crGE[71]) was a gift from Prof. Boersma. I transformed all the gene constructions into XL-10 Gold *E. coli* cells (200314, Agilent Technologies) and cultured in the Luria-Bertani (LB) medium with 100 μg/mL carbenicillin (Sigma-Aldrich) for 10–12 h at 37 °C, and then, I performed plasmid purification.

Protein purification. I transformed *E. coli* strain JM109(DE3) (P9801, Promega) with the $pRSET_B$ plasmid harboring ELP-TEMP or ELP-REF fused with an N-terminal polyhistidine tag by heat shock method at 42 °C for 45 s. I spread the transformants on an LB plate containing 100 μg/mL carbenicillin and incubated at 37 °C for overnight. I grew *E. coli* in a 200 mL LB medium containing 100 μg/mL carbenicillin at 23 °C for 3

days with gentle shaking at 120 rpm. I harvested the *E. coli* cells, suspended them in a phosphate buffered saline solution (PBS; T900, Takara Bio) containing a protease inhibitor cocktail (11873580001, Roche Diagnostics), and ultra-sonicated to lyse the cells. I subsequently applied the proteins on the Ni-NTA agarose (30230, Qiagen) and eluted them with a TN buffer (10 mM Tris-HCl and 150 mM NaCl, pH 8.0) supplemented with 200 mM imidazole (099-00013, FUJIFILM Wako). Finally, I exchanged the solvent of the protein solution with a PBS solution (pH 7.4) by applying on a PD-10 desalting column (17085101, GE Healthcare) equilibrated with the same buffer. I concentrated the protein by ultrafiltration using a filter with a molecular weight cut-off of 50 kDa (UFC803024, Amicon Ultra-4, Merck Millipore), quickly froze the protein solution in liquid nitrogen, and stored them at −80 °C.

Fluorescence spectroscopy measurement. I performed fluorescence spectroscopy measurements by an FP-750 spectrofluorometer (JASCO) equipped with a temperature controller unit (ETC-272T, JASCO). I diluted proteins in a PBS solution (T900, Takara Bio) and loaded into a quartz cuvette. I took 5 min to wait for temperature equilibration at each temperature point before starting measurement. The excitation wavelength was 430 nm.

To investigate the effect of macromolecular crowding, I dissolved ELP-TEMP in a PBS solution containing Ficoll PM70 (F2878, Sigma-Aldrich). To examine the effect of salts, I added $CaCl_2$, $MgCl_2$, or 1 mM EDTA to a PBS solution, where 1 mM EDTA was used to achieve the condition of 0 mM $CaCl_2$ or $MgCl_2$. For NaCl and KCl, I added a salt to a 10 mM sodium phosphate buffer (pH 7.4). For pH dependence measurement, I prepared a mixture of 30 mM trisodium citrate and 30 mM borax adjusted to pH 8.0, 7.0, 6.0, and 5.0 by adding HCl.

To measure the fluorescence of ELP-TEMP in a cell suspension, I suspended ~5 million HeLa cells expressing ELP-TEMP in 0.5 mL of a PBS solution, and measured the fluorescence by a fluorescence spectrophotometer (F-7000, Hitachi-Hightech). For background correction, I measured the baseline from a suspension containing ~5 million untransfected HeLa cells. The excitation wavelength was 430 nm.

Cell culture, transfection, and establishment of stable cell lines. I cultured HeLa cells in Dulbecco's modified Eagle medium (DMEM; D6046, Sigma-Aldrich) supplemented with 10% fetal bovine serum (FBS; Biowest) at 37 °C in a 5% CO_2 incubator. I seeded cells on in-house-made glass bottom dishes and grew up to 60–70% of cell confluence before performing transfection. For transfection, I mixed 2.0 μg of plasmids and 5.0 μg of polyethylenimine MAX (24765-1, Polysciences) in 200 μL of Opti-MEM medium (31985-070, Thermo Fisher Scientific), and incubated for 20 min at room temperature. Subsequently, I added the mixture to 1 mL of culture medium containing HeLa cells, and exchanged the culture medium at 6 h after the mixing. I cultured the cells for ~48 h and exchanged the medium to DMEM/F12 (11039-021, ThermoFisher Scientific) without phenol red before microscopy observation.

To establish a HeLa cell line stably expressing ELP-TEMP or ELP-REF, 2 days after transfection, I exchanged the culture medium with DMEM supplemented with 10% FBS and 500 μg/mL geneticin (G-418, 10131-035, Gibco). I kept culturing the cells until colonies formed. Finally, I isolated a fluorescent colony and grew up in the same medium to increase the cell number. After establishing the stable cell lines, I grew them with a DMEM medium containing 10% FBS and 200 μg/mL geneticin.

Cell imaging. I performed cell imaging with an inverted microscope (Ti-2, Nikon) equipped with a confocal unit (Dragonfly 200, Andor Technology), a microscope objective (CFI Plan Apochromat λ 60x Oil; numerical aperture, 1.40; Nikon), and a stage-top incubator with 5% CO2 supply (STXG-WSKMX, Tokai Hit). I used a 445 nm laser for excitation and collected the fluorescence emission through bandpass filters (ET480/40nm and ET540/30nm for mT and mV, respectively; Chroma). I captured the fluorescence images with an EMCCD camera (iXon Ultra, Andor Technology). The exposure time was 500 ms, and the binning size was 2×2 pixels. I measured fluorescence ratios of mV/mT cell by cell to calculate the average values and the standard deviation.

Western Blotting. I used stable HeLa cell lines expressing ELP-REF or ELP-TEMP. The indicators were detected with a primary anti-GFP (Rabbit pAb, Cat #598, MBL, dilution 1:1000) and a secondary anti-rabbit IgG HPR conjugation (W401B, Promega, dilution 1:1000). As a loading control, I used a primary anti-GAPDH (Mouse mAb, SC-32233,

Santa Cruz, dilution 1:1000) and a secondary anti-mouse IgG HPR conjugation (W402B, Promega, dilution 1:1000). For chemiluminescence detection, I used a kit of ECL prime Western Blotting detection regents (RPN2232, GE Healthcare).

Quick temperature rises with a local heat spot using carbon nanotubes (CNTs).
I prepared a suspension of 1 mg/mL multiwalled carbon nanotubes (CNTs) (average diameter, 170 nm; average length, 5–9 μm; 659258, Sigma-Aldrich) in a mixture of 0.5 mL of Tween20 and 1.5 mL of a buffer containing 20 mM HEPES, 25 mM KCl, and 5 mM $MgCl_2$ (pH 7.0) as described in ref 28. For imaging, I changed the culture medium of HeLa cells stably expressing ELP-TEMP to FluoroBrite DMEM (A1896701, ThermoFisher Scientific) supplemented with 10% FBS and GlutaMAX (35050-061, ThermoFisher Scientific). Subsequently, I dispersed 20 μL of the CNTs suspension into the culture medium. I used an inverted microscope (IX71, Olympus) equipped with a PlanApo 60X/1.40 oil-immersion objective lens (Olympus), a Light Engine (SPECTRA X, Lumencor), a stage-top incubator (INUB-ONICS, Tokai Hit), and a dual-view optics (W-View GEMINI, Hamamatsu photonics). I used a dichroic mirror of FF471/539-Di01 (Semrock) and an excitation filter of FF02-438/24 (Semrock). I used the dual-view optics equipped with a dichroic mirror (FF520-Di02, Semrock), emission filters of FF01-483/32 (Semrock) for mT and FF01-562/40 (Semrock) for mV, and a sCMOS camera (ORCA Flash4.0, Hamamatsu Photonics). The exposure time was 200 ms, and the binning of the sCMOS camera was 4x4 pixels. Before starting the experiment, I allowed CNTs to settle down for 30–60 min. To generate local heat, I irradiated a cluster of CNTs located near to several cells with a focused beam at 638 nm from a laser (Cube 635-20C, Coherent). For precisely synchronizing the laser, light engine, and sCMOS, I used a delay pulse generator (Sapphire Plus 9214+; Quantum Composers) coupled to them. The temperature was 34 °C, and the medium was in a 5% CO2 atmosphere.

Heat production with chemically induced Ca^{2+} influx. I transiently co-transfected HeLa cells stably expressing ELP-TEMP with R-GECO, a genetically encoded Ca^{2+} indicator[75] with the same transfection method mentioned above. I observed the cells with an inverted microscope (Ti-2, Nikon) equipped with a confocal unit (Dragonfly 200, Andor Technology), and the condition was the same in the cell imaging section mentioned above.

I stimulated the cells with ionomycin (I-700, Alomone Labs) to the final concentration of 4 μM in DMEM/F12 (11039-021, ThermoFisher Scientific) by a home-made perfusion system. Medium temperature was 34 °C. For data analysis, I selected ROIs in the nucleus or cytoplasm of cells and used a nucleus or cytoplasm calibration curve for estimating temperature.

2.3 Results and discussion

2.3.1 Development of ELP-based temperature indicators (ELP-TEMP)

I exploited the LCST behavior of ELPs to develop a FRET-based GETI. I designed my GETI so that it contained an ELP fused with a FRET pair of mT and mV. For the purpose of temperature imaging in mammalian cells, I selected ELP[V-60] containing a sequence of $(VPGVG)_{60}$, whose T_t was reported to be 35.2 °C[74]. Thereby, I constructed the gene of a fusion protein of mV-ELP[V-60]-mT denoted as ELP-TEMP0.5, an ELP-based temperature indicator (**Figure 2**).

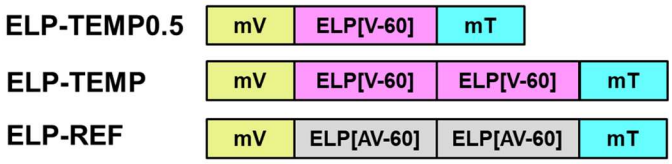

Figure 2. Gene design of ELP-TEMP0.5, ELP-TEMP, and ELP-Reference (ELP-REF).

The fluorescence emission spectrum of ELP-TEMP0.5 excited at 430 nm in a PBS solution showed fluorescence emission bands with peaks at 474 and 528 nm, which are attributed to mT and mV, respectively (**Figure 3A**). When I measured the fluorescence response of ELP-TEMP0.5 by scanning the temperature, the emission peak intensity of mT dramatically decreased as the temperature changed from 50 to 75 °C, whereas that of mV slightly increased (**Figure 3A**). **Figure 4** shows a plot of the fluorescence ratio of the fluorescence peak intensity of mV to that of mT (528/474 nm) against temperature. The data showed that as the temperature increased from 50 °C, the fluorescence ratio abruptly increased to a higher value, which was most likely ascribable to the phase transition behavior of the ELP (discuss below). Unfortunately, this temperature response was too high for mammalian cell imaging, and thereby, I decided to develop an ELP-based GETI with a lower temperature response.

Because an ELP with a large number of the pentapeptide repeats is known to show a low T_t[76], I then created a fusion protein consisting of a doubly repeated ELP[V-60], mT and mV, denoted as ELP-TEMP (**Figure 2**). ELP-TEMP also showed two fluorescence bands due to mT and mV like ELP-TEMP0.5 (**Figure 3B**), but the temperature response was found to shift to a considerably lower temperature around 40–55 °C (**Figure 4**).

Although this temperature response as measured in the PBS solution seemed somewhat higher than the optimum for temperature imaging in mammalian cells, the fluorescence ratio measured from a suspension of HeLa cells expressing ELP-TEMP was found to exhibit the transition of fluorescence ratio in the range of 30–45 °C (**Figure 5**), which was optimal for imaging of mammalian cells. Thus, ELP-TEMP is likely to be useful as a GETI for live mammalian cells.

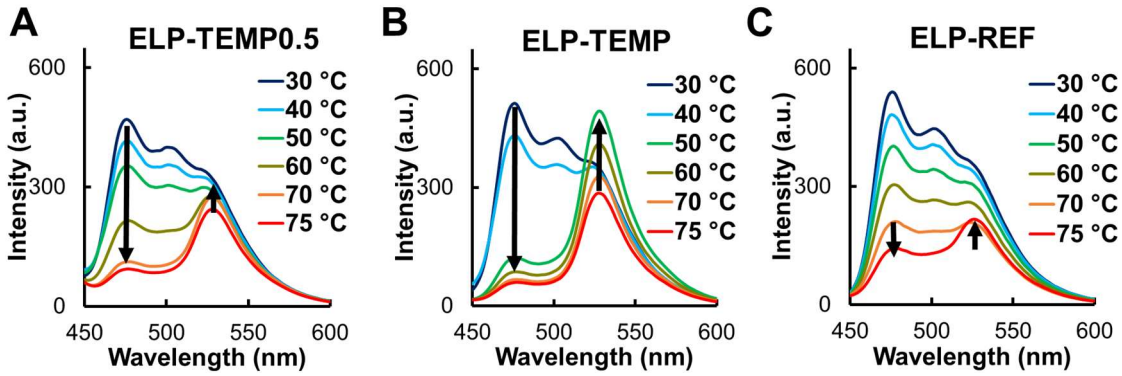

Figure 3. The fluorescence emission spectrum of (A) ELP-TEMP0.5, (B) ELP-TEMP, and (C) ELP-REF at various temperatures. Purified proteins (2 μM) were dissolved in a PBS solution (pH 7.4) and scanned the spectrum by a fluorescence spectrophotometer. The excitation wavelength was 430 nm.

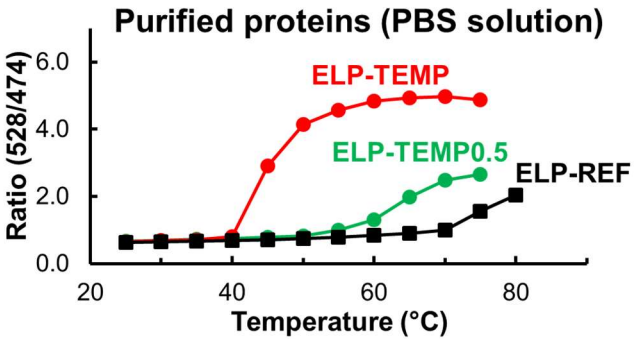

Figure 4. A plot of fluorescence ratio of mV (peak emission, 528nm) to mT (peak emission, 474 nm) of ELP-TEMP0.5, ELP-TEMP, and ELP-REF against temperature.

As a reference, I constructed another ELP-FP fusion protein, denoted as ELP-REF, composed of mT, mV, and an ELP with a doubly repeated sequence of ELP[AV-60] ($(VPGAG\text{-}VPGVG)_{30}$), which had the same polypeptide length with that of the ELP-TEMP (**Figure 2**). Because ELP[AV-60] itself was known to transition at 55.2 °C[74],

which was substantially higher than T_t of ELP[V-60][74], ELP-REF was expected to transition at a temperature higher than T_t of ELP-TEMP. In fact, T_t of ELP-REF was above 70 °C and the fluorescence ratio was almost unchanged between 25 and 60 °C (**Figure 3C, Figure 4**), regardless of the temperature dependence of the fluorescence intensities of mT and mV (**Figure 6**).

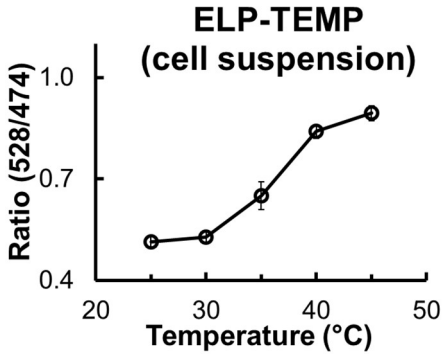

Figure 5. A plot of fluorescence ratio of ELP-TEMP in HeLa cell suspension against temperature. Approximate 5 million HeLa cells expressing ELP-TEMP were suspended in 0.5 mL PBS solution and measured the fluorescence by a fluorescence spectrophotometer. The excitation wavelength was 430 nm. Data are mean ± SD (n = 3).

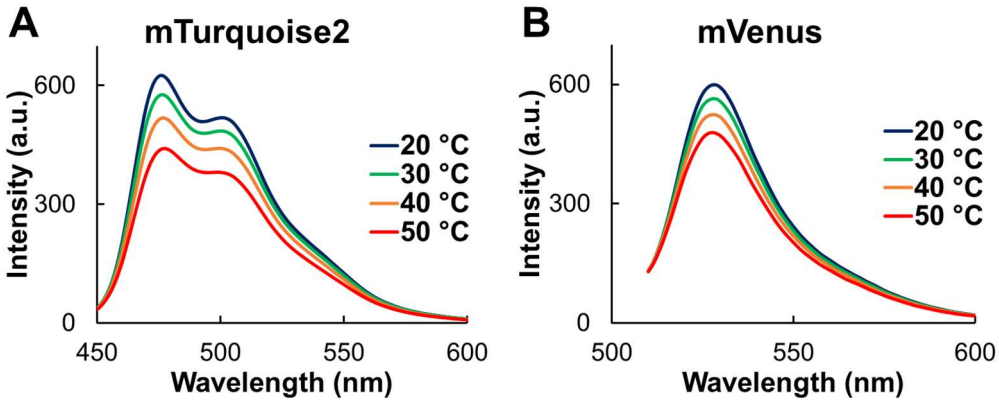

Figure 6. Temperature dependence fluorescence intensity of (A) mTurquoise2 (mT) and (B) mVenus (mV). Purified proteins were dissolved in a PBS solution (pH 7.4) and measured their fluorescence spectrum at various temperatures. Excitation was 430 and 500 nm for mT and mV, respectively.

Fluorescence ratio of ELP-TEMP changed in response to the temperature in relation with FRET. Previously, Tang *et al.* reported T_t of ELPs themselves as determined by solution turbidity by measuring the absorbance at 350 nm, and the order of T_t was ELP[AV-60] > ELP[V-60] > ELP[V-150][74]. The temperature response T_t of ELP-FP fusion proteins showed an order of ELP-REF (ELP[AV-60]-ELP[AV-60]) > ELP-TEMP0.5 (ELP[V-60]) > ELP-TEMP (ELP[V-60]-ELP[V-60]). In the standpoint of the guest residues in the pentapeptide, the order of ELP[AV-60] > ELP[V-60] should be consistent with that of ELP-REF > ELP-TEMP, which had the same polypeptide length. In the standpoint of the length of ELP moiety, the order of ELP[V-60] > ELP[V-150] should be consistent with that of ELP-TEMP0.5 > ELP-TEMP, which had the same guest residue. Thus, these results suggest that the transitions of fluorescence ratio seen in **Figure 4** should be largely attributed to the change of ELP moiety. Li *et al.* investigated temperature-dependent conformation of ELPs by molecular dynamics simulation and showed that at low temperature, the ELP molecules were in a much more extended conformation, whereas at temperatures above the T_t, ELP backbones underwent conformation changes, which were attributed to the formation of more ordered secondary structure of ELP[77]. Thus, it is suggested that below T_t, the conformation of ELP-FP fusion proteins, i.e., ELP-TEMP0.5, ELP-TEMP, or ELP-REF would be largely extended and dispersed[61] in the solution so that FRET from mT to mV occurs at a low efficiency. At temperatures above T_t, the ELP moiety in the ELP-FP fusion proteins may be ordered conformation and self-assembling into coacervate, so that the average distance between mT and mV becomes smaller than that below T_t, and FRET between them occurs at a high efficiency (**Figure 7**). In fact, at low temperatures, I observed a high mT fluorescence and a low mV fluorescence, indicating low FRET efficiency, whereas at elevated temperatures above the T_t, the mT fluorescence was abruptly decreased accompanied with an increase of mV fluorescence, indicating high FRET efficiency. This indicates that FRET efficiency is changed in accordance with the phase transient behavior of the ELPs, which is consistent with my hypothesis. Thus, ELP-TEMP would be the first FRET-based GETI, to my knowledge.

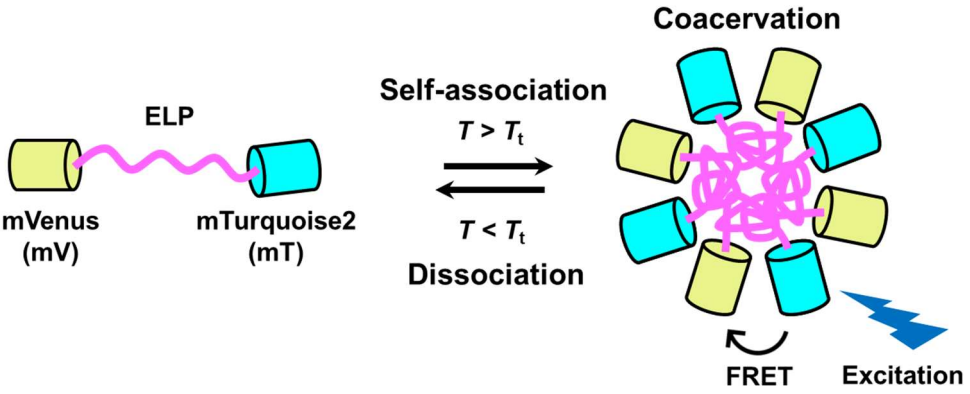

Figure 7. Schematic illustration of proposed temperature-sensing mechanism of ELP-FP fusion proteins exploiting lower critical solution temperature (LCST) of an ELP. ELP has coacervation property that is self-assembling of molecules with ordered structures dependent on increasing of temperature. At temperatures below T_t, the conformation of ELP-FP fusion proteins would be largely extended and dispersed in the solution so that FRET from mT to mV occurs at a low efficiency. At temperatures above T_t, the ELP moiety in the ELP-FP fusion proteins would undergo the conformation change and self-assembly into compacted coacervate so that the average distance between mT and mV becomes small, and FRET between them occurs at a high efficiency. In addition, because mT and mV are hydrophilic and ELP is hydrophobic, mT and mV may be largely exposed to the solvent and the ELP coacervate may be largely covered by mT and mV.

It should also be noted that the T_t of ELP-TEMP0.5 was significantly higher than that of the ELP[V-60] polypeptide itself [74]. This difference has been known as the "fusion ΔT_t effect" (fusion ΔT_t = T_t(ELP fusion protein) - T_t (free ELP)), which was caused by fusion with proteins that might change the conformation stability and the hydration surrounding the ELP[76,78]. Particularly, fusion with a hydrophobic protein resulted in a decrease of T_t, whereas fusion with a hydrophilic protein resulted in an increase of T_t of the ELP fusion protein compared to that of the ELP alone[76,78]. In my design, because ELPs are fused with two FPs, which have highly hydrophilic surface[78], the soluble state of the ELP-FP fusion proteins would be more favorable than that of the unfused ELPs, causing a shift to a higher transition temperature of the ELPs in the fusion proteins than that of the ELPs alone. Thus, the T_t of ELP-TEMP0.5, ELP-TEMP, and ELP-REF would have higher T_t than those of unfused ELPs, consistent with my results.

2.3.2 *In vitro* characterization of ELP-TEMP

I examined the effect of macromolecular crowding, self-concentration, and ion species on the temperature response of ELP-TEMP, as well as the reversibility of temperature response. To investigate the effect of macromolecular crowding, I utilized Ficoll PM70 as a macromolecular crowding reagent, because it is widely-used as a standard reagent that mimics the intracellular macromolecular crowding[71]. Although the ELP-TEMP fluorescence ratio also responded to elevated temperature in the presence of Ficoll PM70, the transition temperature shifted to lower temperatures as the Ficoll PM70 concentration increased (**Figure 8**), indicating that the temperature response of ELP-TEMP was affected by macromolecular crowding. At 14% w/w Ficoll PM70, the temperature response range of ELP-TEMP was about 30–45 °C, which was almost consistent with that in cell suspension (**Figure 5**), suggesting that the macromolecular crowding in HeLa cells would be equivalent to that in a PBS solution containing 14% w/w Ficoll PM70. The temperature response of ELP-TEMP was dependent to some degree on the self-concentration: the transition temperature shifted to lower temperatures as the ELP-TEMP concentration increased (**Figure 9**). The pH-dependence of ELP-TEMP fluorescence showed that the fluorescence ratio at 40 °C was almost unchanged between pH 6 and 8, but that at 45 and 50 °C declined below pH 6 (**Figure 10**). The temperature response of ELP-TEMP was little affected by the addition of KCl, NaCl, $MgCl_2$, or $CaCl_2$ (**Figure 11**). Additionally, the fluorescence ratio of ELP-TEMP responded to temperature change highly-reversibly during many cycles of heating and cooling (**Figure 12**).

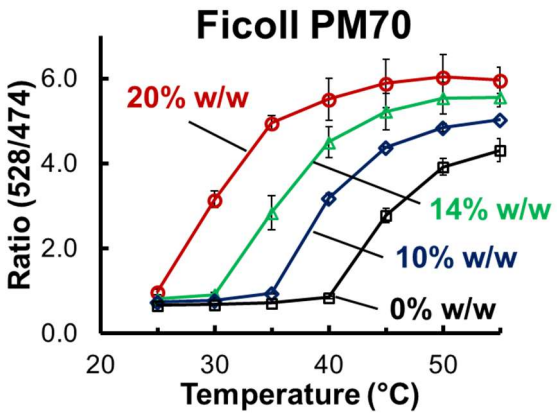

Figure 8. Effect of Ficoll PM70 as a macromolecular crowding reagent on the temperature dependence of fluorescence ratio of ELP-TEMP. Purified proteins (2

μM) were dissolved in the PBS solution containing Ficoll PM70 (0, 10, 14, and 20% w/w; pH 7.4). The excitation was 430 nm. Data are mean ± SD (n = 3).

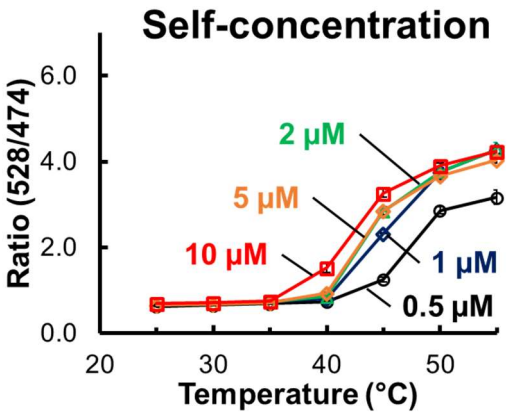

Figure 9. Effect of self-concentration of ELP-TEMP on its temperature dependence of fluorescence ratio. Purified proteins at different concentrations were dissolved in the PBS solution (pH 7.4). The excitation was 430 nm. Data are mean ± SD (n = 3).

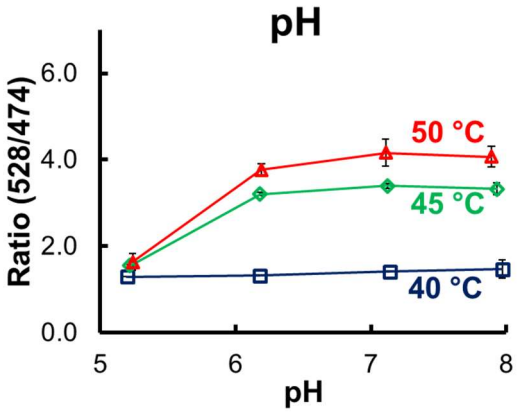

Figure 10. The pH-dependence of ELP-TEMP fluorescence ratio. The ELP-TEMP solution contained 30 mM trisodium citrate and 30 mM borax, whose pH was adjusted by adding HCl. The pH values of the solution were directly measured at various temperatures. The protein concentration was 2 μM. The excitation was 430 nm. Data are mean ± SD (n = 3).

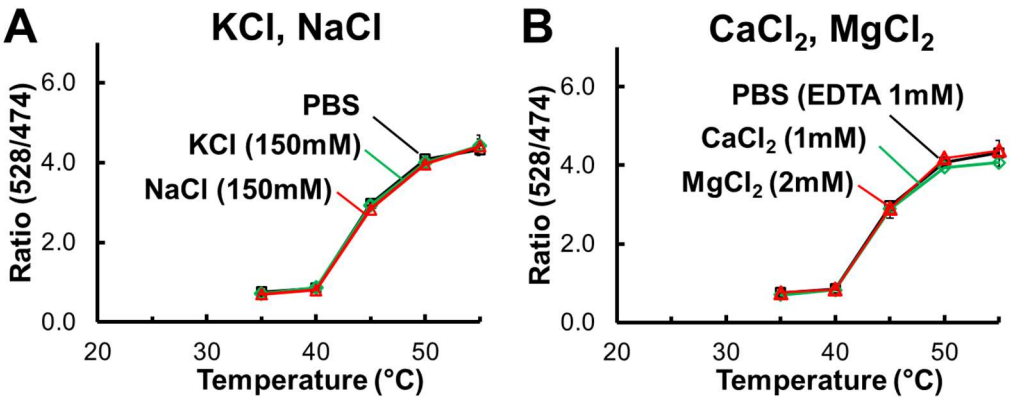

Figure 11. Effect of some salts on the temperature response of ELP-TEMP. (A) The effect of KCl or NaCl on the temperature response of ELP-TEMP. The ELP-TEMP solution contained PBS solution or 10 mM sodium phosphate buffer with 150 mM KCl or NaCl, pH 7.4. (B) The effect of $CaCl_2$ or $MgCl_2$ on the temperature response of ELP-TEMP. The ELP-TEMP solution contained the PBS solution and one of the salts. To mimic 0 mM of $CaCl_2$ or $MgCl_2$, I added EDTA to the final concentration of 1 mM to the PBS solution. The protein concentration was 2 μM. The excitation was 430 nm. Data are mean ± SD (n = 3).

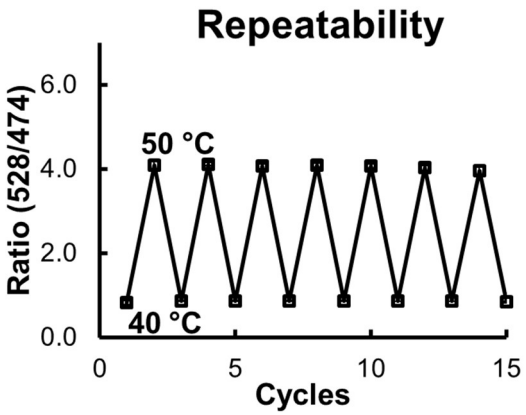

Figure 12.Effect of repeatability on the florescence ratio of ELP-TEMP. Purified proteins (2 μM) were dissolved in PBS solution (pH 7.4). The excitation was 430 nm. Data are mean ± SD (n = 3).

2.3.3 Temperature response of ELP-TEMP in live HeLa cells

I investigated the temperature response of ELP-TEMP in live HeLa cells. When I observed HeLa cells stably expressing ELP-TEMP by a confocal microscope, I were able to capture the fluorescence of mT and mV from the nucleus and cytoplasm in each cell, indicating that ELP-TEMP was present in both (**Figure 13A**). By analogy with the spectroscopy characterization of ELP-TEMP, I derived ratio images of the fluorescence of mV to that of mT (mV/mT) at various temperatures to examine the temperature response of ELP-TEMP in the cells, confirming that the fluorescence ratio changed with temperature between 34–40 °C (**Figure 13A**). By looking at the nucleus and cytoplasm, I noticed that the fluorescence ratios responded to temperature somewhat differently between them (**Figure 13A**). Thus, I separately analyzed the temperature-dependent fluorescence ratios in the nucleus and cytoplasm (**Figure 13B**). The data showed that the transition temperature in the nucleus would be lower by about 1 °C than that in the cytoplasm, and the fluorescence ratio in the nucleus was significantly higher than that in the cytoplasm. These differences would be mainly attributed to a difference in ELP-TEMP concentration (see **section 2.3.6**). Furthermore, I examined a relative temperature sensitivity S_T defined in **Equation 2** in the **Box 1** in **Chapter 1**. As shown in **Figure 14**, S_T of ELP-TEMP showed values of 5–45%/°C between 32 and 40 °C and maxima of 45.1 ± 8.1%/°C at 34 °C and 19.5 ± 5.0%/°C at 36 °C in the nucleus and cytoplasm, respectively. Compared from S_T values of previous GETIs and non-genetically-encoded indicators for intracellular thermometry (**Table 1**), the present S_T of ELP-TEMP was the highest ever reported temperature sensitivity. In addition, I evaluated a temperature resolution δT defined in **Equation 3** in the **Box 1** in **Chapter 1**. The δT value of ELP-TEMP was as fine as < 1 °C between 33 and 37 °C with the finest δT of 0.1 °C at 33 °C (**Figure 14**). In contrast, when I observed live HeLa cells stably expressing ELP-REF, I detected only a very small change in fluorescence ratios from 30 to 40 °C (S_T = 0–3.7 %/°C) (**Figure 15**).

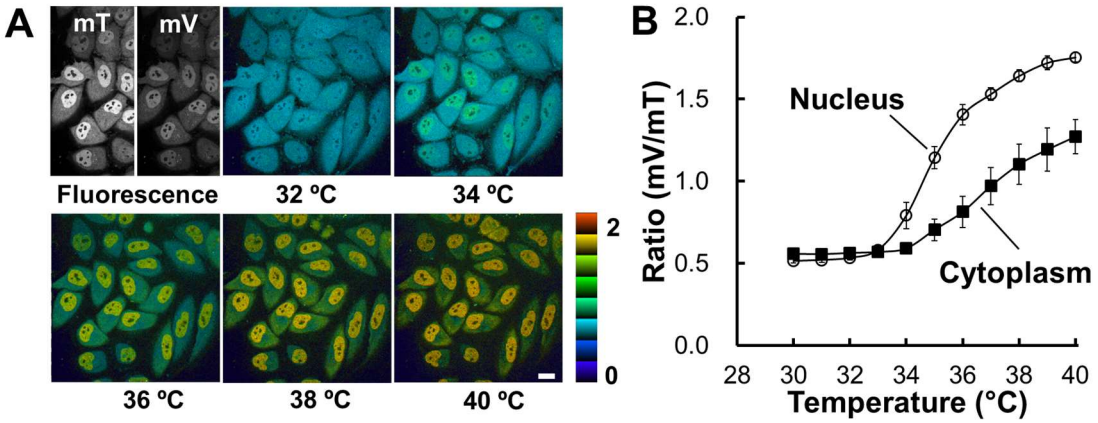

Figure 13. Temperature response of ELP-TEMP stably expressed in live HeLa cells. (A) Confocal fluorescence images and pseudo-colored ratio images of HeLa cells stably expressing ELP-TEMP at various temperatures. (B) A plot of fluorescence ratio mV/mT of ELP-TEMP in the nucleus and cytoplasm against medium temperature. The color bar indicates fluorescence ratio mV/mT. The scale bar, 20 μm. Data are mean ± SD (n = 18).

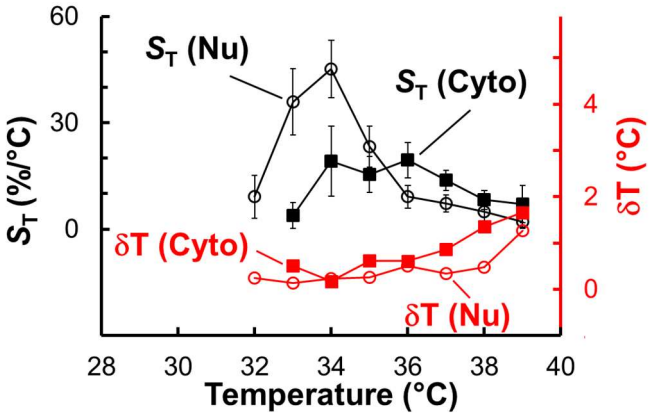

Figure 14. A plot of relative temperature sensitivity (S_T; left vertical axis) and temperature resolution (δT; right vertical axis) of the nucleus (Nu) or cytoplasm (Cyto) against medium temperature. S_T and δT are derived from **Figure 13**. Data are mean ± SD (n = 18).

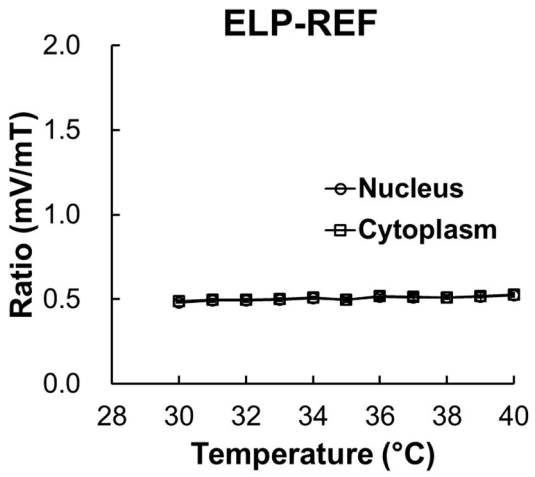

Figure 15. Temperature response of ELP-REF stably expressed in live HeLa cells. A plot of fluorescence ratio mV/mT of ELP-REF in the nucleus and cytoplasm against medium temperature. Fluorescence images were taken by the same imaging condition as in **Figure 13**. Data are mean ± SD (n = 16).

It should be noted that I used a HeLa cell line with stable ELP-TEMP expression. In fact, HeLa cells with transient ELP-TEMP expression showed a large variety of fluorescence ratios mV/mT (**Figure 16**), and thus, they were not suitable for temperature imaging in this study. Taking the data in **Figure 9** into consideration, the variety of fluorescence ratio suggests that, in cells transiently expressing ELP-TEMP, the expression level of ELP-TEMP would considerably differ from cell to cell (**Figure 17**). However, establishing a stable cell line could mitigate this effect as I showed that the stable cell line (**Figure 13B**) showed less variance in ratios than that of the transient cell line (**Figure 16B**). Thus, I used the HeLa cell line stably expressing ELP-TEMP throughout the study, unless mentioned.

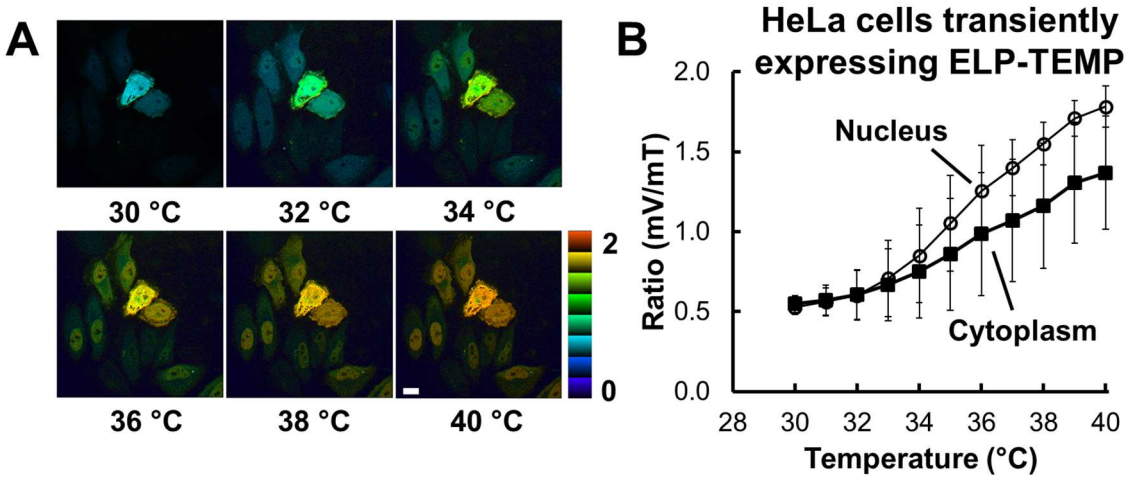

Figure 16. Confocal microscopy observation of live HeLa cells transiently expressing ELP-TEMP at various temperatures. (A) Pseudo-colored ratio images of HeLa cells transiently expressing ELP-TEMP at various temperatures. (B) A plot of fluorescence ratio mV/mT of ELP-TEMP in the nucleus and cytoplasm against medium temperature. Data are mean ± SD (n = 11). Fluorescence images were taken by the same imaging condition as in **Figure 13**. The color bar indicates fluorescence ratio of mV/mT. The scale bar, 20 μm.

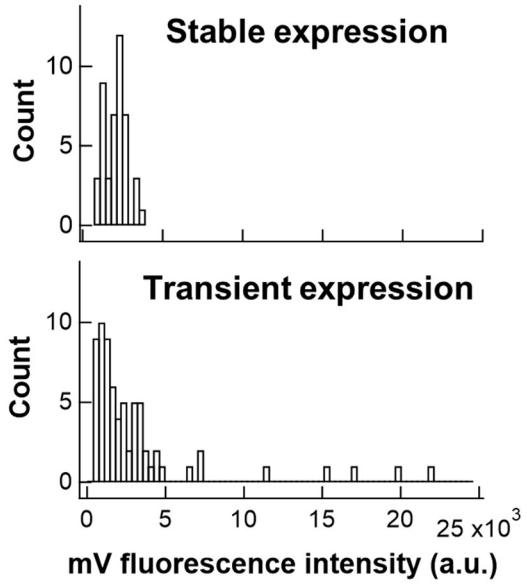

Figure 17. Histograms of mV fluorescence in ELP-TEMP by direct excitation mV at 514 nm between stable and transient expression of ELP-TEMP. The mV fluorescence intensity by direct excitation would represent the concentration of ELP-TEMP in cells**.**

I examined intracellular macromolecular crowding on the temperature response of ELP-TEMP, since fluorescence ratio of ELP-TEMP was affected by macromolecular crowding (**Figure 8**). I observed HeLa cell expressing a genetically encoded crowing indicator, crGE[71], at various temperatures with the same imaging conditions to those of the observation of ELP-TEMP. The fluorescence ratio of crGE was almost independent on temperature from 30 to 40 °C (**Figure 18**), indicating that the degree of macromolecular crowding in HeLa cells is likely to be almost unchanged during the microscopy observation. This result, as a control, suggests that the temperature response of ELP-TEMP (**Figure 13B**) was mostly attributed to temperature change.

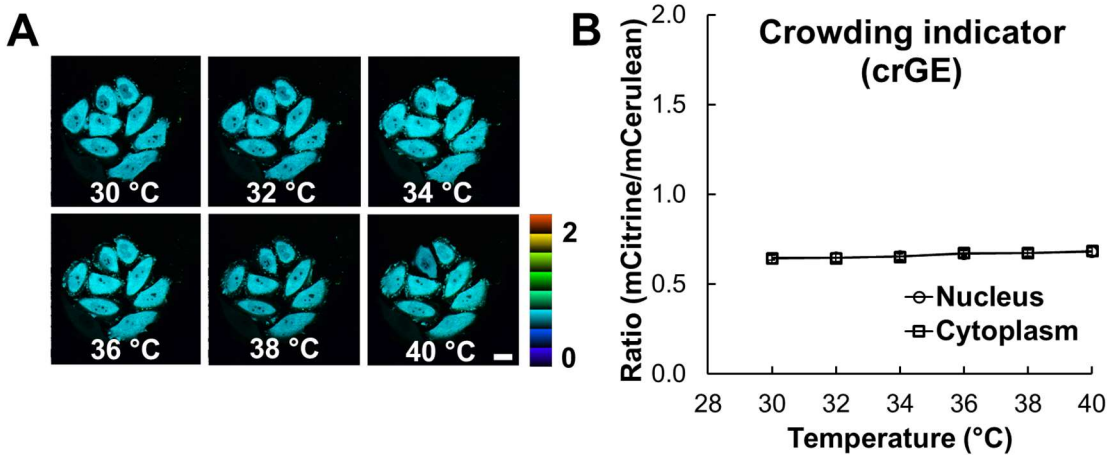

Figure 18. Confocal microscopy observation of live HeLa cells expressing a genetically encoded crowding indicator (crGE) at various medium temperatures. (A) Pseudo-colored ratio images of HeLa cells expressing crGE. Fluorescence images were taken by the same imaging condition as in **Figure 13**. (B) A plot of fluorescence ratio mCitrine/mCerulean in the nucleus and cytoplasm against medium temperature. The color bar indicates fluorescence ratio of mCitrine/mCerulean. The scale bar, 20 μm. Data are mean ± SD (n = 8).

2.3.4 Application of ELP-TEMP to monitor quick temperature rises with a local heat spot

I employed ELP-TEMP to demonstrate the imaging of quick temperature rises in live HeLa cells. I observed HeLa cells stably expressing ELP-TEMP mixed with a suspension of carbon nanotubes (CNTs) on an in-house built fluorescence microscope. I chose a CNT cluster near to two HeLa cells in the culture medium and irradiated it with a focused laser beam at 638 nm (**Figure 19A**). The laser beam irradiation brought about local heat production in the CNT cluster followed by heat diffusion from it[79]. In fact, when I turned on the beam irradiation of the CNT cluster, an increase of fluorescence ratio in the cells was observed, indicating a temperature increase (**Figure 19A**). When I turned off the beam irradiation, the fluorescence ratio decreased to the original level, indicating a temperature decrease, due to heat dissipation. Furthermore, I used the calibration of fluorescence ratio as a function of temperature taken separately from the nucleus and cytoplasm (**Figure 20**) to determine the temperature increment ΔT in regions of interests (ROIs) 1–4 relative to the surrounding medium temperature (**Figure 19A**). A plot of ΔT against time (**Figure 19B**) shows that the read-out of temperatures from ELP-TEMP reversibly responded to the laser irradiation of the CNT cluster. Additionally, the dependence of the plateau ΔT in ROI 1 during heating on the laser power (**Figure 19C**) confirmed that the increase of ΔT was well correlated with the energy flux directing the CNT cluster. Thus, these data demonstrate that I successfully applied ELP-TEMP to detect reversible temperature changes due to the heat production and dissipation arising from turning on and off the heat production in the CNT cluster.

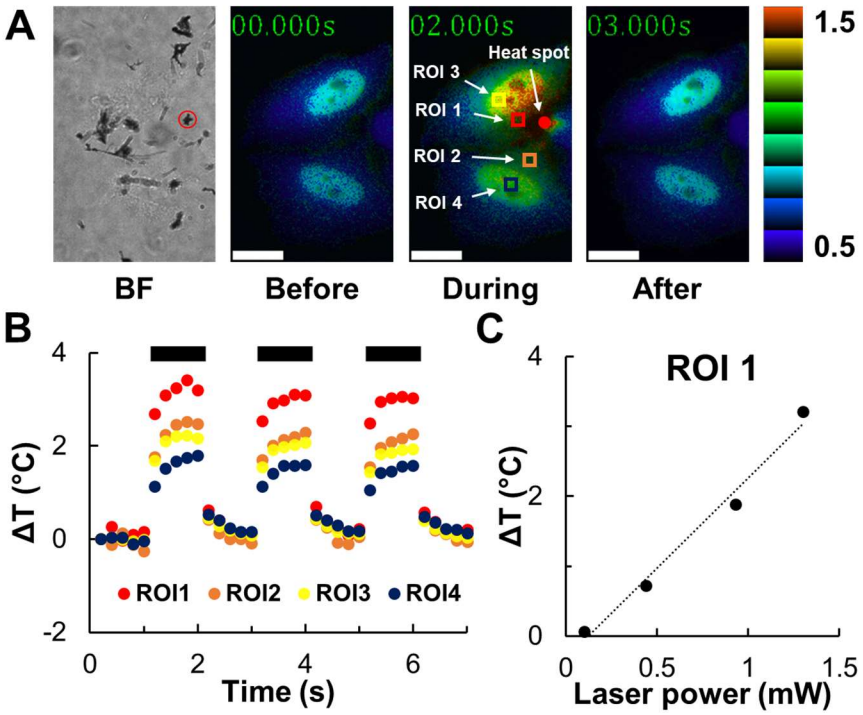

Figure 19. Application of ELP-TEMP to monitor quick temperature rise in live HeLa cells with a local heat. (A) Bright-field (BF) and pseudo-colored ratio images of HeLa cells stably expressing ELP-TEMP before, during, and after local heating. The red circle indicates the CNT cluster, i.e., the heat spot, whereas squares indicate regions of interest (ROI). (B) A plot of temperature increment ΔT as the function of time in ROIs 1–4. The temperature of ROI 1 and 2 was estimated from the cytoplasm calibration curve, whereas the temperature of ROI 3 and 4 was estimated from the nucleus calibration curve in **Figure 20**, respectively. A CNT cluster located near two cells was irradiated with a 638 nm laser beam at a power of 1.3 mW. Black lines indicate the periods of laser irradiation. (C) A plot of ΔT in ROI 1 as a function of the laser power at 638 nm. The medium temperature was 34 °C. The color bar indicates fluorescence ratio mV/mT. The scale bar, 20 μm.

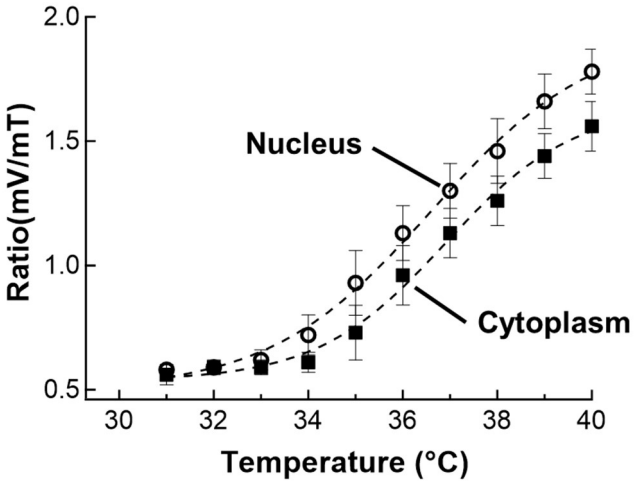

Figure 20. A plot of mV/mT ratio of ELP-TEMP in the nucleus and cytoplasm against temperature observed by the same microscope for the CNTs experiments. Fluorescence images were taken by the same imaging condition as in **Figure 19** (see Material and methods for detail). Dash lines indicate sigmoidal fitting. Data are mean ± SD (n = 6).

I also examined a cross-section of ΔT during heating across the nucleus and cytoplasm in a HeLa cell. I took a profile of the plateau temperature increment ΔT during heating along a line which crossed the CNT cluster, i.e., the heat spot, the nucleus, and the cytoplasm (**Figure 21A**). It should be noted that because the calibrations of the fluorescence ratios as a function of temperature were significantly different between the nucleus and cytoplasm (**Figure 20**), I calculated ΔT values in them separately using the corresponding calibrations. A plot of ΔT as a function of the distance from the heat spot shows that the values of ΔT depended on both the distance from the heat spot and the total laser power at 638 nm. Importantly, the ΔT values seemed to continuously decrease with the distance irrespective of whether a ROI was in the nucleus or cytoplasm, and thus, a discontinuity in ΔT seemed not to be noticeable at the interface between them (**Figure 21B**). This result confirmed the continuity of temperature in the cell, suggesting that the temperature inside the cell was well estimated by the present protocol using the organelle-specific calibration curves (**Figure 20**). Additionally, because of the high S_T, ELP-TEMP was able to map a temperature difference in single cells even if ΔT was as small as <1 °C (**Figure 21A**). These results altogether demonstrate that ELP-TEMP would be a very

useful GETI to visualize intracellular temperature dynamics that have been previously invisible on the micrometer to nanometer scale.

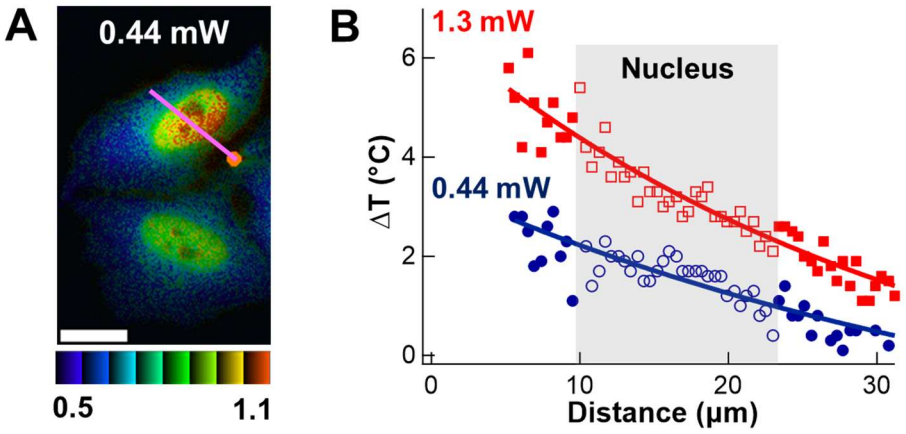

Figure 21. Temperature profile across a line. (A) A pseudo-colored ratio image of HeLa cells stably expressing ELP-TEMP under local heating with the laser power of 0.44 mW. A line indicates ROI. (B) A plot of ΔT of the line in panel (A) against the distance from the heat spot. Closed and opened blue circles represent ΔT in the cytoplasm and nucleus with the laser power of 0.44 mW, whereas closed and opened red squares represent ΔT in the cytoplasm and nucleus with the laser power of 1.3 mW, respectively. The transparent box indicates the nucleus area. The medium temperature was 34 °C. The color bar indicates fluorescence ratio mV/mT. The scale bar, 20 μm.

2.3.5 Visualization of heat production from Ca^{2+} influx induced by ionomycin stimulation

I tried to detect heat production caused by ionomycin-induced Ca^{2+} influx, which has been reported to give rise to an intracellular temperature increase by 1–2 °C[33,36,42]. I stimulated HeLa cells stably expressing ELP-TEMP with 4 μM ionomycin by perfusion, and observed the cells with the same confocal microscope as that in **Figure 13** so that I could determine the intracellular temperature from the calibration in **Figure 13B**. I transiently co-transfected the HeLa cells stably expressing ELP-TEMP with a genetically encoded Ca^{2+} indicator, R-GECO[75], to monitor Ca^{2+} concentration change. As shown in **Figure 22A,B**, I detected an abrupt increase of Ca^{2+} concentration at t = 210 s in the cells through R-GECO fluorescence, being most likely due to Ca^{2+} influx stimulated by ionomycin. Furthermore, I found that the Ca^{2+} concentration increase was followed by a significant increase of the fluorescence ratio mV/mT of ELP-TEMP in both nucleus and cytoplasm (two-tailed Student's t-test led to p = 0.0007 and 0.007 for nucleus and cytoplasm, respectively, between t = 0 and t = 600 s in **Figure 22D,E**. As a control, I also took the fluorescence image of mV directly-excited at 514 nm during the observation of **Figure 22** as a measure of ELP-TEMP average concentration in the ROIs (see **Section 2.3.6**). The fluorescence intensity of directly-excited mV was observed to be almost unchanged with the Ca^{2+} concentration was increase induced by ionomycin stimulation, and thus, the ELP-TEMP concentration would have been almost unchanged during this observation (**Figure 23**). As another control, I examined macromolecular crowding in HeLa cells transfected with both macromolecular crowding indicator crGE[71] and R-GECO before and after ionomycin stimulation. However, the fluorescence ratio mCitrine/mCerulean of crGE, i.e., macromolecular crowding was unchanged even though Ca^{2+} concentration increased as observed by R-GECO fluorescence increase (**Figure 24**). In addition, I should also note that the fluorescence ratio of ELP-TEMP was little affected by the addition of $CaCl_2$ (**Figure 11B**). Accordingly, considering the results thus far, the fluorescence ratio increase from ELP-TEMP after ionomycin stimulation (**Figure 22D,E**) is likely to be attributed to temperature increase caused by Ca^{2+} influx. Using the nucleus and cytoplasm calibration curves in **Figure 13B**, I was able to estimate the average temperature increase (ΔT) before (average temperature in a range of t = 0–180 s) and after ionomycin stimulation (average temperature in a range of t = 420–600 s) in the nucleus

and cytoplasm, respectively, to be ΔT = 1.0 ± 0.8 °C and 1.5 ± 0.7 °C (means ± SD, n = 7), which was consistent with previously reported studies[33,36,42]. The difference in ΔT between the nucleus and cytoplasm should be ascribed to the heat source of thermogenesis, which was considered due to SERCA pumping up Ca^{2+} into endoplasmic reticulum (ER)[36,80], and this difference may have not been reported previously to my knowledge.

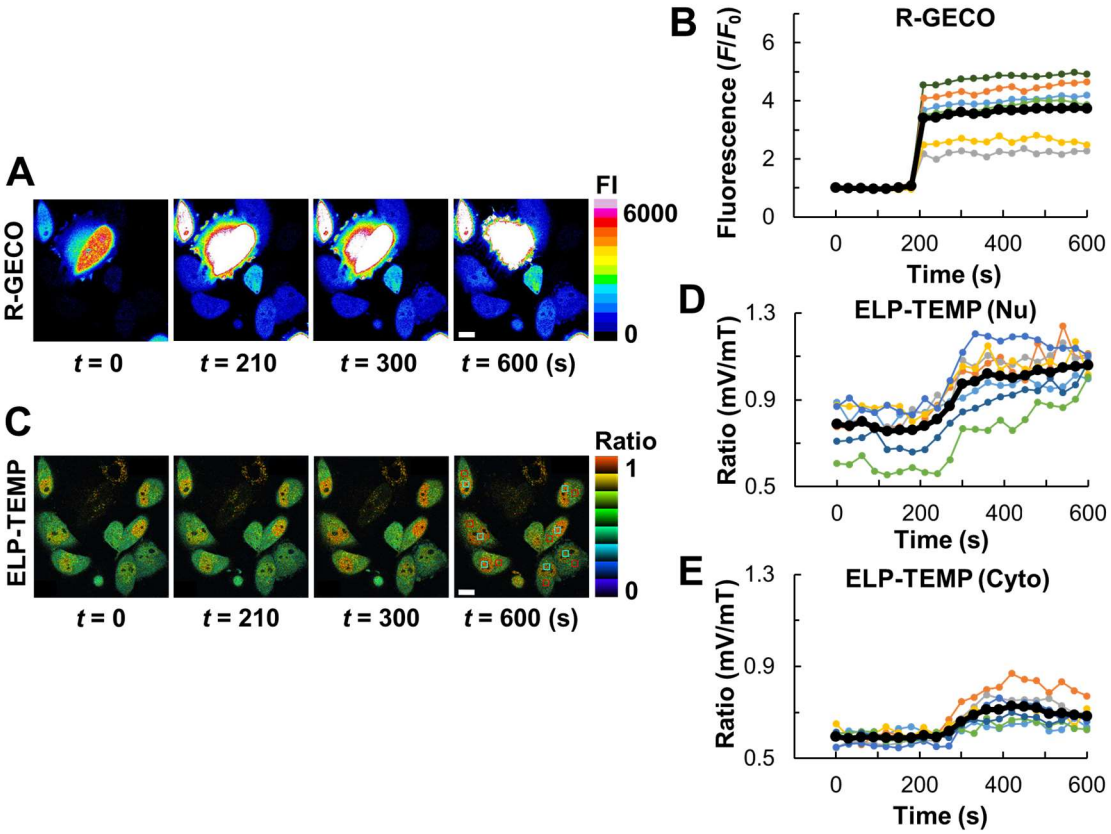

Figure 22. Visualization of heat production from Ca^{2+} influx induced by Ca^{2+}-ionophore ionomycin in live HeLa cells stably expressing ELP-TEMP and transiently co-expressing R-GECO. (A) Pseudo-colored fluorescence images of R-GECO in responding to ionomycin stimulation. (B) A plot of fluorescence intensity (F/F_0) of R-GECO against time. (C) Pseudo-colored ratio images of ELP-TEMP in responding to ionomycin stimulation. (D) A plot of fluorescence ratio mV/mT of ELP-TEMP in the nucleus (Nu) against time. (E) A plot of fluorescence ratio mV/mT of ELP-TEMP in the cytoplasm (Cyto) against time. The observation was performed under the same confocal microscope in **Figure 13B**. To prevent changes in medium temperature due to ionomycin stimulation, medium containing 4 μM ionomycin was supplied through a preheated perfusion tube, and the medium temperature around the observed cells was

maintained at 34 ± 0.1°C during observation. Red and cyan squares indicate ROIs for cytoplasm and nucleus, respectively. The color bars indicate fluorescence intensity (FI) and ratio for (A) and (C), respectively. Scale bars, 20 μm.

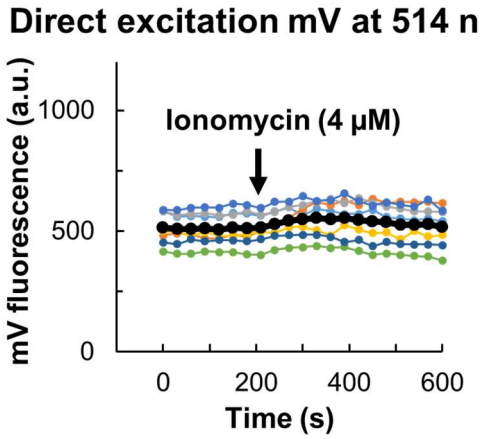

Figure 23. Investigation of the effect of ELP-TEMP concentration by direct excitation mV in ELP-TEMP under the stimulation of ionomycin. The mV fluorescence images were captured in the same experiment in **Figure 22C,D,E**. The mV fluorescence intensity was taken from the same ROIs as in **Figure 22C,D,E**. I used a 514 nm laser for direct excitation mV and collected the fluorescence emission through a bandpass filter (ET540/30nm; Chroma). I took the fluorescence images by an EMCCD camera (iXon Ultra, Andor Technology). Exposure time, 150 ms; binning size, 2×2 pixels. The arrow indicates the start of Ca^{2+} influx induced by ionomycin stimulation.

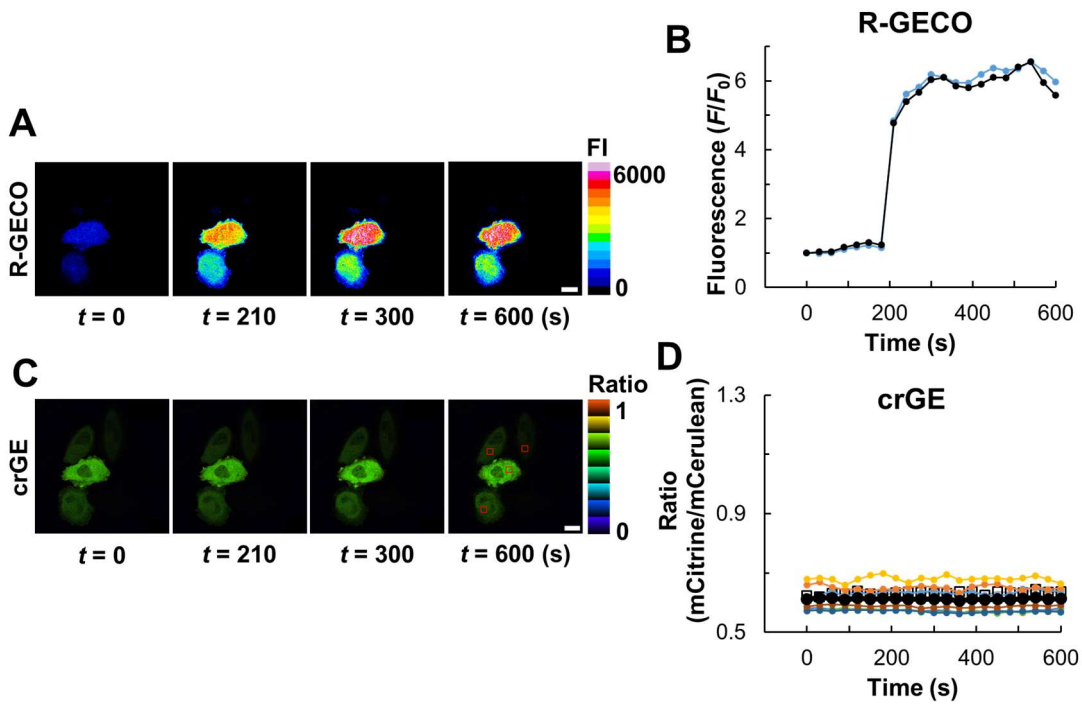

Figure 24. Investigation of the effect of ionomycin treatment on macromolecular crowding of HeLa cells transiently co-expressing crGE and R-GECO. (A) Pseudo-colored fluorescence images of R-GECO in responding to ionomycin stimulation. (B) A plot of fluorescence intensity (F/F_0) of R-GECO against time. (C) Pseudo-colored ratio images of crGE in responding to ionomycin stimulation. (D) A plot of fluorescence ratio of crGE against time. The observation was performed under the same confocal microscope in **Figure 13B**. Ionomycin (4 μM) was added into the cell media by perfusion. Red squares indicate ROIs. The color bars indicate fluorescence intensity (FI) and ratio for (A) and (C), respectively. Medium temperature was 34 °C. Scale bars, 20 μm.

2.3.6 Investigation of the difference in temperature response of ELP-TEMP between the nucleus and cytoplasm

I investigated the difference in temperature response of ELP-TEMP between the nucleus and cytoplasm as observed in **Figure 13A,B**. Since I clearly observed a difference of ELP-TEMP fluorescence intensities between the nucleus and cytoplasm (**Figure 13A**), I speculated that the ELP-TEMP concentration may have been different between them. Thus, I tried to measure ELP-TEMP concentrations in the nucleus and cytoplasm to figure out the temperature response of ELP-TEMP in them. To measure the ELP-TEMP concentration in cells, I measured the mV fluorescence in ELP-TEMP by direct excitation mV at 514 nm with a confocal microscope. Because mV is the acceptor of FRET in ELP-TEMP, its fluorescence intensity by direct excitation should not be susceptible to the change of FRET efficiency, and therefore, it was expected to be little dependent on the conformation of the ELP moiety. As shown in **Figure 25**, the mV fluorescence intensity in the nucleus was measured to be 3.3-fold higher than that in the cytoplasm, and thereby, ELP-TEMP concentrations in the nucleus and cytoplasm were estimated as 1.3 ± 0.6 μM and 0.4 ± 0.2 μM, respectively, by using a calibration of the mV fluorescence intensity by direct excitation from purified ELP-TEMP (**Figure 26**).

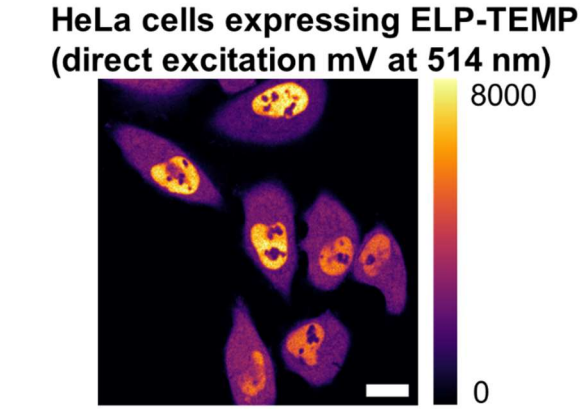

Figure 25. Estimation of ELP-TEMP concentration in HeLa cells. Fluorescence image of mV signal in ELP-TEMP by direct excitation at 514 nm observed by a confocal microscope. The mV fluorescence intensity in the nucleus was measured to be 3.3-fold higher than that in the cytoplasm. From this calibration curve in **Figure 26**, the ELP-TEMP concentration in the nucleus and cytoplasm was estimated to be 1.3 ± 0.6 μM and

0.4 ± 0.2 μM (n = 43 cells), respectively. The color bar indicates fluorescence intensity of mV. The scale bar, 20 μm.

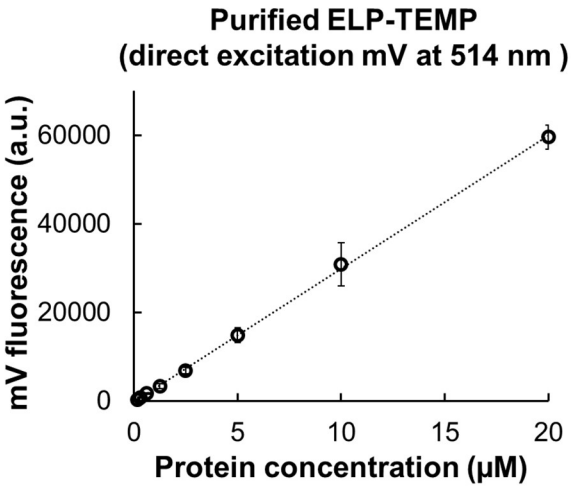

Figure 26. A plot of mV fluorescence intensity directly-excited at 514 nm in purified ELP-TEMP against the protein concentration observed by a confocal microscope. Purified ELP-TEMP was dissolved in a DMEM/F12 medium that used for cell imaging. The imaging condition was the same as that in **Figure 25**. In particular, I used a 514 nm laser for direct excitation mV and collected the fluorescence emission through a bandpass filter (ET540/30nm; Chroma). I captured the fluorescence images with an EMCCD camera (iXon Ultra, Andor Technology). The exposure time was 150 ms, and the binning size was 2×2 pixels. Data are mean ± SD (n = 3).

In addition, since a result from Western Blotting showed that ELP-TEMP was little degraded in HeLa cells (**Figure 27**), the mV fluorescence intensity from the cells in **Figure 25** was mostly ascribed to the ELP-TEMP. With the information of ELP-TEMP concentrations, I then measured the temperature response of purified ELP-TEMP in a PBS solution at concentrations of 1.3 and 0.4 μM corresponding to the ELP-TEMP concentration in the nucleus and cytoplasm, respectively, and compared their temperature responses with those measured in cells. To mimic the intracellular macromolecular crowding, I added Ficoll PM70 to the PBS solution, in which I optimized the concentration to 14% w/w Ficoll PM70 that well emulated the temperature response of 1.3 μM ELP-TEMP to that of the nucleus (**Figure 28**). As shown in **Figure 29**, the temperature response of ELP-TEMP at concentrations of 1.3 and 0.4 μM in the presence

of 14% w/w Ficoll PM70 was highly consistent with the temperature response of ELP-TEMP in the nucleus and cytoplasm, respectively. Furthermore, I also examined the macromolecular crowding in the nucleus and cytoplasm on the temperature response of ELP-TEMP. When I observed HeLa cells expressing crGE, I found that the fluorescence ratios from the nucleus and cytoplasm were almost the same between 30 and 40 °C (**Figure 18**), indicating that the macromolecular crowding was almost equivalent in them. This result suggests that macromolecular crowding would have a very little effect on the observed difference of ELP-TEMP between the nucleus and cytoplasm. Thus, considering the results presented here, the difference in the temperature response of ELP-TEMP between the nucleus and cytoplasm would be mainly attributed to the ELP-TEMP concentration difference in them.

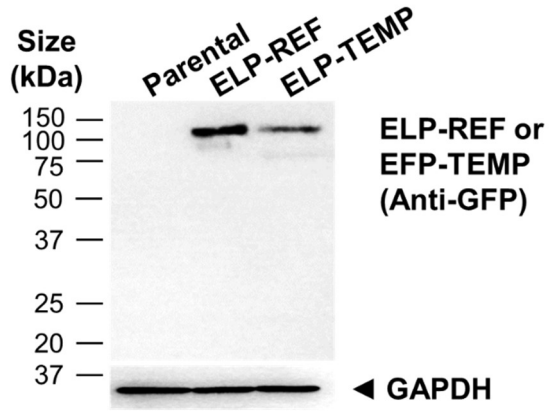

Figure 27. Western Blotting of stable HeLa cell lines expressing ELP-REF or ELP-TEMP. The parental indicates HeLa cells without transfection. The indicators were detected by anti-GFP, whereas anti-GAPDH was used as a loading control (see Material and methods for detail).

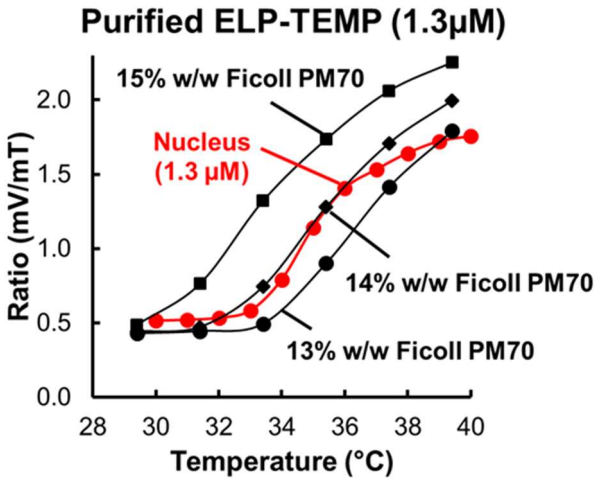

Figure 28. Optimization of the effect of Ficoll PM70 on the temperature response of ELP-TEMP. Purified ELP-TEMP (1.3 μM) was dissolved in a PBS solution containing 13, 14, or 15% w/w Ficoll PM70. For comparison with the microscopy data, I calculated the integral of $F(\lambda)T(\lambda)$ for mT and mV, where F is a fluorescence emission spectrum and T is a composite spectral transmittance of a bandpass filter and a dichroic mirror. The integration wavelengths were 457–500 nm and 526–552 nm for mT and mV, respectively. Additionally, I directly measured the temperature of the ELP-TEMP solution with the same thermometer used for the microscopy observation. The temperature response of ELP-TEMP in the nucleus (red line) was obtained from microscopy data in **Figure 13B**. The excitation was 430 nm.

I look at the difference of fluorescence ratios of ELP-TEMP in the nucleus and cytoplasm. Although there have been several reports suggesting a temperature difference between the nucleus and cytoplasm in mammalian cells[15,19,22,81], it still remains controversial[56-58,82]. According to the results of in vitro characterization, the temperature response of ELP-TEMP was dependent on the self-concentration, macromolecular crowding and the environment pH, and thus, I questioned whether these factors were responsible for the observed difference between the nucleus and cytoplasm. I showed that purified ELP-TEMP at concentrations of 1.3 and 0.4 μM in a PBS solution containing 14% w/w Ficoll PM70 was able to well emulate the temperature response of ELP-TEMP in the nucleus and cytoplasm. In addition, by using crGE, I ruled out the possibility of the effect of macromolecular crowding on the observed difference. From a previous study, the pH in HeLa cells was measured to be 7.4 ± 0.2 without significant difference between

the nucleus and cytoplasm[83]. Thus, the difference of the temperature response in the nucleus and cytoplasm should be mainly attributed to the difference of ELP-TEMP concentration in them. Furthermore, from the result in **Figure 29**, although I assumed that the temperatures in the nucleus and cytoplasm in HeLa cells were the same as that in the culture medium, the fluorescence ratio of purified ELP-TEMP in a temperature control of the fluorescence spectrophotometer was in good agreement with the microscopy data in the nucleus and cytoplasm. The result in **Figure 21B** suggested that there seemed no noticeable thermal boundary at the interface between the nucleus and cytoplasm. As shown in **Figure 13A**, the fluorescence ratio of ELP-TEMP was observed to be almost uniform in the nucleus or cytoplasm. Thus, considering the evidence presented here, the temperatures in the nucleus and cytoplasm in the absence of heat source should be almost the same within the temperature resolution of the measurement.

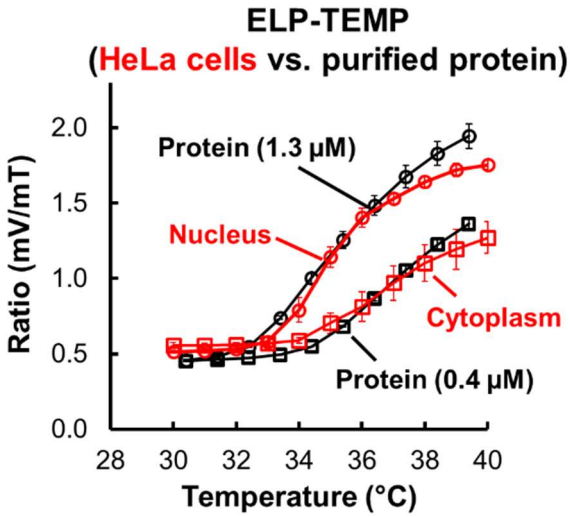

Figure 29. Comparison of temperature response of ELP-TEMP in HeLa cells by confocal microscopy *versus* purified ELP-TEMP. Data of HeLa cells (red lines) was taken from **Figure 13B**. Purified ELP-TEMP with concentrations of 1.3 and 0.4 μM was dissolved in a PBS solution containing 14% w/w Ficoll PM70 and measured fluorescence spectrum by a fluorescence spectrophotometer. For comparison with the microscopy data, I calculated the integral of $F(\lambda)T(\lambda)$ for mT and mV, where F is a fluorescence emission spectrum and T is a composite spectral transmittance of a bandpass filter and a dichroic mirror. The integration wavelengths were 457–500 nm and 526–552 nm for mT and mV, respectively. Additionally, I directly measured the temperature of the ELP-TEMP

solution with the same thermometer used for the microscopy observation. The excitation was 430 nm. Data are mean ± SD (n = 3).

In the present study, I examined temperature in HeLa cells in the steady state and the drug-stimulated state. In the heating experiment using a CNT cluster and the irradiation of focused laser beam, the temperature in HeLa cells in the steady state changed passively: the temperature changed back and forth rapidly at a time constant of ~200 ms with turning on and off the laser beam irradiation (**Figure 19B**) and no thermal boundary or gap was noticeable in the distance-temperature profile taken from the cell during heating (**Figure 21B**). In addition, the temperatures in the nucleus and cytoplasm of HeLa cells in the steady state without any external heat source and drug stimulation were measured to be indistinguishable (**Figure 29**). Baffou *et al.*[56] estimated by using the heat diffusion equation that the temperature inside a cell could be higher than its surrounding environment by ~10^{-5} K, in which they assumed heat conduction in watery environment and a steady-state heat production of ~100 pW/cell[56]. The conditions of the cells in **Figure 19**, **Figure 21** and **Figure 29** might be apparently somewhat near to the situation discussed by Baffou *et al.*, considering that the amount of heat production of HeLa cells was measured to be ~10^{1} pW/cell[84] together with the approximation by Baffou *et al.*[56] such that $\Delta T = P/\kappa L$, where ΔT is an expected temperature increase (K), P is the amount of heat production (W), κ is a thermal conductivity ($Wm^{-1}K^{-1}$), and L is a typical size of a heat source[56]. In contrast, when HeLa cells were stimulated by the addition of ionomycin, the temperature increase (ΔT = ~1.5 K in the cytoplasm) was observed to last for >100 s (**Figure 22E**). Because ionomycin allows for stimulated transport of Ca^{2+} across a membrane[85], the influx of Ca^{2+} toward the inside of cells induced by ionomycin occurs as observed by the R-GECO fluorescence (**Figure 22B**) and this should lead to the activation of intracellular Ca^{2+} pumps that hydrolyze ATP[80], possibly having a knock-on effect on the activation of the intricate metabolism. In fact, in the observation of HeLa cells stimulated with ionomycin, the fluorescence response of ELP-TEMP was observed to delay by ~120 s after the increase of Ca^{2+} concentration, and this delay has been reported previously[36,42]. Thus, the observation of the continued temperature increase observed in the ionomycin stimulation (**Figure 22D,E**) may be compatible with a presumption by Suzuki *et al.*[57] that an intracellular temperature

increase relative to the environment under stimulation could be sustained by continued glucose uptake.

I have demonstrated that, by properly calibrating ELP-TEMP, I was able to measure temperature inside cells for high accuracy at an optical microscopy resolution. Moreover, by localizing ELP-TEMP to a specific organelle by fusing with a targeting peptide or protein, I would be able to measure the temperature in an organelle of interest. Although the fusion of ELP-TEMP with a targeting peptide or protein may change the transition temperature of ELP-TEMP due to the "fusion ΔT_t effect" of the ELP, it would be possible to be compensated by a proper calibration. Because of the remarkable S_T, I expect that, in the future, ELP-TEMP would be able to reveal small heat production arising from biological processes or drug stimulations that have been previously invisible at the cellular/subcellular level.

2.4 Summary

Here, I successfully developed the first-FRET based GETI, denoted as ELP-TEMP, exploiting the LCST behavior of an ELP fused with a FRET pair of FPs. I demonstrated the temperature-sensing performance of ELP-TEMP for intracellular temperature measurement in mammalian cells with high accuracy. Because ELP-TEMP achieved the highest ever S_T among reported fluorescent nanothermometers, ELP-TEMP would solve the main drawback of poor S_T of GETIs. In addition, because the temperature imaging with ELP-TEMP provided a quantitative measurement and ELP-TEMP was expressed in live cells by simply transfecting the cells with a common transfection method, ELP-TEMP has overcome the limitation of other approaches using ELPs for temperature measurement such as ELPs fused with a GFP that only detect a temperature at the T_t of ELPs[63] and ELP chemically labeling with a hydrophobicity-sensitive fluorescent dye[64]. Despite the advantages, I found that ELP-TEMP showed sensitivity not only to temperature but also to macromolecular crowding and self-concentration. However, by the observation with a genetically encoded crowding indicator, crGE[71], the possibility of the effect of the macromolecular crowding on the temperature response of ELP-TEMP was rule out as far as the imaging conditions in my study applied. Additionally, by using the stable cell line, I mitigated the effect of different expression level of ELP-TEMP, i.e., ELP-TEMP concentration, from cell to cell, and by measuring the concentrations of ELP-TEMP in the nucleus and cytoplasm separately, I were able to determine the accurate temperature response of ELP-TEMP in them, which depended on ELP-TEMP concentration. Using ELP-TEMP, I demonstrated its temperature-sensing performance to accurately measure temperature changes in live HeLa cells at subcellular level, even if the temperature difference was as small as <1 °C, and to visualize the heat production from Ca^{2+} influx for >100 s induced by the stimulation of Ca^{2+}-ionophore ionomycin. Additionally, I investigated the temperature in the nucleus and cytoplasm, and found that their temperature was almost the same within the temperature resolution of the measurement. Thus, ELP-TEMP will be a very useful GETI for the investigation of cell thermobiology.

CHAPTER 3
CHARACTERIZATION OF A BLUE-EXCITED GENETICALLY ENCODED TEMPERATURE INDICATOR

3.1 Introduction

Previously, Nagai laboratory developed a genetically encoded ratiometric fluorescent temperature indicator (gTEMP) for temperature imaging in live cells and organisms[15]. gTEMP is composed of a green FP, mT-Sapphire (mT-Sap) with low temperature sensitivity and blue FP, Sirius with high temperature sensitivity. Because of their difference in temperature sensitivity, fluorescence ratios of mT-Sap to Sirius can be used as a measure for temperature. In addition, both mT-Sap and Sirius can be excited by the same wavelength of light (~370 nm), and thus their fluorescence was simultaneously observed, allowing ratiometric temperature imaging at a high temporal resolution. Moreover, temperature-sensing performance of gTEMP was little affected by other factors such as K^+, Ca^{2+}, Mg^{2+}, and pH as long as the solution was near to the physiological conditions. gTEMP showed a relative temperature sensitivity of 2.6 %/°C within a wide detection range of temperature from 5 to 50 °C. In HeLa cells, gTEMP showed a rapid response to a local temperature rise induced by irradiating with an infrared laser with a time resolution of 50 ms. Additionally, by localizing gTEMP to mitochondria, gTEMP was able to measure heat production inside mitochondria by treatment of an uncoupling reagent, carbonyl cyanide 4-(trifluoromethoxy)phenylhydrazone (FCCP) that can cause depolarization of proton gradient across the inner membrane of mitochondria resulting a temperature increase instead of ATP synthesis[15,16,32]. Furthermore, temperature imaging with gTEMP suggested a temperature difference between the nucleus and cytoplasm, where the temperature in the nucleus was estimated to be higher by 2.9 ± 0.3 °C than that of cytoplasm. Because gTEMP showed a wide detection range of temperature, gTEMP was exploited to the monitoring of temperature in live medaka embryos at a medium temperature of 25 °C, which demonstrated the feasibility of *in vivo* thermometry.

Despite the advantages, there are drawbacks that would limit the application of gTEMP for cellular temperature imaging. First, Sirius[86] in gTEMP is dim compared to

some of the brightest FPs, e.g., mNeonGreen (mNG)[87]. In consequence, temperature imaging with gTEMP requires relatively strong irradiation or long exposure time. These may cause photodamage to the indicator protein as well as a cell or tissue, and decrease temporal resolution. Second, gTEMP utilized ultraviolet (UV) excitation that may restrict its biocompatible applications in live-cell imaging because of the phototoxicity. Additionally, UV irradiation also generates excessive autofluorescence from some endogenous molecules such as flavins, NADH/NADPH[88], and glass material in glass-bottom dish, resulting in low signal-to-background. Thus, it is needed to develop a new GETI that would overcome the limitations of gTEMP for a friendly-biocompatible temperature imaging in live cells.

Previously, a former lab member Asst. Prof. Masahiro Nakano has screened several FPs that can be excited with visible excitation and found that tdTomato[89] (tdT) showed the largest temperature sensitivity and mNeonGreen[87] (mNG) showed the smallest temperature sensitivity among the examined FPs. Thus, a fusion of mNG-tdT was expected to be a GETI with a blue excitation light, and this fusion protein was denoted as blue-excited genetically encoded temperature indicator, B-gTEMP, as an improved version of gTEMP.

Here, I aim to evaluate temperature-sensing performance of B-gTEMP in vitro characterization and to examine its specificity to temperature. I also make a comparison between B-gTEMP and gTEMP in serval aspects of macromolecular crowding, autofluorescence, signal-to-background, temperature resolution, and phototoxicity. I apply B-gTEMP to the intracellular temperature measurement in live HeLa cells. I demonstrated the temperature-sensing performance of B-gTEMP to monitor temperature changes with a local heat spot, to visualize heat production in mitochondria with chemical stimulation, and to investigate the temperature in the nucleus and cytoplasm of live HeLa cells.

3.2 Materials and methods

Gene construction. I constructed B-gTEMP by fusing mNG and tdTomato (tdT), and a reference fusion protein by fusing mNG and mScarlet (mS). For gene construction of B-gTEMP, I amplified the cDNA of mNG with *Bam*HI/*Kpn*I restriction enzyme sites, and the cDNA of tdT with *Kpn*I/*Eco*RI sites. I then ligated both cDNA fragments of mNG and tdT to pRSET$_B$ vector (Invitrogen) for bacterial expression or to pcDNA3.0 vector (Invitrogen) for mammalian expression. For localizing B-gTEMP to specific subcellular compartments, I amplified the cDNA of B-gTEMP and inserted it to a pcDNA3.0 vector between the *Not*I/*Xho*I restriction sites; a nucleus export signal (MNLVDLQKKLEELELDEQQ) or a duplicated mitochondrial targeting signal of cytochrome *c* oxidase subunit VIII (sCOX8), denoted as mito-B-gTEMP, was inserted between *Hin*dIII/*Not*I restriction sites on pcDNA3.0 for cytosolic or mitochondria localization, respectively. For mNG-mS, I replaced the cDNA of tdT in the B-gTEMP gene with that of mS. I transformed all gene constructions into XL-10 Gold *E. coli* cells (200314, Agilent Technologies) and cultured in the Luria-Bertani (LB) medium with 100 μg/mL carbenicillin (Sigma-Aldrich) for 10–12 h at 37 ºC before performing plasmid purification.

Protein purification. I transformed *E. coli* strain JM109(DE3) (P9801, Promega) with pRSET$_B$ plasmid encoding B-gTEMP or mNG-mS with a N-terminal polyhistidine tag by heat shock method at 42 ºC for 45 s. I spread the transformants on a LB plate containing 100 μg/mL carbenicillin and incubated at 37 ºC for overnight. I grew *E. coli* in a 200 mL LB medium containing 100 μg/mL carbenicillin at 23 ºC for 4 days under gentle shaking at 120 rpm. I harvested the *E. coli* cells, re-dispersed them in a phosphate-buffered saline (PBS; T900, Takara Bio) containing a protease inhibitor cocktail (11873580001, Roche Diagnostics), and ultrasonicated to lyse the cells. Next, I purified proteins with Ni-NTA chromatography (30230, Qiagen) and eluted them from the column with a TN buffer (10 mM Tris-HCl pH 8.0 and 150 mM NaCl) supplemented with 200 mM imidazole (099-00013, FUJIFILM Wako). Finally, I exchanged the solvent of the protein solution with a 20 mM HEPES buffer (pH 7.4) by applying on a PD-10 desalting column (17085101, GE Healthcare) equilibrated with the buffer. I concentrated the protein by ultrafiltration using

a 30 kDa molecular weight cut-off filter (UFC803024, Amicon Ultra-4, Merck Millipore), quickly frozen the protein solution in liquid nitrogen and stored at −80 °C.

***In vitro* characterization.** I performed fluorescence measurement with scanning temperature from 15 to 50 °C by an FP-750 spectrofluorometer (JASCO) equipped with a temperature controller unit (ETC-272T, JASCO). I diluted proteins in a MOPS buffer (20 mM MOPS, 150 mM KCl, pH 7.3) to 0.2 μM, loaded into a quartz cuvette. I took 5 min to wait for the stabilization of temperature at each temperature point before starting the fluorescence measurement. I set the excitation wavelength at 470 nm. For comparison with microscopy data, I integrated the FI of 580–600 nm and 500–540 nm, which I denoted as F_R and F_G, respectively. Then, I calculated a fluorescence ratio by F_R/F_G.

To examine the effect of salts, I added a salt such as NaCl, $CaCl_2$, or $MgCl_2$ to the 20 mM MOPS buffer containing 150 mM KCl, pH 7.3. For 0 mM of $CaCl_2$ and $MgCl_2$, I added EDTA to the final concentration of 1mM to the solution. For pH dependence measurement, I prepared a mixture of 150 mM KCl, 30 mM trisodium citrate, and 30 mM borax adjusted to pH 8.0, 7.0, 6.0, and 5.0 by titrating with HCl. To investigate the effect of macromolecular crowding, I dissolved Ficoll PM70 powder (F2878, Sigma-Aldrich) in an aqueous buffer solution containing 10 mM sodium phosphate, 100 mM NaCl, and 2 mg/mL BSA (pH 7.3) as described in ref.[71] To study the effect of heating-cooling cycles, I measured fluorescence in cycles of temperature change between 30 to 40 °C with an interval of 5 min.

Acceptor photobleaching. I measured the FRET efficiency of B-gTEMP and mNG-mS expressed in HeLa cells by the acceptor photobleaching FRET method[90]. To perform photobleaching of the acceptor of tdT in B-gTEMP or mS in mNG-mS, I used a 561 nm laser beam and a Ti2 microscope (Nikon) equipped with a confocal unit (Dragonfly 200, Andor Technology). After three days of transfection, HeLa cells were fixed with 4% paraformaldehyde at room temperature for 30 min. I performed the photobleaching of tdT in B-gTEMP by continuously irradiating 561 nm laser beam (maximum power) for 30 min, whereas the photobleaching of mS in mNG-mS for 15 min. I measured the fluorescence intensity of mNG before and after photobleaching by an EM-CCD camera

(iXon Ultra, Andor) through a bandpass filter (FF01-520/35, Semrock). The FRET efficiency was calculated as:

$$E = \frac{I_{\mathrm{mNG(post-bleac\ )}} - I_{\mathrm{mNG(pre-bleach)}}}{I_{\mathrm{mNG(post-bleac\ )}}} \times 100\%, \quad (5)$$

where E is FRET efficiency, $I_{\mathrm{mNG(post\text{-}bleach)}}$ is the fluorescence intensity of mNG after photobleaching and $I_{\mathrm{mNG(pre\text{-}bleach)}}$ is the fluorescence intensity of mNG before photobleaching.

Phototoxicity of B-gTEMP and gTEMP. I illuminated cells expressing B-gTEMP with a visible light (center wavelength, 472 nm; band width, 30 nm; power density, 0.34 W/cm^2), whereas I illuminated cells expressing gTEMP with a UV light (center wavelength, 370 nm, band width, 36 nm; power density, 0.34 W/cm^2). I captured images every 5 min on an inverted microscope (Ti-E, Nikon) equipped with a Plan Fluor 40×1.3 NA oil immersion objective lens (Nikon), a motorized-stage (BIXY Chuo Precision Industrial), a stage-top incubator with supply of air containing 5% CO_2 (INUB-ONICS, Tokai Hit), and a sCMOS camera (ORCA Flash4.0, Hamamatsu Photonics). The exposure time was 100 ms and the medium temperature was 37 °C.

For B-gTEMP imaging, I used a filter cube made of an excitation filter of FF02-472/30 (Semrock) and a dichromic mirror of FF495-Di03 (Semrock). Emission filters of mNG (FF01-520/35, Semrock) and tdT (FF01-589/15, Semrock) were inserted in a filter wheel unit (MAC6000, Ludl Electronic Products). For gTEMP imaging, I used another filter cube made of an excitation filter of FF01-370/36 (Semrock) and a dichromic mirror of CFW-Di01-Clin (Semrock). The emission filters were FF01-440/40 (Semrock) and FF01-520/35 (Semrock) for Sirius and mT-Sap, respectively.

To detect dead cells, I stained dead cells with propidium iodine[91] (PI; P3566, Thermo Fisher Scientific) at a final concentration of 1 μg/mL during the time-lapse imaging with FF02-472/30 (Semrock) and FF01-732/68nm (Semrock) bandpass filters for excitation and emission, respectively. The exposure time was 500 ms for PI imaging.

I calculated the percentage of live cells as:

$$\text{Live cells (\%)} = \frac{(\text{total fluorescent cells} - \text{dea\ \ cells})}{\text{Total fluorescent cells}} \times 100, \quad (6)$$

where dead cells were counted from images of PI staining.

Cell culture and transfection. I cultured HeLa cells in Dulbecco's modified Eagle medium (DMEM; D6046, Sigma-Aldrich) supplemented with 10% fetal bovine serum (FBS; Biowest) at 37 °C in a 5% CO_2 incubator. I seeded the cells on in-house-made glass bottom dishes and grew up to 50–60% of cell confluence before performing transfection. For transfection, I mixed 2.0 μg of plasmids and 5.0 μg of polyethylenimine MAX (24765-1, Polysciences) in 200 μL of Opti-MEM media (31985-070, Thermo Fisher Scientific), and incubated for 20 min at room temperature. Subsequently, I added the mixture to a medium containing HeLa cells, and exchanged the culture media at 6 h after the mixing. I cultured cells for ~72 h and exchanged the medium to DMEM/F12 (11039-021, ThermoFisher Scientific) without phenol red before microscopy observation.

Cell imaging. I performed cell imaging with an inverted microscope (Ti-2, Nikon) with an air conditioner to maintain the room temperature at 25 °C. The microscope was equipped with a Plan Apo λ 60×1.40 numerical aperture (NA) oil objective lens (Nikon), a LED light source (Niji Bluebox, power 1%), a stage-top incubator with 5% CO_2 supply (STXG-WSKMX, Tokai Hit), and a dual-view optics (W-View GEMINI 2C, Hamamatsu photonics). For B-gTEMP imaging, I used a dichroic mirror (FF495-Di03, Semrock) and an excitation filter (FF01-482/18, Semrock). I used a dual-view optics equipped with a dichroic mirror (FF560-FDi02, Semrock) and emission filters of FF01-589/15 (Semrock) for tdT or mS and FF01-520/35 (Semrock) for mNG. I captured fluorescence images from mNG and tdT separately by two scientific complementary metal oxide semiconductor (sCMOS) cameras (ORCA Flash4.0, Hamamatsu Photonics) synchronized by a TTL signal from a delay pulse generator (Sapphire Plus, Quantum Composer). The exposure time was 100 ms and the binning of the sCMOS was 2×2 pixels.

I measured fluorescence ratios F_R/F_G cell by cell to calculate average values and the standard deviation.

Heat production in mitochondria. I transfected HeLa cells with mito-B-gTEMP for mitochondria localization (see gene construction in section 2.3). I freshly dissolved an uncoupler reagent of carbonyl cyanide 4-(trifluoromethoxy) phenylhydrazone (FCCP; C2920, Sigma-Aldrich) in dimethyl sulfoxide (DMSO; D2650, Sigma-Aldrich). I added FCCP solution to the cell culture to the final concentration of 10 μM. As a negative

control, I added DMSO to the cell culture to the same final DMSO concentration as in the FCCP solution. Medium temperature was 37 °C.

Quick temperature rises by a local heat spot using carbon nanotubes (CNTs).

I prepared 1mg/mL multiwalled carbon nanotubes (CNTs) with average diameter and length of 170 nm and 5–9 μm, respectively, (659258, Sigma-Aldrich) suspended in a mixture containing 0.5 mL of Tween20 with 1.5 mL of HEPES buffer (20 mM HEPES, 25 mM KCl, and 5 mM $MgCl_2$, pH 7.0) as described in ref.[79] For imaging, I dispersed 50 μL of Tween-CNTs (1 mg/mL) into culture media containing HeLa cells expressing B-gTEMP in cytoplasm. I used an inverted microscope (Olympus, IX71) equipped with a PlanApo 60X/1.40 oil objective lens (Olympus), a Light Engine (SPECTRA X, Lumencor), a stage-top incubator (INUB-ONICS, Tokai Hit), and a dual-view optics (W-View GEMINI, Hamamatsu photonics). I used a dichroic mirror of Di01-R405/488/561/635 (Semrock) and an excitation filter was FF01-475/28 (Semrock) in the filter cube of the IX-71 microscope. I used the dual-view optics equipped with a dichroic mirror (FF560-FDi02, Semrock), emission filters of FF01-589/15 (Semrock) for tdT and FF01-520/35 (Semrock) for mNG, and a sCMOS camera (ORCA Flash4.0, Hamamatsu Photonics). To generate local heat, I irradiated a cluster of CNTs located nearby a cell with a 638 nm laser beam (Coherent). The medium temperature was 30 °C.

3.3 Results and discussion

3.3.1 Development of an improved version of gTEMP, B-gTEMP

To develop an improved version of gTEMP based on a pair of FPs with different temperature sensitivity, a former lab member Asst. Prof. Masahiro Nakano first searched for a FP with visible excitation wavelengths and large temperature dependence in the emission fluorescence intensity. Among FPs examined, tdTomato[89] (tdT) showed the largest temperature dependence of FI (**Figure 30**) with a relative temperature sensitivity ($S_{T,\mathrm{tdT}}$) of −2.9 %/ºC (**Table 2**), which was defined by **Equation 2** in the **Box 1** in **Chapter 1** and Q is replaced with F, the fluorescence intensity. In addition, he also searched for another FP which showed minimal temperature dependence and fluorescence emission separable from that of tdT (emission wavelength peak, 581 nm) so that it would be used as an internal reference for the FI of tdT for ratiometric temperature measurement. He selected mNeonGreen (mNG),[87] which had the smallest temperature dependence of FI (**Figure 30, Table 2**) with a $S_{T,\mathrm{mNG}}$ value of −0.7 %/ºC and a fluorescence spectrum peaking at 517 nm, which was separable from that of tdT. Thus, he constructed a fusion protein of mNG and tdT (**Figure 31**), denoted as a blue-excited genetically encoded temperature indicator (B-gTEMP).

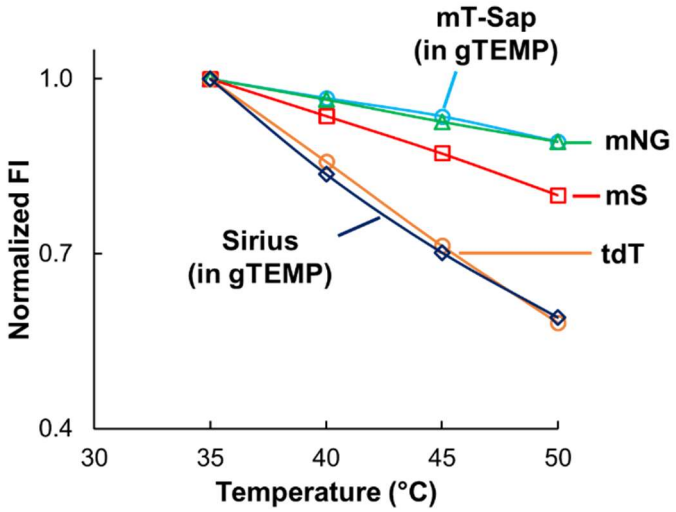

Figure 30. Plots of fluorescence intensity (FI) against temperature for purified mT-Sapphire (mT-Sap), mNeonGreen (mNG), mScarlet (mS), tdTomato (tdT), and Sirius. Their excitation wavelengths were 400, 470, 550, 550, and 350 nm, respectively, while their fluorescence emission was monitored at 509, 517, 587, 581, and 424 nm,

respectively. The proteins were dissolved in a buffer containing 20 mM MOPS and 150 mM KCl (pH 7.3).

Table 2. Physical properties of FPs involved in the study.

FPs	S_T (%/°C)[§]	λ_{ex}	λ_{em}	ε ($mM^{-1}\,cm^{-1}$)	ϕ	Relative brightness[‖]	pK_a[‡]	Ref.
Sirius	−3.0	355	424	15	0.24[†]	3.6	3.0	86
mT-Sap	−0.6	399	511	44	0.60[†]	26.4	4.9	92
mNG	−0.7	506	517	116	0.86*	99.8	5.7	87
tdT	−2.9	554	581	138	0.73*	100.7	4.7	89
mS	−1.3	569	594	100	0.72*	72.0	5.3	93

[§]Calculated from **Figure 30** and **Equation 2** in the **Box 1** in **Chapter 1**.
[†]Reported fluorescence quantum yield (ϕ)
*Measured in this study. Proteins were dissolved in a 20 mM HEPES buffer (pH 7.3) and measured the fluorescence quantum yield with a Quantarus QY absolute quantum yield spectrometer (C11347, Hamamatsu Photonics).
[‖]Relative brightness was calculated by ε×ϕ
[‡] pK_a values from references (Ref.)

Figure 31. Gene design of B-gTEMP and its reference, mNG-mS.

I tested the temperature response of purified B-gTEMP on a fluorescence spectrophotometer. B-gTEMP excited at a single wavelength of 470 nm showed two fluorescence emission bands with peak wavelengths of 517 and 581 nm, which are attributed to mNG and tdT, respectively (**Figure 32A**). When I increased the temperature from 15 to 50 °C, the tdT fluorescence from B-gTEMP showed a large decrease in the FI with temperature, whereas the mNG fluorescence showed considerably smaller decrease in the FI (**Figure 32A**), consistent with the temperature dependence of the individual FPs (**Figure 30**). Therein, I took a ratio of the integrated FI of tdT (580–600 nm), denoted as F_R, to that of mNG (500–540 nm), denoted as F_G for ratiometric temperature measurement. As shown in **Figure 32B**, the F_R/F_G ratio monotonically decreased with temperature, so that I expected that F_R/F_G would be able to be used as a measure of

temperature with one-to-one correspondence. When I performed cooling from 50 to 15 °C, F_R/F_G increased, and the values were well consistent with those in the heating (**Figure 32B**). Moreover, B-gTEMP showed an excellent reproducibility of F_R/F_G during repeated cycles of heating and cooling between 30 and 40 °C (an inset in **Figure 32A**). This indicates the high reversibility of the fluorescence change of B-gTEMP with temperature. In addition, the averaged relative temperature sensitivity $S_{T,\text{B-gTEMP}}$ of the ratio F_R/F_G between 15 and 50 °C was −2.2 ± 1.2 %/°C, where Q is replaced with R in **Equation 2**.

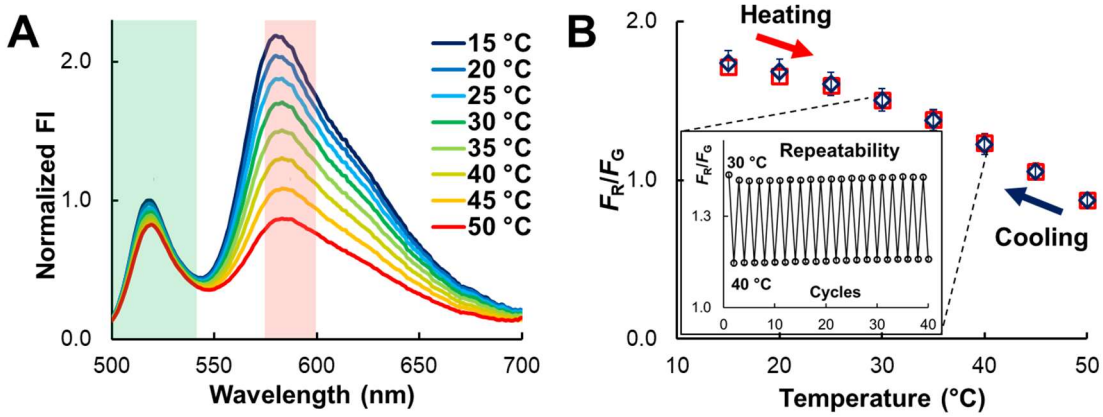

Figure 32. Temperature response of B-gTEMP. (A) Fluorescence emission spectrum of B-gTEMP at various temperatures. (B) A plot of the ratio F_R/F_G of B-gTEMP against temperature. An inset showed trajectory of F_R/F_G during heating-cooling cycles between 30 and 40 °C. Green and red transparent boxes in panel (A) indicate transmission bands used in microscopy observation. F_R and F_G in panel (B) are the integrated fluorescence intensity (FI) of 580–600 nm and 500–540 nm, respectively. The buffer contained 20 mM MOPS and 150 mM KCl (pH 7.3). Excitation wavelength was 470 nm. Data are mean ± SD (n = 3).

Additionally, I constructed a reference fusion protein composed of mNG and mScarlet[93] (mS) (**Figure 31**). Because mS showed negatively 2.2-fold smaller temperature sensitivity ($S_{T,\text{mS}}$ of −1.3 %/°C, **Table 2**) than tdT, the ratio F_R/F_G of mNG-mS was expected to be less sensitive to temperature. Although the FIs of mNG and mS in mNG-mS somewhat decreased with temperature, its F_R/F_G value showed significantly smaller temperature sensitivity ($S_{T,\text{mNG-mS}}$ = −0.6 ± 0.2 %/°C) than that of B-gTEMP (**Figure 33**).

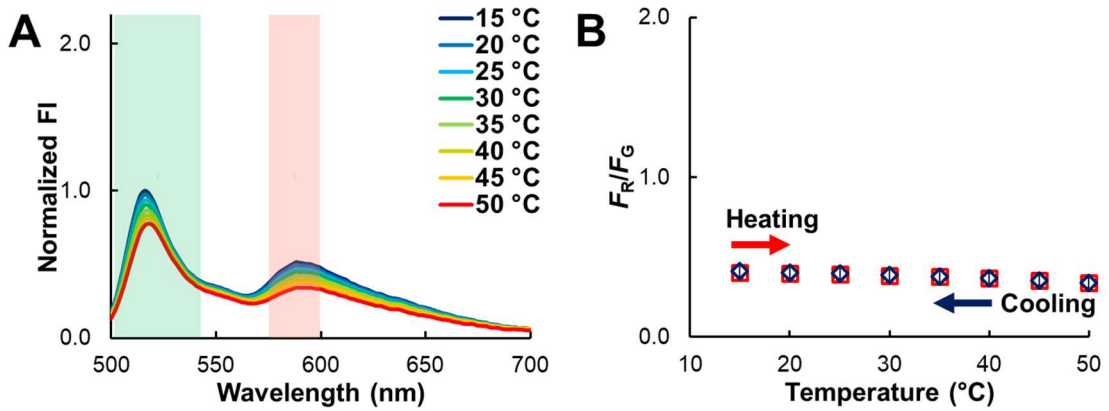

Figure 33. Temperature response of the reference, mNG-mS. (A) Fluorescence emission spectrum of mNG-mS at various temperatures. (B) A plot of the ratio F_R/F_G of mNG-mS against temperature. Green and red transparent boxes in panel (A) indicate transmission bands used in microscopy observation. F_R and F_G in panel (B) are the integrated fluorescence intensity (FI) of 580–600 nm and 500–540 nm, respectively. The buffer contained 20 mM MOPS and 150 mM KCl (pH 7.3). Excitation wavelength was 470 nm. Data are mean ± SD (n = 3).

It should be noted that Förster resonance energy transfer (FRET) occurred between mNG and tdT in B-gTEMP, as well as mNG and mS in the reference mNG-mS, so that I questioned whether FRET was responsible for the temperature sensitivity of B-gTEMP. To clarify that, I measured the FRET efficiency of B-gTEMP and the reference mNG-mS at 25 and 35 °C in fixed HeLa cells with the acceptor photobleaching method (see Materials and methods for detail). As shown in **Figure 34**, FRET efficiency of B-gTEMP was little dependent on temperature as the FRET efficiency was calculated to be 70.7 ± 3.2 % and 69.6 ± 2.8 % at 25 and 35 ºC, respectively. Similarly, mNG-mS showed almost no temperature dependence on FRET efficiency, which was calculated to be 51.0 ± 1.6 % and 51.6 ± 1.7 % for 25 and 35 ºC, respectively. These results suggested that FRET would have a small contribution to the temperature sensitivity of B-gTEMP, while the major contribution should be derived from the temperature dependence of FI and the FPs made up the indicator. Thus, B-gTEMP is not a FRET-based GETI.

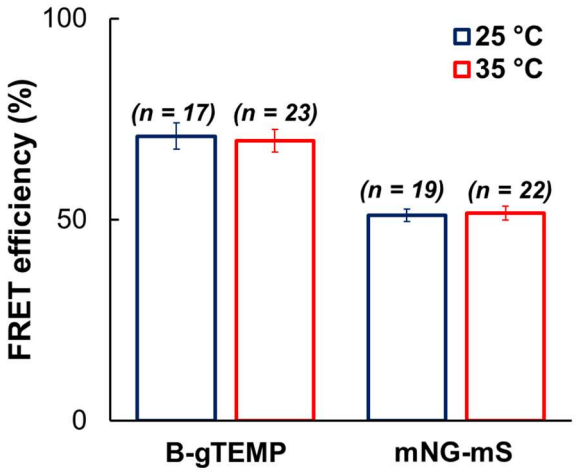

Figure 34. FRET efficiency calculated by the acceptor photobleaching method using fixed HeLa cells. The FRET efficiency of B-gTEMP was calculated to be 70.7 ± 3.2 % and 69.6 ± 2.8 % at 25 and 35 ºC, respectively, whereas that of mNG-mS was calculated to be 51.0 ± 1.6 % and 51.6 ± 1.7 % for 25 and 35 ºC, respectively. Data represents mean ± SD (*n* = cells).

3.3.2 *In vitro* characterization of B-gTEMP

To evaluate the specificity of fluorescence response of B-gTEMP to temperature, I tested the dependence of F_R/F_G on other factors such as ionic strength (I_s), salts, self-concentration, and pH. To examine the effect of ionic strength on F_R/F_G of purified B-gTEMP, I used KCl as an additive to modify I_s of B-gTEMP solutions, because K^+ is generally the most abundant cation species in cytoplasm (~150 mM)[94] and Cl^- is also an abundant anion species in mammalian cells. As shown in **Figure 35A**, the temperature response of F_R/F_G in the range of 15–50 °C was almost unaffected by I_s for I_s = 60–210 mM (the ionic strength due to the MOPS buffer (10 mM) and KCl), although F_R/F_G at I_s = 10 mM showed slightly deviated F_R/F_G values. However, the deviation of F_R/F_G at I_s = 10 mM should not affect temperature imaging in cells, since I_s in mammalian cells is usually ~150 mM[94]. To examine the effects of other factors, I used 150 mM KCl as a basal constituent of the sample solutions. The value of F_R/F_G was almost unaffected by the addition of salts such as NaCl, $CaCl_2$, and $MgCl_2$ (**Figure 35B–D**), and was little dependent on the B-gTEMP concentration itself (**Figure 36**). The value of F_R/F_G was also almost stable in a pH range of 6–8, although F_R/F_G showed small deviation at pH ~5

(**Figure 37**). Thus, the results indicate that B-gTEMP is likely to be a specific and sensitive indicator to measure temperature in live cells.

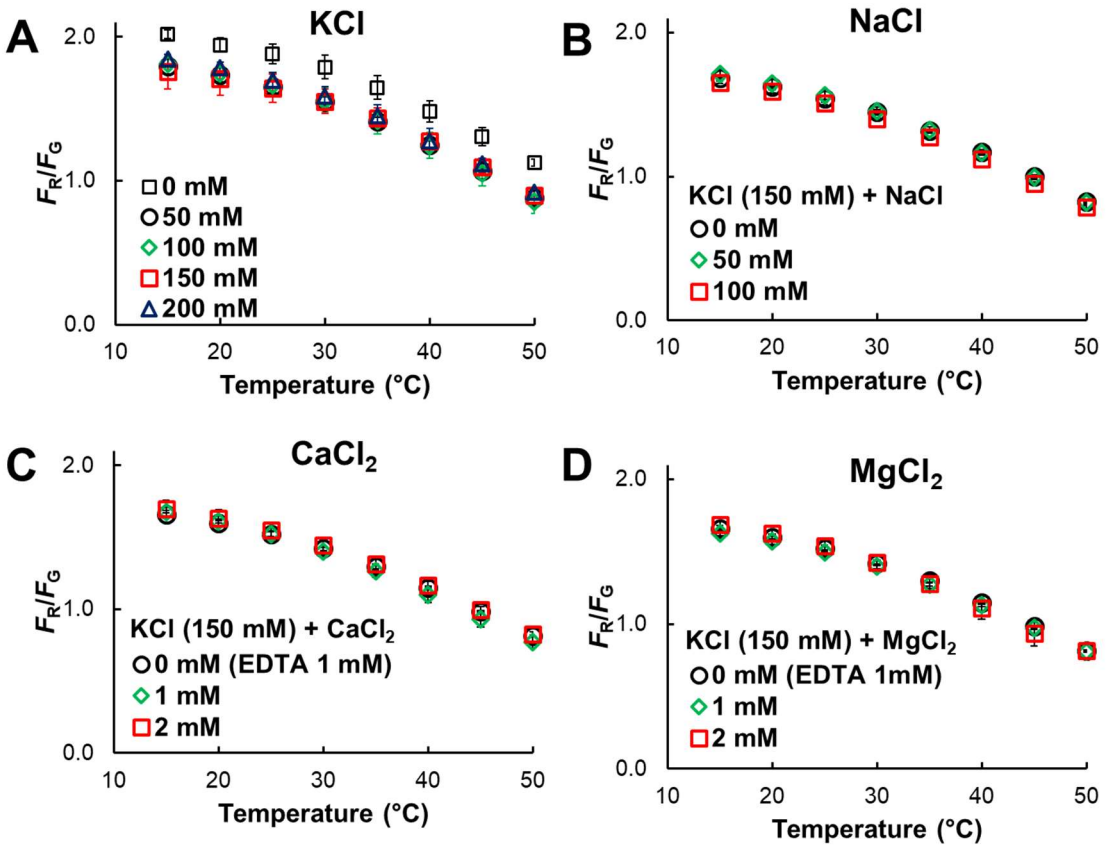

Figure 35. Effect of some salts on the fluorescence response of B-gTEMP to temperature. (A) The effect of ionic strength on the temperature dependence of F_R/F_G using KCl as an additive. The B-gTEMP solution contained 20 mM MOPS buffer (pH 7.3) and KCl (0–200 mM). The ionic strength of the MOPS buffer was 10 mM. (B–D) The effects of (B) NaCl, (C) $CaCl_2$, and (D) $MgCl_2$ on the temperature dependence of F_R/F_G. The B-gTEMP solution contained 20 mM MOPS buffer, 150 mM KCl (pH 7.3), and one of the salts. For 0 mM of $CaCl_2$ and $MgCl_2$, I added EDTA to the final concentration of 1 mM to the solution. Excitation wavelength was 470 nm. Data are mean ± SD (n = 3).

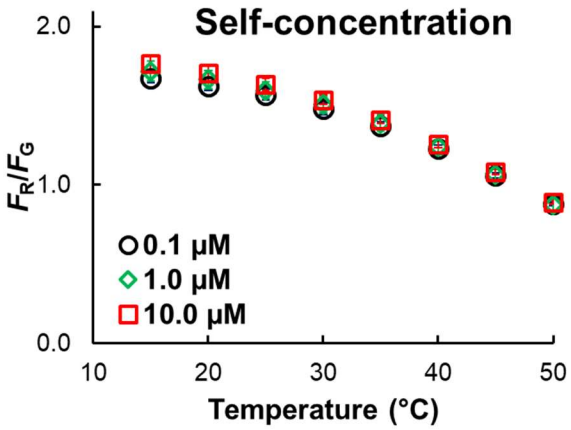

Figure 36. Temperature dependence of F_R/F_G at different B-gTEMP concentrations. The B-gTEMP solution contained 20 mM MOPS buffer and 150 mM KCl (pH 7.3). Excitation wavelength was 470 nm. Data are mean ± SD (n = 3).

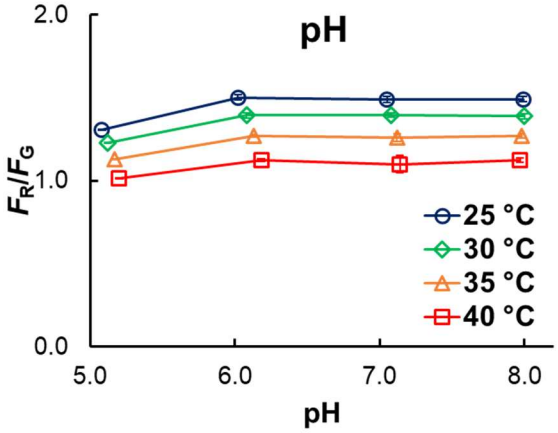

Figure 37. Effect of pH on the temperature dependence of F_R/F_G. The B-gTEMP solution contained 150 mM KCl, 30 mM trisodium citrate, and 30 mM borax, whose pH was adjusted by adding HCl. The pH values of the solution were directly measured at different temperatures. Excitation wavelength was 470 nm. Data are mean ± SD (n = 3).

3.3.3 Comparison between B-gTEMP and gTEMP

I investigated the influence of macromolecular crowding on the temperature response of purified B-gTEMP and gTEMP. I measured the dependence of fluorescence ratio on Ficoll PM70 as a widely-used macromolecular crowding reagent. Although the macromolecular crowding in HEK293 cells was reported to be equivalent to 20% (w/w) Ficoll PM70[71], the ratio F_R/F_G of B-gTEMP was observed to be only slightly affected by Ficoll PM70 especially at low temperature of ≤25 °C, even with Ficoll PM70 concentration ≥30% (w/w) (**Figure 38A**). In contrast, the fluorescence ratio of gTEMP was significantly affected by Ficoll PM70 (**Figure 38B**), which should be attributed to a difference in Ficoll PM70 dependence between mT-Sap and Sirius, whereas mNG and tdT showed a similar dependence (**Figure 39**). This result indicated that B-gTEMP would be more specific to temperature than gTEMP.

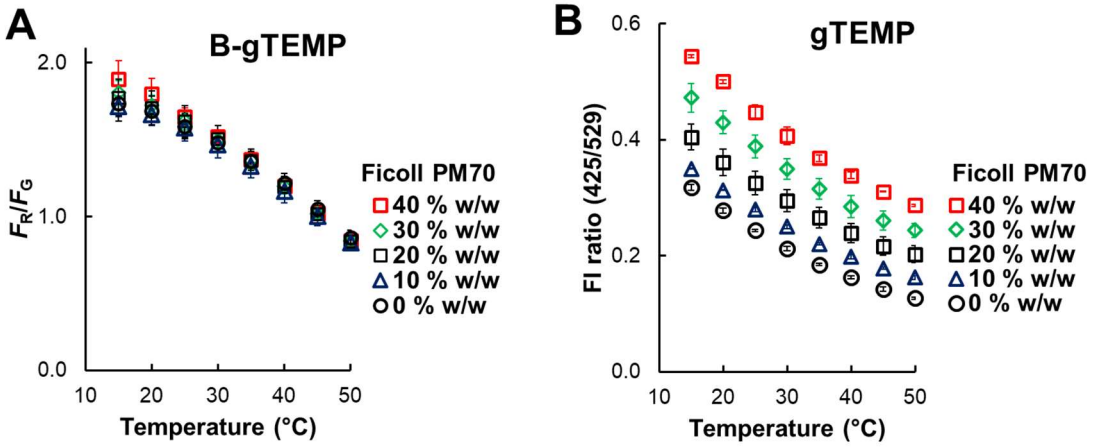

Figure 38. Comparison of the effect of Ficoll PM70 on the fluorescence ratio of (A) B-gTEMP and (B) gTEMP. The solution contained 10 mM sodium phosphate, 100 mM NaCl, 2 mg/mL BSA (pH 7.4), and Ficoll PM70 (0–40% w/w), as described in ref[71]. The excitation wavelengths were 470 nm and 370 nm for B-gTEMP and gTEMP, respectively. Data are mean ± SD.

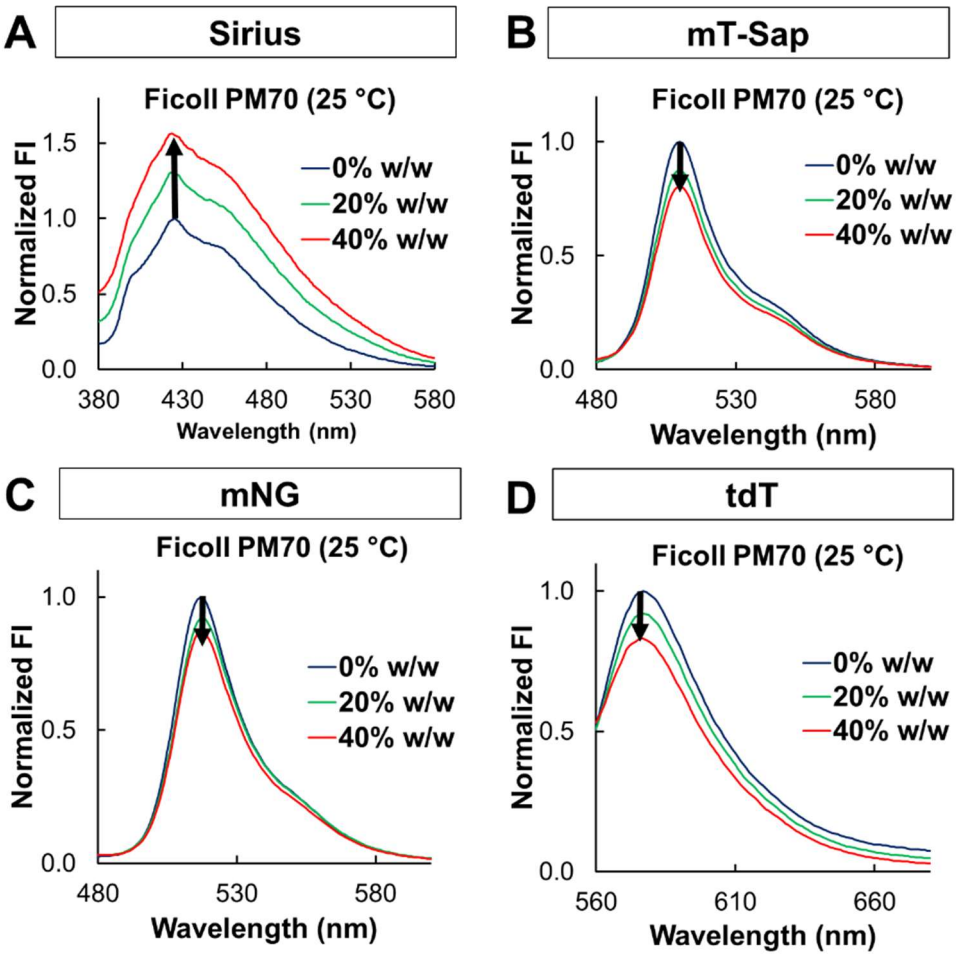

Figure 39. Effect of Ficoll PM70 as a macromolecular reagent on the fluorescence intensity of (A) Sirius, (B) mT-Sap, (C) mNG, and (D) tdT. The proteins were dissolved in a buffer containing 0–40% (w/w) Ficol PM70, 10 mM sodium phosphate, 100 mM NaCl, and 2 mg/mL BSA (pH 7.4). The excitation wavelength was 350, 400, 470, and 550 nm for Sirius, mT-Sap, mNG, and tdT, respectively.

Next, I compared B-gTEMP and gTEMP in microscopy observation of live-cell imaging in terms of autofluorescence and phototoxicity. For autofluorescence, I measured the background of images with no cells and untransfected HeLa cells from fluorescence channels of mNG and tdT in B-gTEMP, and Sirius and mT-Sap in gTEMP (**Figure 40**). I used the same microscopy setup as in phototoxicity experiment (see Phototoxicity of B-gTEMP and gTEMP the materials and methods for detail). The exposure time was 100 ms and the power density of excitation was the same (0.34 W/cm^2) for both B-gTEMP (center wavelength, 472 nm; band width, 30 nm) and gTEMP (center wavelength, 370 nm; band width, 36 nm). As shown in **Figure 40A**, the background of fluorescence

channels of Sirius and mT-Sap in gTEMP was significantly higher than that of mNG and tdT in B-gTEMP. No difference between no cells and untranfected cells was observed suggesting that the autofluorescence was mostly derived from the bottom glass. In addition, because mNG and tdT were brighter than Sirius and mT-Sap (see relative brightness in **Table 2**), I calculated signal-to-background ratios from HeLa cells expressing B-gTEMP or gTEMP and untransfected HeLa cells. As shown in **Figure 40B**, the signal-to-background ratio of mNG and tdT was significantly higher by ~66- and 180-fold than that of Sirius, respectively, and by ~10- and 27-fold than that of mT-Sap, respectively.

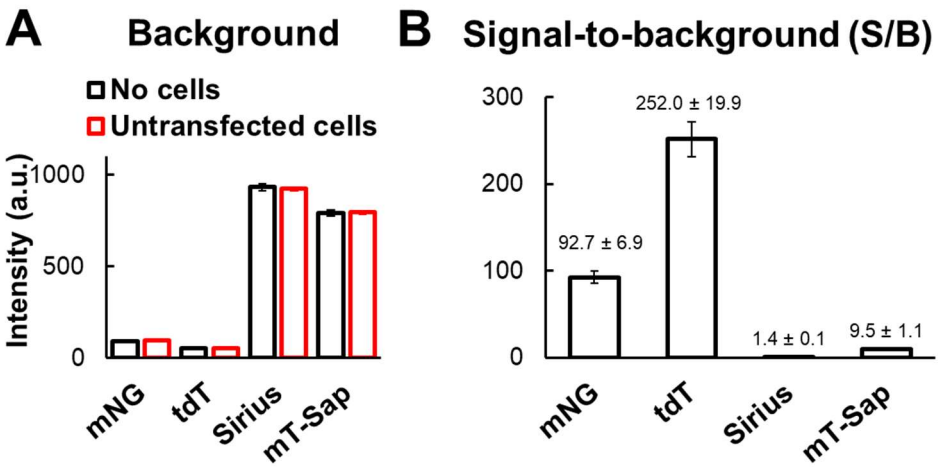

Figure 40. Comparison of background autofluorescence and signal-to-background (S/B) between B-gTEMP and gTEMP. (A) Background signals in microscopy observation of no cells (n = 5) and untransfected HeLa cells (n = 135) of fluorescence channels of mNG and tdT in B-gTEMP, and Sirius and mT-Sap in gTEMP. (B) Signal-to-background ratios of live HeLa cells expressing B-gTEMP (n = 135) or gTEMP (n = 125). The exposure time was 100 ms with the same power density of excitation for B-gTEMP and gTEMP. Fluorescence signals were subtracted to the camera offset. Data are mean ± s.e.m.

Because the temperature resolution (δT, see **Box 1** in **Chapter 1**) is related to the signal-to-background noise, I therefore compared the δT between B-gTEMP and gTEMP under the same imaging condition (i.e., exposure time, 100 ms; power of excitation, 0.34 W/cm^2). As shown in **Figure 41**, the δT of B-gTEMP showed 88.8-fold higher than that

of gTEMP. This suggests that microscopy observation with B-gTEMP would require much less power of irradiation or shorter exposure time than that with gTEMP.

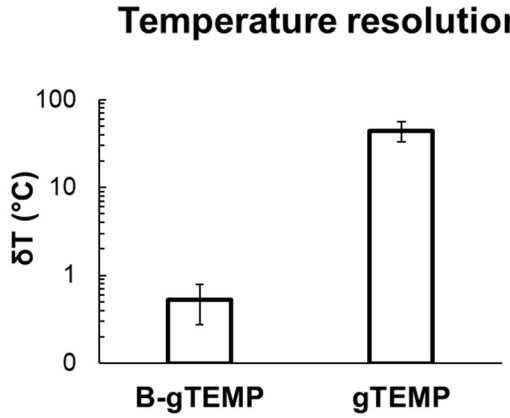

Figure 41. Comparison of temperature resolution between B-gTEMP and gTEMP at the same imaging condition. The exposure time was 100 ms with the same power density (0.34 W/cm^2) of excitation for B-gTEMP and gTEMP. Fluorescence signals were subtracted to the camera offset. Data are mean ± SD.

For phototoxicity, I performed a phototoxicity experiment in HeLa cells expressing B-gTEMP or gTEMP encountered in fluorescence microscopy observation. When I continuously illuminated cells expressing B-gTEMP with a visible excitation light (center wavelength, 472 nm; band width, 30 nm; power density, 0.34 W/cm^2) to observe the fluorescence of mNG and tdT, the cells started dying around 2 h, as detected by propidium iodine staining of DNA[91] (red trajectory, **Figure 42A**). In contrast, when I continuously illuminated cells expressing gTEMP with a UV excitation light (center wavelength, 370 nm; band width, 36 nm) at the same power density as in the B-gTEMP observation, the cells started dying around 50 min (black trajectory, **Figure 42A**), significantly earlier than the cells irradiated with the visible excitation light. The half-lives were 3.5 and 1 h for cells continuously irradiated with the visible and UV excitation lights for B-gTEMP and gTEMP, respectively. Thus, HeLa cells were more vulnerable to the observation condition of gTEMP than that of B-gTEMP.

I also examined intermittent illumination of an excitation light, which is often-used observation sequence for long-term imaging. I illuminated HeLa cells expressing B-gTEMP with the visible light (see above) for 100 ms to acquire mNG and tdT images, and repeated the acquisition every 5 min. The cells showed little cell death and remained

viable (red trajectory, **Figure 42B**), but the cells expressing gTEMP with intermittent irradiation of UV light started dying at around 11 h (black trajectory, **Figure 42B**). It should be noted that the fluorescence of Sirius in gTEMP under the exposure time of 100 ms was too dim to be imaged. To evaluate the phototoxicity under realistic imaging condition for gTEMP, I performed another experiment of intermittent UV irradiation with the exposure times adapted from temperature imaging of gTEMP[15], which was 1500 and 500 ms for Sirius and mT-Sap, respectively. Unfortunately, cells died around 4 h under this gTEMP-adapted imaging condition (data not shown). Thus, these results clearly demonstrated that temperature imaging with B-gTEMP inflicted less phototoxicity than that with gTEMP.

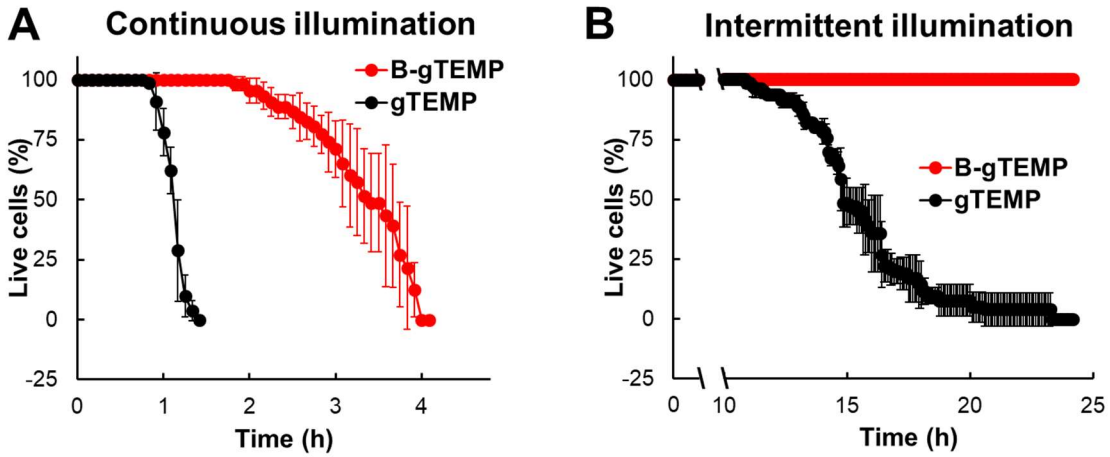

Figure 42. Comparison of phototoxicity between B-gTEMP and gTEMP. (A) Time courses of the viability of cells expressing B-gTEMP (n = 87) or gTEMP (n = 94) with continuous illumination of excitation. (B) Time courses of the viability of cells expressing B-gTEMP (n = 91) or gTEMP (n = 95) with intermittent illumination of excitation. Cells expressing B-gTEMP were illuminated with a visible light (center wavelength, 472 nm; band width, 30 nm; power density, 0.34 W/cm^2), whereas cells expressing gTEMP were illuminated with a UV light (center wavelength, 370 nm; band width, 36 nm; power density: 0.34 W/cm^2). Images were captured every 5 min with the exposure time of 100 ms with continuous or intermittent illumination. Medium temperature was 37 °C. Data are mean ± SD.

Additionally, in the observation of cells expressing B-gTEMP or gTEMP, photobleaching was observed to occur. However, as shown in **Figure 43** mNG and tdT showed slower photobleaching than Sirius and mT-Sap, suggesting that B-gTEMP would

likely to have higher photostability than gTEMP (as I demonstrated in the **section 3.3.5**). Thus, B-gTEMP should be more suitable for long-term temperature imaging than gTEMP.

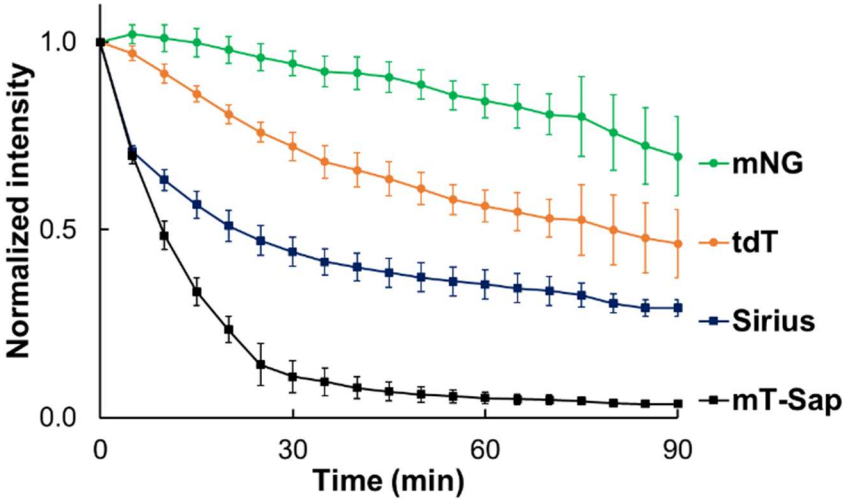

Figure 43. Photobleaching of mNG, tdT, Sirius, and mT-Sap in live HeLa cells under the microscopy observation condition of B-gTEMP or gTEMP. The cells were continuously irradiated with a light at 370 nm (band width, 36 nm, power density, 0.34 W/cm^2) for Sirius and mT-Sap (n = 13), a light at 470 nm (band width, 28 nm, power density, 0.34 W/cm^2) for mNG and tdT (n = 10). Data represents mean ± SD.

3.3.4 Temperature response of B-gTEMP in live HeLa cells

To test the temperature-sensing performance of B-gTEMP in live cells, I measured the ratio F_R/F_G of B-gTEMP in the cytoplasm of HeLa cells between 30 and 40 °C. The ratio F_R/F_G from B-gTEMP in cells also showed a decrease with temperature (**Figure 44A**) and the temperature sensitivity $S_{T,\text{B-gTEMP}}$ was −1.8 ± 0.1 %/°C (in a range of 37–40 °C), almost consistent with the data of purified B-gTEMP (**Figure 32B**). However, the ratio F_R/F_G from cells was slightly different from the data of purified protein (**Figure 32B**), presumably because of differences in the environment of B-gTEMP (an aqueous buffer solution and cytoplasm for **Figure 32B** and **Figure 44A**, respectively) as well as measurement setup (fluorescence spectroscopy and fluorescence microscopy for **Figure 32B** and **Figure 44A**, respectively). In contrast, the reference of mNG-mS responded to temperature at a lower temperature sensitivity ($S_{T,\text{mNG-mS}}$, −1.1 ± 0.2 %/°C in a range of

37–40 °C) (**Figure 44B**). In addition, I calculated the temperature resolution (δT) in estimated temperature through F_R/F_G measured from B-gTEMP (see **Equation 3** in the **Box 1** in **Chapter 1**) and found that the temperature resolution of B-gTEMP was 0.5–0.8 ºC in a range of 30–40 °C, and that of mNG-mS was >2 °C (**Figure 45**).

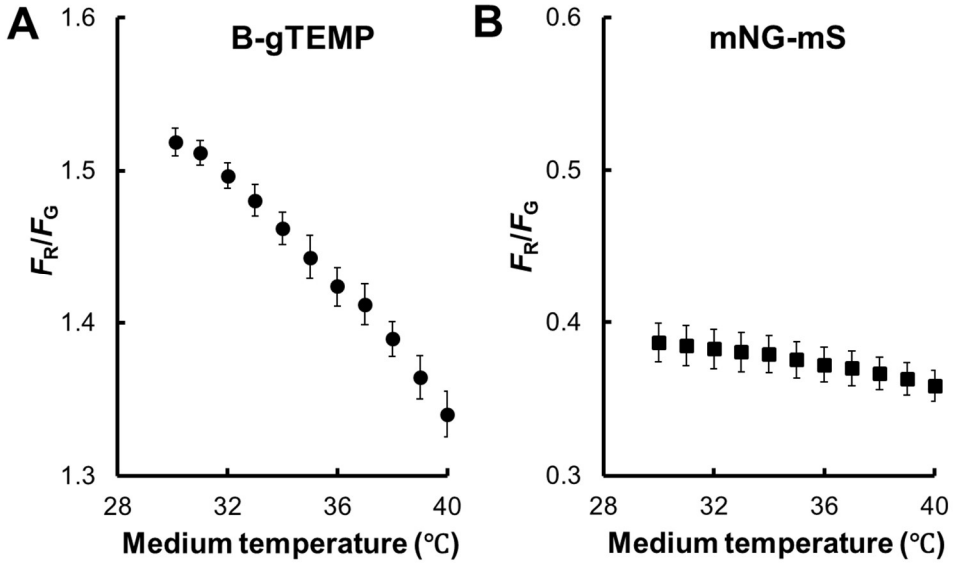

Figure 44. Fluorescence response of B-gTEMP and mNG-mS in live HeLa cells. (A) Intracellular temperature response of B-gTEMP in cytoplasm of live HeLa cells (n = 11). (B) Intracellular temperature response of mNG-mS in cytoplasm of live HeLa cells (n = 13). Data are mean ± SD.

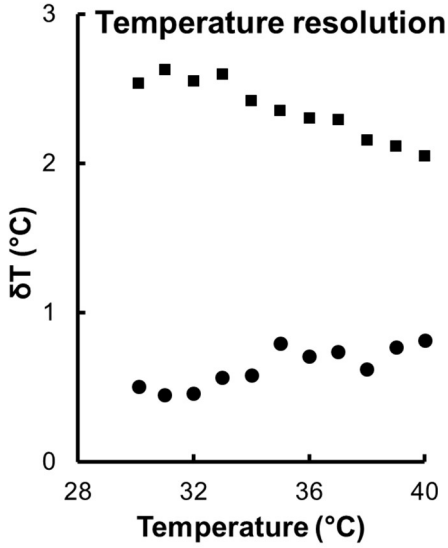

Figure 45. Temperature resolution (δT) in estimated temperature through F_R/F_G measured by B-gTEMP and mNG-mS. The data were derived from **Figure 44** using **Equation 3** in the **Box 1** in **Chapter 1**.

3.3.5 Application of B-gTEMP to monitor quick temperature rises with a local heat spot

I employed B-gTEMP to monitor quick temperature rise with an external heat source. I dispersed carbon nanotubes (CNTs) in a medium containing HeLa cells expressing B-gTEMP, and irradiated a cluster of CNTs in the neighbor of cells with a focused laser beam (wavelength, 638 nm) to locally produce heat. Temperature change in cells was monitored through the fluorescence of B-gTEMP (**Figure 46**). Previously, laser irradiation of CNTs has been used for locally increasing temperature surrounding motor proteins,[79] and producing a steep temperature gradient in the neighbor of cells.[16,33] As shown in **Figure 46A**, when I irradiated the CNTs with the laser beam, a decrease of the ratio F_R/F_G in a HeLa cell near the CNTs was observed, which indicated temperature increase. The ratio F_R/F_G, i.e., temperature, immediately returned to the original value when I turned off the laser beam. Furthermore, the time trajectories of temperature at regions of interest (ROI) 1–3 (**Figure 46B**), which was calculated from the ratio F_R/F_G at ROI 1–3 in reference with the calibration curve (**Figure 44A**), showed that the read-out of temperatures from B-gTEMP reversibly responded to the laser irradiation of the CNTs.

The plateau temperatures negatively correlated with the distance from the CNTs (distances from the CNTs were 7, 14, and 21 μm for ROI 1, 2, and 3, respectively). Furthermore, the temperature increase at ROI 1 well correlated with the laser power (**Figure 46C**), i.e., the higher the laser power, the larger the temperature increase became. These results underpinned that the read-out from B-gTEMP really provided the spatiotemporal dynamics of temperature in cells. In addition, the rising and the falling of temperature were observed to occur almost at the same time among ROI 1–3 (**Figure 46B**). These data suggest that B-gTEMP should respond to temperature change faster than 10 ms.

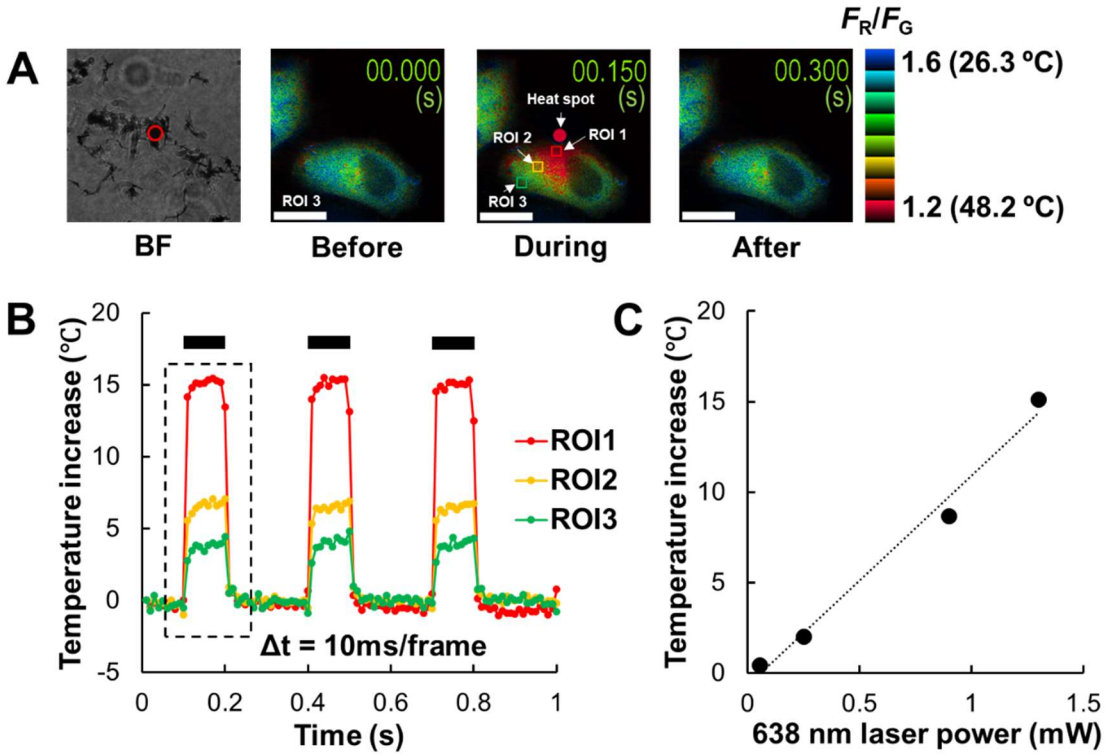

Figure 46. Applications of B-gTEMP for tracking temperature change in live cells. (A) Bright filed (BF) and pseudo-colored ratio images before, during, and after local heating. The red circle indicates heat spot. The color bar indicates fluorescence ratio F_R/F_G. (B) Temperature increase estimated from the calibration curve (**Figure 44A**) as the function of time. A CNTs cluster located nearby a cell was irradiated with a 638 nm laser at a power of 1.3 mW. Black lines indicate the periods of laser irradiation. The exposure time was 10 ms. (C) Temperature increase at ROI 1 as a function of laser power at 638 nm. The medium temperature was 30 °C. Scale bar, 20 μm.

Additionally, as shown in **Figure 47A**,**B**, gTEMP also exhibited a rapid response to temperature change like B-gTEMP. However, gTEMP showed a decrease of ratio with time, which should be attributed to the photobleaching of mT-Sap, while B-gTEMP showed complete reversibility of the ratio (**Figure 46B**). This indicates that B-gTEMP would have higher photostability than gTEMP. In contrast, ELP-TEMP showed a slow response speed with the half-life (τ) of 108 and 112 ms for the rising and falling temperature, respectively (**Figure 47C**,**D,E**). This slow response may derive from the kinetic of conformation change of the ELP moiety in ELP-TEMP. Thus, ELP-TEMP is not suitable for the application of high-speed temperature imaging with a time resolution <100 ms.

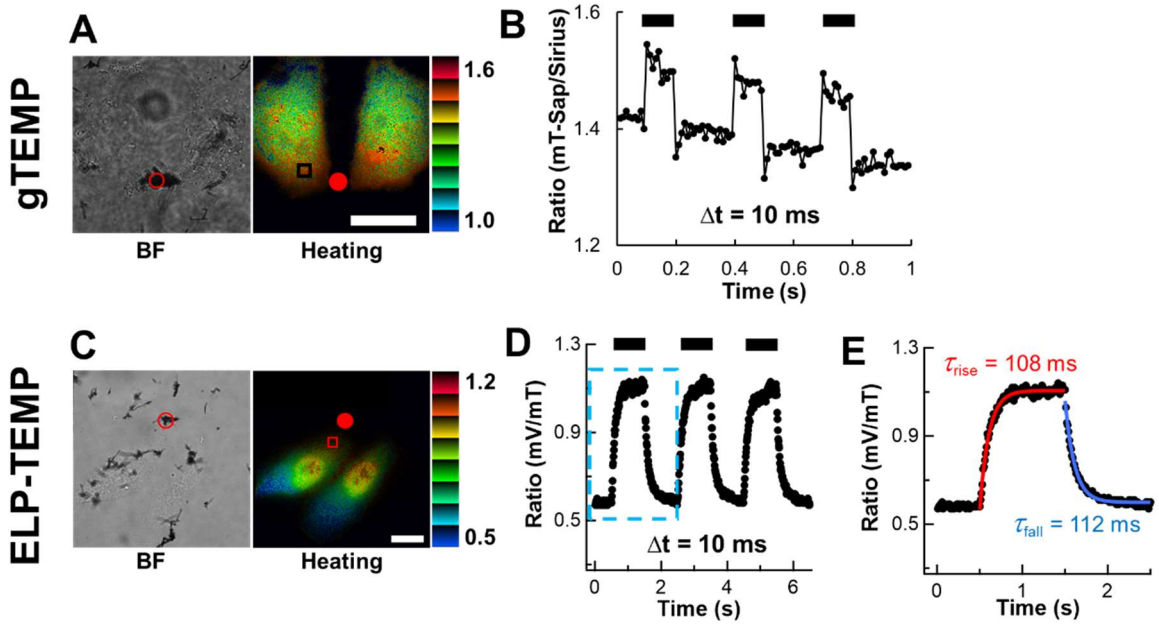

Figure 47. Comparison of temperature response of gTEMP (upper) and ELP-TEMP (lower) at a time resolution of 10 ms. (A) Bright-field (BF) and pseudo-colored ratio images of HeLa cells expressing gTEMP during local heating. (B) A plot of ratio of mT-Sap/Sirius against time. (C) BF and pseudo-colored ratio images of HeLa cells expressing ELP-TEMP during local heating. (D) A plot of ratio of mV/mT against time. (E) An expand of blue box in panel (D). Red and blue lines indicate exponential fitting for the rising and falling, respectively, with the half-time (τ). Red circles indicate the heat spot. Black lines indicate the periods of laser irradiation. The medium temperature was 30 and 34 °C for gTEMP and ELP-TEMP, respectively. The color bar indicates fluorescence ratio. The scale, 20 μm.

3.3.6 Application of B-gTEMP to monitor heat production in mitochondria by treatment of an uncoupling reagent

I employed B-gTEMP to detect a temperature change arising from the depolarization of proton gradient across the inner membrane in mitochondria with the addition of carbonyl cyanide 4-(trifluoromethoxy)phenylhydrazone (FCCP), an uncoupling reagent[15,16,32]. To measure temperature inside mitochondria, I fused B-gTEMP with a duplex of mitochondria target sequence of cytochrome *c* oxidase VIII (mito-B-gTEMP) to localize the nanothermometer in mitochondria. As shown in **Figure 48**, when I added 10 μM FCCP to HeLa cells, I were able to detect a temperature rise of 1.8 ± 0.6 °C in mitochondria as estimated from a calibration curve in **Figure 49**, where B-gTEMP was localized in mitochondria. As a negative control, adding DMSO, the solvent for FCCP, did not raise the temperature in mitochondria (**Figure 48B**). The data demonstrated that B-gTEMP was able to detect heat production in mitochondria from the depolarization of proton gradient by FCCP treatment. Thus, B-gTEMP would be useful for tracking temperature involving cellular processes.

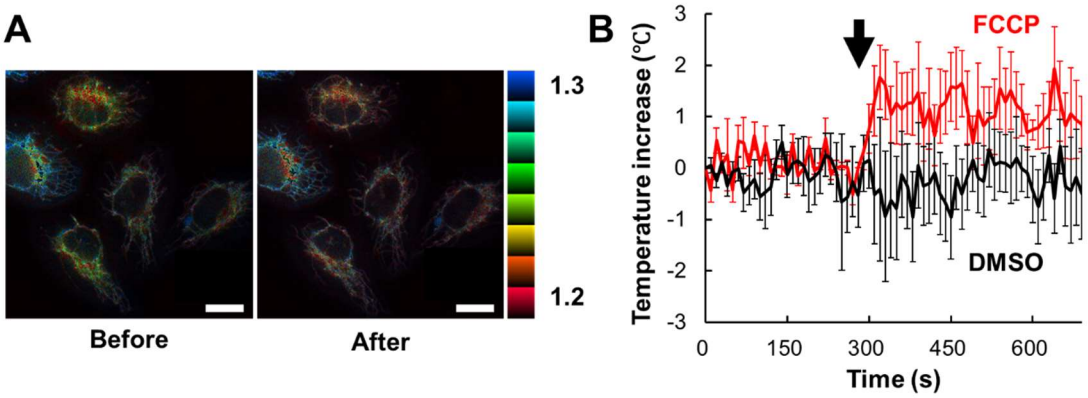

Figure 48. Monitoring the heat production in mitochondria by the treatment of an uncoupling reagent, FCCP. (A) Pseudo-colored ratio images of HeLa cell expressing mito-B-gTEMP before (left) and after (right) treatment with FCCP (10 μM). (B) Plots of temperature increase in mitochondria against time. The temperature increase was estimated by the calibration curve in the **Figure 49**, where B-gTEMP was localized in mitochondria. The arrow indicates the treatment of 10 μM of FCCP (n = 5) or DMSO (n = 6). The medium temperature was 37 °C. The scale bars, 20 μm. Data are mean ± SD.

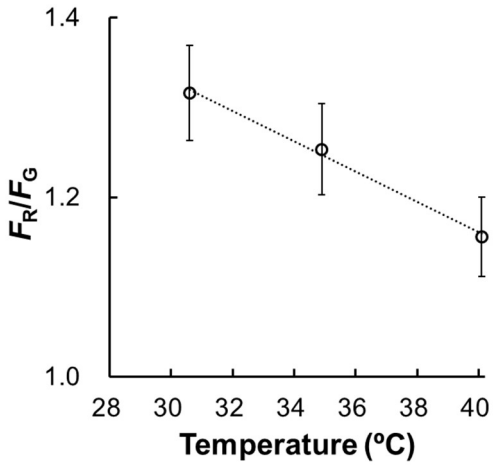

Figure 49. A plot of fluorescence ratio of mito-B-gTEMP in fixed HeLa cells as a function of temperature. B-gTEMP was fused to a duplex of mitochondria signaling peptide (sCOX8) so as to be localized in mitochondria. A slope from the linear regression was calculated to be −0.0169/°C (R^2 = 0.9954). Data are mean ± SD (n = 25).

3.3.7 Temperature in the nucleus and cytoplasm of live HeLa cells

There has been a debate over heterogeneous temperature distribution in cells[56-59], and specifically, there have been several reports which suggested temperature difference between cytoplasm and nucleus[15,19,22,81]. With B-gTEMP, I found that the values of the ratio F_R/F_G of B-gTEMP in the nucleus and cytoplasm were measured to be similar (**Figure 50**), suggesting their temperatures would be almost the same, consistent with the result of ELP-TEMP in **Chapter 2**.

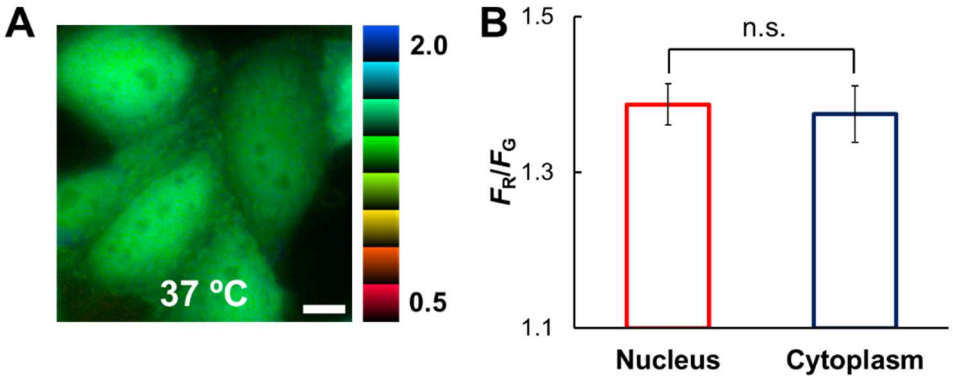

Figure 50. Investigation of fluorescence ratio of B-gTEMP between the nucleus and cytoplasm in live HeLa cells. (A) A pseudo-colored ratio image of B-gTEMP. (B) Comparison of F_R/F_G of B-gTEMP between the nucleus and cytoplasm. n.s represents not significant (two-tailed Student's *t*-test, $p = 0.13$). The temperature was 37 °C. Scale bar, 20 μm. Data are mean ± SD ($n = 30$).

3.4 Summary

B-gTEMP was successfully developed to be an improved version of gTEMP in which temperature imaging can be performed with more advantageous than gTEMP as following. First, B-gTEMP used visible light excitation, and this allowed temperature imaging with greatly-reduced phototoxicity and low background autofluorescence compared to temperature imaging with gTEMP utilizing UV excitation. Second, because B-gTEMP is made up of mNG and tdT, which are much brighter than Sirius and mT-Sap in gTEMP, cell imaging with B-gTEMP requires much less power of irradiation or shorter exposure time than that with gTEMP. Additionally, due to the brightness of mNG and tdT, cell imaging with B-gTEMP achieved high signal-to-background and temperature resolution compared to that of gTEMP. Third, B-gTEMP would be more specific to temperature than gTEMP, as B-gTEMP showed a little dependence on macromolecular crowding and gTEMP showed a significant dependence on macromolecular crowding. Fourth, since B-gTEMP was likely to be more resistant to photobleaching than gTEMP, B-gTEMP would be more useful for long-term temperature imaging than gTEMP. In addition, B-gTEMP had an average S_T of −2.2 ± 1.2%/°C, comparable to that of gTEMP (2.6%/°C[15]). Furthermore, temperature measurement with B-gTEMP was insignificantly affected by factors such as ionic strength, salts, pH, self-concentration as long as the solution was near to physiological conditions. It should note that temperature measurement with B-gTEMP was not affected by macromolecular crowding and self-concentration, which were factors that influenced the temperature measurement with ELP-TEMP. Thus, B-gTEMP is a useful GETI showing high specificity to temperature comparing to gTEMP and ELP-TEMP. I successfully demonstrated temperature-sensing performance of B-gTEMP in live cells. B-gTEMP showed a response to temperature in live HeLa cells with a S_T of −1.8 ± 0.1 %/°C (in a range of 37–40 °C) and δT of 0.5–0.8 °C. Using B-gTEMP, I demonstrated its applicability to monitor the temperature rises inside HeLa cells induced by a local temperature heat spot. Although the S_T of B-gTEMP was lower than that of ELP-TEMP, B-gTEMP showed a linear response to temperature in a wider temperature detection range from 15 to 50 °C and a faster temperature response speed than that of ELP-TEMP. In addition, I demonstrated the applicability of B-gTEMP to measure heat production in mitochondria induced by the stimulation of an uncoupling reagent. Furthermore, I investigated the temperature between the nucleus and cytoplasm

with B-gTEMP in live HeLa cells, and I found that their temperatures were almost the same within the error of the measurement, which was consistent with the result of ELP-TEMP in **Chapter 2**.

CHAPTER 4
CONCLUSION AND PERSPECTIVES

4.1 Conclusion

In this thesis, I report the development of ELP-TEMP and B-gTEMP for temperature imaging in live mammalian cells. For ELP-TEMP, I successfully exploited ELP as a temperature-sensing domain and FRET technique to develop the first FRET-based GETI for highly-sensitive temperature imaging in live cells. Although I found that ELP-TEMP was sensitive to other factors such as self-concentration and macromolecular crowding, by properly calibrating, I managed to correct the output of ELP-TEMP to measure temperature at the sub-organelle scale. In live HeLa cells, ELP-TEMP showed a response to temperature from 33 to 40 °C with a maximum S_T of 45.1 ± 8.1%/°C, which was the highest ever S_T among the existing fluorescent nanothermometers. I demonstrated temperature-sensing performance of ELP-TEMP to monitor quick temperature rises induced by a local heat spot, even if the temperature difference was as small as < 1 °C. Additionally, I visualized heat production from Ca^{2+} influx induced by ionomycin stimulation with ΔT = 1.0 ± 0.8 °C and ΔT = 1.5 ± 0.7 °C in the nucleus and cytoplasm, respectively. Furthermore, when I observed HeLa cells stably expressing ELP-TEMP with a confocal microscope, I found a difference in fluorescence ratios of ELP-TEMP between the nucleus and cytoplasm. However, by correcting ELP-TEMP concentration dependence of the temperature response of ELP-TEMP, the temperatures in the nucleus and cytoplasm were indistinguishable, suggesting that the difference in fluorescence ratios between the nucleus and cytoplasm was due to difference in ELP-TEMP concentrations between them.

On the other hand, B-gTEMP was successfully developed as a chimera of mNG and tdT with different temperature sensitivities. In comparison to its parental gTEMP, B-gTEMP showed superior in brightness due to the brightness of mNG and tdT, which are ones of bright FPs. This allowed B-gTEMP to be excited with short exposure time or low power of excitation without losing its temperature resolution. Additionally, because B-gTEMP utilized blue excitation light, the imaging in live cell could be performed with lower phototoxicity and autofluorescence background than gTEMP that utilized UV

excitation. In comparison to ELP-TEMP, temperature measurement with B-gTEMP was not affected by macromolecular crowding, self-concentration, which were the factors influenced the temperature measurement of ELP-TEMP, and B-gTEMP showed faster response speed than ELP-TEMP. Using B-gTEMP, I successfully visualized quick temperature changes induced by a local heat spot and measured the heat production in mitochondria by treatment with an uncoupling reagent. Furthermore, I investigated the temperature between the nucleus and cytoplasm of HeLa cell and confirmed that the temperature was almost the same between them within the temperature resolution of the measurement, consistent with the result of ELP-TEMP.

4.2 Perspectives

4.2.1 New versions of ELP-TEMP with different temperature-response ranges

I have showed that, by changing the polypeptide length of the ELP moiety and the guest residue in the pentapeptide, the temperature response of ELP-TEMP can be optimized to fit the physiological temperature of mammalian cells. Thus, by further modifying the length of ELP moiety, a new version of ELP-TEMP with a different temperature response range can be developed for a wide range of different applications such as temperature imaging in medaka fish, whose optimum temperature for rearing was reported at 28 °C[95], some plants growing with an optimum temperature range of 20–30 °C[96], or thermophilic bacteria that tolerate a wide temperature of 20–80 °C[97] .

4.2.2 Development of bioluminescent ELP-TEMP

Although FP-based GETIs has demonstrated their usefulness in temperature imaging in live cells, the irradiation of excitation may have caused phototoxicity, autofluorescence background, and photobleaching of the chromophores. However, these limitations would be overcome by utilizing bioluminescent proteins, whose luminescence is generated from a biochemical reaction between a luciferase and its substrate. There have been a number of bioluminescent-based indicators using a combination of NanoLuc[98], the brightest luciferase, and Venus, a yellow FP[70,99]. Thus, by replacing mT in ELP-TEMP with

NanoLuc, a new version of bioluminescent ELP-TEMP can be developed, and this would be the first bioluminescent GETI that has not been reported previously.

4.2.3 *In vivo* temperature imaging

Photothermal therapy (PTT) utilizes heat, which is often generated by pulsed near infrared laser into photosensitizing agents such as gold nanoparticles, to thermally ablate cancer tumors[100]. In this case, real-time measurement of temperature increase of the area surrounding the laser irradiation is essential to minimize the heat damage to the healthy tissue. Thus, an animal model that allows real-time temperature measurement is of great demand to optimize the dose of heat and treatment time before applying in clinical practice. In **Figure 51,** I showed a preliminary result of whole body imaging of nude mice with the injection of B-gTEMP purified protein in the blood vessel. I could detect the fluorescence signal from mNG and tdT to derive a ratio imaging (**Figure 51A)**. In contrast, a nude mouse without injection of B-gTEMP showed low fluorescence signal for both mNG and tdT that should be attributed to autofluorescence (**Figure 51B)**. Although this just a preliminary data, whether the fluorescence ratio reflects the temperature is needed to verify in the future. If I could measure temperature in mice with B-gTEMP, I would create transgenic mice expressing B-gTEMP and demonstrate its practical for photothermal therapy.

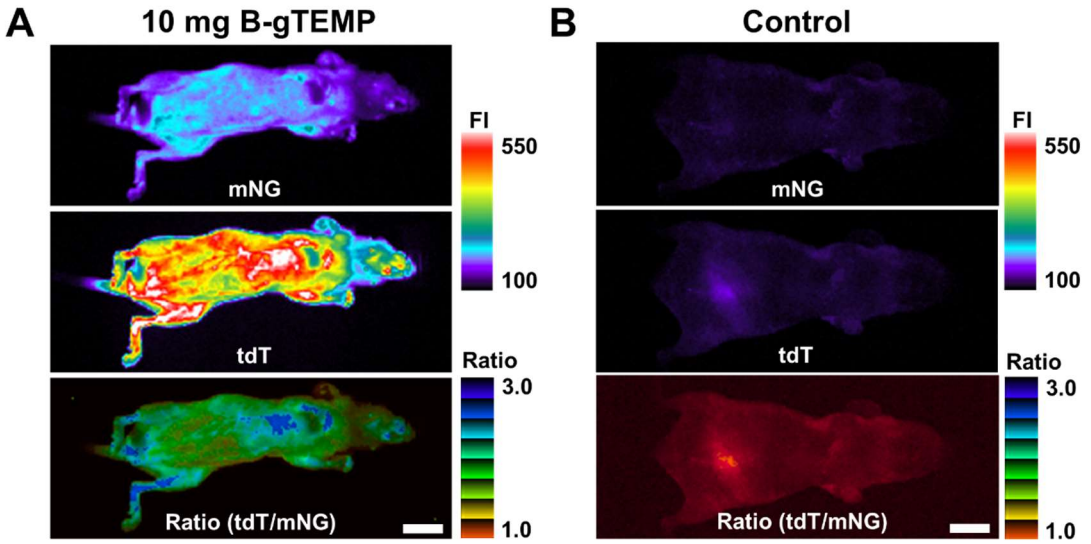

Figure 51. Preliminary data of whole body imaging of nude mice injected with (A) purified B-gTEMP in the blood vessel and (B) control (without B-gTEMP). Nude mice (BALB/cSIc-nu/w, 5-week age, female, 14–19 g in weight obtained from JSLC company, Japan) was injected with 10 mg B-gTEMP in a 500 mL Ringer's solution into the blood vessel. Fluorescence images were captured by EMCCD camera (iXon, ANDOR) with bandpass filters of FF03-525/50 (Semrock) and FF01-593/LP (Semrock) for mNG and tdT, respectively. The exposure time was 10 ms and binning was 1x1 pixels. The excitation light was 470 nm. Color bars indicate fluorescence intensity (FI) or ratio. Scale bar, 1 cm.

4.2.4 My viewpoint on "the 10^5 gap issue"

In this study, I found that temperature measurement with ELP-TEMP was affected by other factors such as self-concentration and macromolecular crowding, and that of gTEMP was also affected by macromolecular crowding, which is a factor that has not been tested in most of fluorescent nanothermometers[3,15,22,23,31,32]. Other temperature indicators involving conformation change of polymer chains or polypeptides should also be susceptible to macromolecular crowding in temperature imaging, which may cause misinterpretation. Regarding the single-cell thermometry with temperature indicators, Baffou *et al.* previously criticized the experimental results obtained by FNT showing a temperature increase by >1 °C that would exceed their theoretical calculation of

temperature changes in single cells by serval orders of magnitude[56]. They pointed out that temperature measurement with fluorescent nanothermometers would have suffered from other factors[56] except for temperature. Accordingly, my results are likely to agree with Baffou *et al.* study in the standpoint of non-specificity of fluorescent nanothermometers to temperature.

Baffou *et al.* argument, however, has been challenged by recent results of non-fluorescent nanothermometry. For examples, Yang *et al.* developed a built-in high-performance micro-thermocouple arrays and a temperature-stabilized system to monitor local temperature of adherent human hepatoblastoma (HepG2) cells under unstimulated condition for days, and found that cellular temperature frequently fluctuated by 60 mK and a maximum increment of 285 mK[101]. In addition, Inomata *et al.* developed a microthermistor to measure single cultured COS7 cells and detected temperature increment by 1 °C in an order of minutes by stimulating with a chemical drug[102]. Furthermore, short-term temperature variations were observed in unstimulated cells with large amplitudes up to 0.8 °C when culturing at 37 °C[102]. Rajagopal *et al.* employed a microthermocouple to measure intracellular temperature increase in the perinuclear cytoplasm enriched with mitochondria of neurons from the seaslug *Aplysia californica*[12]. By stimulating with an uncoupling reagent, the authors detected temperature spikes of ~7.5 °C that showed a rapid decay of ~4.8 °C over ~1 s followed by a slower decay over ~17 s[12]. Such results from non-fluorescent nanothermometry would indicate that there is local temperature fluctuation in single cells that can be measureable.

Perhaps the gap between theoretical and experimental values in single-cell thermometry may be uncovered by reconsidering the values of parameters in the theoretical calculation[82]. In a great attempt, Suzuki group[25] recently utilized a nanoheater/nanothermometer hybrid to measure the intracellular thermal conductivity of HeLa and MCF-7 cells and reported the value of 0.11 ± 0.04 $Wm^{-1}K^{-1}$, which is significantly smaller than the value using the theoretical calculation[56] of 1 $Wm^{-1}K^{-1}$. Also, it should be noticed that in the calculation, Baffou *et al.* estimated that the glucose of cells has will be consumed up in a few seconds in order to rise the temperature to 1 °C[56]. However, this consideration assumes an unrealistic condition in which the cell does not continuously take up glucose as Suzuki *et al.*[57] have pointed out in a reply to the critique. In my experiment, when I stimulated HeLa cells with an ionomycin-induced Ca^{2+} influx,

I detected a temperature increase $\Delta T \sim 1.5$ °C in the cytoplasm with a delay of ~120 s, which may be compatible with a presumption by Suzuki *et al.*[57] that an intracellular temperature increase relative to the environment under stimulation could be sustained by continued glucose uptake. However, to confirm the glucose uptake during ionomycin stimulation, in the future, I will examine this experiment using glucose uptake assay with fluorescent glucose analog (2-NBDG)[67,103] together with the stimulation of ionomycin.

To conclude, Baffou *et al.* may correct only if the cells in the steady-state under unstimulated condition. However, under the stimulated condition, I agree with Suzuki *et al.* that cells can rise intracellular temperature to ~1.0 °C higher than the medium temperature.

REFERENCES

1 Choi, J. *et al.* Probing and manipulating embryogenesis via nanoscale thermometry and temperature control. *Proc. Natl. Acad. Sci. U. S. A.* **117**, 14636-14641, doi:10.1073/pnas.1922730117 (2020).

2 Riedel, C. *et al.* The heat released during catalytic turnover enhances the diffusion of an enzyme. *Nature* **517**, 227, doi:10.1038/nature14043 (2014).

3 Kamei, Y. *et al.* Infrared laser–mediated gene induction in targeted single cells in vivo. *Nat. Methods* **6**, 79, doi:10.1038/nmeth.1278 (2008).

4 Lowell, B. B. & Spiegelman, B. M. Towards a molecular understanding of adaptive thermogenesis. *Nature* **404**, 652, doi:10.1038/35007527 (2000).

5 CANNON, B. & NEDERGAARD, J. Brown Adipose Tissue: Function and Physiological Significance. *Physiol. Rev.* **84**, 277-359, doi:10.1152/physrev.00015.2003 (2004).

6 Nowack, J., Giroud, S., Arnold, W. & Ruf, T. Muscle Non-shivering Thermogenesis and Its Role in the Evolution of Endothermy. *Front. Physiol.* **8**, doi:10.3389/fphys.2017.00889 (2017).

7 Rowland, L. A., Bal, N. C. & Periasamy, M. The role of skeletal-muscle-based thermogenic mechanisms in vertebrate endothermy. *Biol. Rev. Camb. Philos. Soc.* **90**, 1279-1297, doi:10.1111/brv.12157 (2015).

8 Whittle, A. J., López, M. & Vidal-Puig, A. Using brown adipose tissue to treat obesity – the central issue. *Trends Mol. Med.* **17**, 405-411, doi:10.1016/j.molmed.2011.04.001 (2011).

9 Song, N.-J., Chang, S.-H., Li, D. Y., Villanueva, C. J. & Park, K. W. Induction of thermogenic adipocytes: molecular targets and thermogenic small molecules. *Experimental &Amp; Molecular Medicine* **49**, e353, doi:10.1038/emm.2017.70 (2017).

10 Wang, X.-d., Wolfbeis, O. S. & Meier, R. J. Luminescent probes and sensors for temperature. *Chem. Soc. Rev.* **42**, 7834-7869, doi:10.1039/C3CS60102A (2013).

11 Wang, C. *et al.* Determining intracellular temperature at single-cell level by a novel thermocouple method. *Cell Res.* **21**, 1517, doi:10.1038/cr.2011.117 (2011).

12 Rajagopal, M. C. *et al.* Transient heat release during induced mitochondrial proton uncoupling. *Commun. Biol.* **2**, 279, doi:10.1038/s42003-019-0535-y (2019).

13 Bai, T. & Gu, N. Micro/Nanoscale Thermometry for Cellular Thermal Sensing. *Small* **12**, 4590-4610, doi:10.1002/smll.201600665 (2016).

14 Nakano, M. & Nagai, T. Thermometers for monitoring cellular temperature. *J. Photochem. Photobiol., C* **30**, 2-9, doi:10.1016/j.jphotochemrev.2016.12.001 (2017).

15 Nakano, M. *et al.* Genetically encoded ratiometric fluorescent thermometer with wide range and rapid response. *PLoS One* **12**, e0172344, doi:10.1371/journal.pone.0172344 (2017).

16 Arai, S. *et al.* Mitochondria-targeted fluorescent thermometer monitors intracellular temperature gradient. *Chem. Commun. (Camb.)* **51**, 8044-8047, doi:10.1039/c5cc01088h (2015).

17 Ferdinandus *et al.* Facilely Fabricated Luminescent Nanoparticle Thermosensor for Real-Time Microthermography in Living Animals. *ACS Sens.* **1**, 1222-1227, doi:10.1021/acssensors.6b00320 (2016).

18 Kucsko, G. *et al.* Nanometre-scale thermometry in a living cell. *Nature* **500**, 54-58, doi:10.1038/nature12373 (2013).

19 Okabe, K. *et al.* Intracellular temperature mapping with a fluorescent polymeric thermometer and fluorescence lifetime imaging microscopy. *Nat. Commun.* **3**, 705, doi:10.1038/ncomms1714 (2012).

20 Ke, G. *et al.* l-DNA Molecular Beacon: A Safe, Stable, and Accurate Intracellular Nano-thermometer for Temperature Sensing in Living Cells. *J. Am. Chem. Soc.* **134**, 18908-18911, doi:10.1021/ja3082439 (2012).

21 Tanimoto, R. *et al.* Detection of Temperature Difference in Neuronal Cells. *Sci. Rep.* **6**, 22071, doi:10.1038/srep22071 (2016).

22 Hayashi, T., Fukuda, N., Uchiyama, S. & Inada, N. A Cell-Permeable Fluorescent Polymeric Thermometer for Intracellular Temperature Mapping in Mammalian Cell Lines. *PLoS One* **10**, e0117677, doi:10.1371/journal.pone.0117677 (2015).

23 Savchuk, O. A., Silvestre, O. F., Adão, R. M. R. & Nieder, J. B. GFP fluorescence peak fraction analysis based nanothermometer for the assessment of exothermal

mitochondria activity in live cells. *Sci. Rep.* **9**, 7535, doi:10.1038/s41598-019-44023-7 (2019).

24 Chrétien, D. *et al.* Mitochondria are physiologically maintained at close to 50 °C. *PLoS Biol.* **16**, e2003992, doi:10.1371/journal.pbio.2003992 (2018).

25 Sotoma, S. *et al.* In situ measurements of intracellular thermal conductivity using heater-thermometer hybrid diamond nanosensors. *Sci. Adv.* **7**, eabd7888, doi:10.1126/sciadv.abd7888 (2021).

26 Song, P. *et al.* Heat transfer and thermoregulation within single cells revealed by transient plasmonic imaging. *Chem*, doi:10.1016/j.chempr.2021.02.027 (2021).

27 Donner, J. S. *et al.* Imaging of Plasmonic Heating in a Living Organism. *ACS Nano* **7**, 8666-8672, doi:10.1021/nn403659n (2013).

28 Ximendes, E. C. *et al.* In Vivo Ischemia Detection by Luminescent Nanothermometers. *Adv. Healthcare Mater.* **6**, 1601195, doi:10.1002/adhm.201601195 (2017).

29 Santos, H. D. A. *et al.* In Vivo Early Tumor Detection and Diagnosis by Infrared Luminescence Transient Nanothermometry. *Adv. Funct. Mater.* **28**, 1803924, doi:10.1002/adfm.201803924 (2018).

30 Xu, M. *et al.* Ratiometric nanothermometer in vivo based on triplet sensitized upconversion. *Nat. Commun.* **9**, 2698, doi:10.1038/s41467-018-05160-1 (2018).

31 Donner, J. S., Thompson, S. A., Kreuzer, M. P., Baffou, G. & Quidant, R. Mapping Intracellular Temperature Using Green Fluorescent Protein. *Nano Lett.* **12**, 2107-2111, doi:10.1021/nl300389y (2012).

32 Kiyonaka, S. *et al.* Genetically encoded fluorescent thermosensors visualize subcellular thermoregulation in living cells. *Nat. Methods* **10**, 1232-1239, doi:10.1038/nmeth.2690 (2013).

33 Arai, S., Lee, S.-C., Zhai, D., Suzuki, M. & Chang, Y. T. A Molecular Fluorescent Probe for Targeted Visualization of Temperature at the Endoplasmic Reticulum. *Sci. Rep.* **4**, 6701, doi:10.1038/srep06701 (2014).

34 Homma, M., Takei, Y., Murata, A., Inoue, T. & Takeoka, S. A ratiometric fluorescent molecular probe for visualization of mitochondrial temperature in living cells. *Chem. Commun.* **51**, 6194-6197, doi:10.1039/C4CC10349A (2015).

35 Huang, Z., Li, N., Zhang, X. & Xiao, Y. Mitochondria-Anchored Molecular Thermometer Quantitatively Monitoring Cellular Inflammations. *Anal. Chem.* **93**, 5081–5088, doi:10.1021/acs.analchem.0c04547 (2021).

36 Suzuki, M., Tseeb, V., Oyama, K. & Ishiwata, S. i. Microscopic detection of thermogenesis in a single HeLa cell. *Biophys. J.* **92**, L46-L48, doi:10.1529/biophysj.106.098673 (2007).

37 Sou, K., Chan, L. Y., Arai, S. & Lee, C.-L. K. Highly cooperative fluorescence switching of self-assembled squaraine dye at tunable threshold temperatures using thermosensitive nanovesicles for optical sensing and imaging. *Sci. Rep.* **9**, 17991, doi:10.1038/s41598-019-54418-1 (2019).

38 Shang, L., Stockmar, F., Azadfar, N. & Nienhaus, G. U. Intracellular Thermometry by Using Fluorescent Gold Nanoclusters. *Angew. Chem. Int. Ed.* **52**, 11154-11157, doi:10.1002/anie.201306366 (2013).

39 Sekiyama, S. *et al.* Temperature Sensing of Deep Abdominal Region in Mice by Using Over-1000 nm Near-Infrared Luminescence of Rare-Earth-Doped NaYF4 Nanothermometer. *Sci. Rep.* **8**, 16979, doi:10.1038/s41598-018-35354-y (2018).

40 Gota, C., Okabe, K., Funatsu, T., Harada, Y. & Uchiyama, S. Hydrophilic Fluorescent Nanogel Thermometer for Intracellular Thermometry. *J. Am. Chem. Soc.* **131**, 2766-2767, doi:10.1021/ja807714j (2009).

41 Oyama, K. *et al.* Walking nanothermometers: spatiotemporal temperature measurement of transported acidic organelles in single living cells. *Lab on a Chip* **12**, 1591-1593, doi:10.1039/C2LC00014H (2012).

42 Takei, Y. *et al.* A Nanoparticle-Based Ratiometric and Self-Calibrated Fluorescent Thermometer for Single Living Cells. *ACS Nano* **8**, 198-206, doi:10.1021/nn405456e (2014).

43 Oyama, K. *et al.* Single-cell temperature mapping with fluorescent thermometer nanosheets. *J. Gen. Physiol.* **152**, doi:10.1085/jgp.201912469 (2020).

44 Su, X. *et al.* Lifetime-based nanothermometry in vivo with ultra-long-lived luminescence. *Chem. Commun.*, doi:10.1039/D0CC04459H (2020).

45 Wu, Y. *et al.* Novel Ratiometric Fluorescent Nanothermometers Based on Fluorophores-Labeled Short Single-Stranded DNA. *ACS Applied Materials & Interfaces* **9**, 11073-11081, doi:10.1021/acsami.7b01554 (2017).

46 Bednarkiewicz, A. *et al.* Luminescence based temperature bio-imaging: Status, challenges, and perspectives. *Applied Physics Reviews* **8**, 011317, doi:10.1063/5.0030295 (2021).

47 Maestro, L. M. *et al.* CdTe Quantum Dots as Nanothermometers: Towards Highly Sensitive Thermal Imaging. **7**, 1774-1778, doi:10.1002/smll.201002377 (2011).

48 dos Santos, A. M. Thermal Effect on Aequorea Green Fluorescent Protein Anionic and Neutral Chromophore Forms Fluorescence. *Journal of Fluorescence* **22**, 151-154, doi:10.1007/s10895-011-0941-0 (2012).

49 Bradac, C., Lim, S. F., Chang, H.-C. & Aharonovich, I. Optical Nanoscale Thermometry: From Fundamental Mechanisms to Emerging Practical Applications. *Adv. Opt. Mater.* **8**, 2000183, doi:10.1002/adom.202000183 (2020).

50 Vyšniauskas, A. *et al.* Cyclopropyl Substituents Transform the Viscosity-Sensitive BODIPY Molecular Rotor into a Temperature Sensor. *ACS Sens.*, doi:10.1021/acssensors.0c02275 (2021).

51 Meng, L. *et al.* TICT-Based Near-Infrared Ratiometric Organic Fluorescent Thermometer for Intracellular Temperature Sensing. *ACS Applied Materials & Interfaces*, doi:10.1021/acsami.0c03714 (2020).

52 Kinosita, K., Jr *et al.* Dual-view microscopy with a single camera: real-time imaging of molecular orientations and calcium. *J. Cell Biol.* **115**, 67-73, doi:10.1083/jcb.115.1.67 %J Journal of Cell Biology (1991).

53 Maksimov, E. G. *et al.* A genetically encoded fluorescent temperature sensor derived from the photoactive Orange Carotenoid Protein. *Sci. Rep.* **9**, 8937, doi:10.1038/s41598-019-45421-7 (2019).

54 Itoh, H. *et al.* Direct organelle thermometry with fluorescence lifetime imaging microscopy in single myotubes. *Chem. Commun.* **52**, 4458-4461, doi:10.1039/C5CC09943A (2016).

55 Kriszt, R. *et al.* Optical visualisation of thermogenesis in stimulated single-cell brown adipocytes. *Sci. Rep.* **7**, 1383, doi:10.1038/s41598-017-00291-9 (2017).

56 Baffou, G., Rigneault, H., Marguet, D. & Jullien, L. A critique of methods for temperature imaging in single cells. *Nat. Methods* **11**, 899, doi:10.1038/nmeth.3073 (2014).

57 Suzuki, M., Zeeb, V., Arai, S., Oyama, K. & Ishiwata, S. i. The 105 gap issue between calculation and measurement in single-cell thermometry. *Nat. Methods* **12**, 802, doi:10.1038/nmeth.3551 (2015).

58 Kiyonaka, S. *et al.* Validating subcellular thermal changes revealed by fluorescent thermosensors. *Nat. Methods* **12**, 801, doi:10.1038/nmeth.3548 (2015).

59 Baffou, G., Rigneault, H., Marguet, D. & Jullien, L. Reply to: "Validating subcellular thermal changes revealed by fluorescent thermosensors" and "The 105 gap issue between calculation and measurement in single-cell thermometry&quot. *Nat. Methods* **12**, 803, doi:10.1038/nmeth.3552 (2015).

60 Gagner, J. E., Kim, W. & Chaikof, E. L. Designing protein-based biomaterials for medical applications. *Acta Biomater.* **10**, 1542-1557, doi:10.1016/j.actbio.2013.10.001 (2014).

61 Varanko, A. K., Su, J. C. & Chilkoti, A. Elastin-Like Polypeptides for Biomedical Applications. *Annu. Rev. Biomed. Eng.* **22**, 343-369, doi:10.1146/annurev-bioeng-092419-061127 (2020).

62 Urry, D. W. *et al.* Temperature of polypeptide inverse temperature transition depends on mean residue hydrophobicity. *J. Am. Chem. Soc.* **113**, 4346-4348, doi:10.1021/ja00011a057 (1991).

63 Pastuszka, M. K. *et al.* A Tunable and Reversible Platform for the Intracellular Formation of Genetically Engineered Protein Microdomains. *Biomacromolecules* **13**, 3439-3444, doi:10.1021/bm301090x (2012).

64 Chen, Z., Ding, Z. Y., Zhang, G. Y., Tian, L. L. & Zhang, X. J. Construction of Thermo-Responsive Elastin-Like Polypeptides (ELPs)-Aggregation-Induced-Emission (AIE) Conjugates for Temperature Sensing. *Molecules* **23**, 1725, doi:10.3390/molecules23071725 (2018).

65 Lakowicz, J. R. *Principles of Fluorescence Spectroscopy*. 3 edn, (Springer, Boston, MA, 2006).

66 Horikawa, K. *et al.* Spontaneous network activity visualized by ultrasensitive Ca2+ indicators, yellow Cameleon-Nano. *Nat. Methods* **7**, 729, doi:10.1038/nmeth.1488 (2010).

67 Maeshima, K. *et al.* A Transient Rise in Free Mg2+ Ions Released from ATP-Mg Hydrolysis Contributes to Mitotic Chromosome Condensation. *Curr. Biol.* **28**, 444-451.e446, doi:10.1016/j.cub.2017.12.035 (2018).

68 Bischof, H. *et al.* Novel genetically encoded fluorescent probes enable real-time detection of potassium in vitro and in vivo. *Nat. Commun.* **8**, 1422, doi:10.1038/s41467-017-01615-z (2017).

69 Burgstaller, S. *et al.* pH-Lemon, a Fluorescent Protein-Based pH Reporter for Acidic Compartments. *ACS Sens.* **4**, 883-891, doi:10.1021/acssensors.8b01599 (2019).

70 Inagaki, S. *et al.* Genetically encoded bioluminescent voltage indicator for multi-purpose use in wide range of bioimaging. *Sci. Rep.* **7**, 42398, doi:10.1038/srep42398 (2017).

71 Boersma, A. J., Zuhorn, I. S. & Poolman, B. A sensor for quantification of macromolecular crowding in living cells. *Nat. Methods* **12**, 227-229, doi:10.1038/nmeth.3257 (2015).

72 Goedhart, J. *et al.* Structure-guided evolution of cyan fluorescent proteins towards a quantum yield of 93%. *Nat. Commun.* **3**, 751, doi:10.1038/ncomms1738 (2012).

73 Nagai, T. *et al.* A variant of yellow fluorescent protein with fast and efficient maturation for cell-biological applications. *Nat. Biotechnol.* **20**, 87-90, doi:10.1038/nbt0102-87 (2002).

74 Tang, N. C. & Chilkoti, A. Combinatorial codon scrambling enables scalable gene synthesis and amplification of repetitive proteins. *Nature Mater.* **15**, 419, doi:10.1038/nmat4521 (2016).

75 Zhao, Y. *et al.* An expanded palette of genetically encoded Ca(2)(+) indicators. *Science* **333**, 1888-1891, doi:10.1126/science.1208592 (2011).

76 MacEwan, S. R. & Chilkoti, A. Elastin-like polypeptides: biomedical applications of tunable biopolymers. *Biopolymers* **94**, 60-77, doi:10.1002/bip.21327 (2010).

77 Li, N. K., Quiroz, F. G., Hall, C. K., Chilkoti, A. & Yingling, Y. G. Molecular Description of the LCST Behavior of an Elastin-Like Polypeptide. *Biomacromolecules* **15**, 3522-3530, doi:10.1021/bm500658w (2014).

78 Trabbic-Carlson, K. *et al.* Effect of protein fusion on the transition temperature of an environmentally responsive elastin-like polypeptide: a role for surface

hydrophobicity? *Protein Eng. Des. Sel.* **17**, 57-66, doi:10.1093/protein/gzh006 (2004).

79 Inoue, Y. *et al.* Single Carbon Nanotube-Based Reversible Regulation of Biological Motor Activity. *ACS Nano* **9**, 3677-3684, doi:10.1021/nn505607c (2015).

80 de Meis, L., Arruda, A. P. & Carvalho, D. P. Role of Sarco/Endoplasmic Reticulum Ca2+-ATPase in Thermogenesis. *Biosci. Rep.* **25**, 181-190, doi:10.1007/s10540-005-2884-7 (2005).

81 Sugimura, T., Kajimoto, S. & Nakabayashi, T. Label-free imaging of intracellular temperature using O-H stretching Raman band of water. *Angew. Chem. Int. Ed.* **59**, 775-7760, doi:10.1002/anie.201915846 (2020).

82 Suzuki, M. & Plakhotnik, T. The challenge of intracellular temperature. *Biophys. Rev.* **12**, 593–600, doi:10.1007/s12551-020-00683-8 (2020).

83 Shi, W., Li, X. & Ma, H. A Tunable Ratiometric pH Sensor Based on Carbon Nanodots for the Quantitative Measurement of the Intracellular pH of Whole Cells. *Angew. Chem. Int. Ed.* **51**, 6432-6435, doi:10.1002/anie.201202533 (2012).

84 Kemp, R. B. Calorimetric studies of heat flux in animal cells. *Thermochim. Acta* **193**, 253-267, doi:10.1016/0040-6031(91)80187-N (1991).

85 Dedkova, E. N., Sigova, A. A. & Zinchenko, V. P. Mechanism of action of calcium ionophores on intact cells: ionophore-resistant cells. *Membrane & cell biology* **13**, 357-368 (2000).

86 Tomosugi, W. *et al.* An ultramarine fluorescent protein with increased photostability and pH insensitivity. *Nat. Methods* **6**, 351-353, doi:10.1038/nmeth.1317 (2009).

87 Shaner, N. C. *et al.* A bright monomeric green fluorescent protein derived from Branchiostoma lanceolatum. *Nat. Methods* **10**, 407-409, doi:10.1038/nmeth.2413 (2013).

88 Schaefer, P. M., Kalinina, S., Rueck, A., von Arnim, C. A. F. & von Einem, B. NADH Autofluorescence—A Marker on its Way to Boost Bioenergetic Research. *Cytometry Part A* **95**, 34-46, doi:10.1002/cyto.a.23597 (2019).

89 Shaner, N. C. *et al.* Improved monomeric red, orange and yellow fluorescent proteins derived from Discosoma sp. red fluorescent protein. *Nat. Biotechnol.* **22**, 1567-1572, doi:10.1038/nbt1037 (2004).

90 Kenworthy, A. K. Imaging protein-protein interactions using fluorescence resonance energy transfer microscopy. *Methods* **24**, 289-296, doi:10.1006/meth.2001.1189 (2001).

91 Wallberg, F., Tenev, T. & Meier, P. Time-Lapse Imaging of Cell Death. *Cold Spring Harbor Protocols* **2016**, pdb.prot087395, doi:10.1101/pdb.prot087395 (2016).

92 Ai, H.-w., Hazelwood, K. L., Davidson, M. W. & Campbell, R. E. Fluorescent protein FRET pairs for ratiometric imaging of dual biosensors. *Nat. Methods* **5**, 401-403, doi:10.1038/nmeth.1207 (2008).

93 Bindels, D. S. *et al.* mScarlet: a bright monomeric red fluorescent protein for cellular imaging. *Nat. Methods* **14**, 53-56, doi:10.1038/nmeth.4074 (2017).

94 Lodish, H. *et al. Molecular Cell Biology*. 5th edn, 253 and 261 (W. H. Freeman: New York,, 2003).

95 Rosemore, B. J. & Welsh, C. A. The Effects of Rearing Density, Salt Concentration, and Incubation Temperature on Japanese Medaka (Oryzias latipes) Embryo Development. *Zebrafish* **9**, 185-190, doi:10.1089/zeb.2012.0744 (2012).

96 Hatfield, J. L. & Prueger, J. H. Temperature extremes: Effect on plant growth and development. *Weather and Climate Extremes* **10**, 4-10, doi:10.1016/j.wace.2015.08.001 (2015).

97 Pandey, A. *et al.* Thermophilic bacteria that tolerate a wide temperature and pH range colonize the Soldhar (95 °C) and Ringigad (80 °C) hot springs of Uttarakhand, India. *Ann. Microbiol.* **65**, 809-816, doi:10.1007/s13213-014-0921-0 (2015).

98 Hall, M. P. *et al.* Engineered Luciferase Reporter from a Deep Sea Shrimp Utilizing a Novel Imidazopyrazinone Substrate. *ACS Chem. Biol.* **7**, 1848-1857, doi:10.1021/cb3002478 (2012).

99 Suzuki, K. *et al.* Five colour variants of bright luminescent protein for real-time multicolour bioimaging. *Nat. Commun.* **7**, 13718, doi:10.1038/ncomms13718 (2016).

100 Jaque, D. *et al.* Nanoparticles for photothermal therapies. *Nanoscale* **6**, 9494-9530, doi:10.1039/C4NR00708E (2014).

101 Yang, F. *et al.* Measurement of local temperature increments induced by cultured HepG2 cells with micro-thermocouples in a thermally stabilized system. *Sci. Rep.* **7**, 1721, doi:10.1038/s41598-017-01891-1 (2017).

102 Inomata, N., Inaoka, R., Okabe, K., Funatsu, T. & Ono, T. Short-term temperature change detections and frequency signals in single cultured cells using a microfabricated thermistor. *Sensing and Bio-Sensing Research* **20**, 100309, doi:10.1016/j.sbsr.2019.100309 (2020).

103 Yoshioka, K. *et al.* A novel fluorescent derivative of glucose applicable to the assessment of glucose uptake activity of Escherichia coli. *Biochimica et Biophysica Acta (BBA) - General Subjects* **1289**, 5-9, doi:10.1016/0304-4165(95)00153-0 (1996).

ACKNOWLEDGEMENTS

I am using this opportunity to express my gratitude to everyone who supported me throughout the doctoral course. Firstly, I would like to express my deep gratitude to my supervisor Prof. Takeharu Nagai. This thesis could not able to be accomplished without his invaluable guidance, generous supporting, patience, kindness, and enthusiastic encouragement. The door of his office is always opened whenever I run into troubles of my research. Words cannot express my acknowledgement.

I would like to offer my special appreciation to my sub-supervisor specially appointed Assoc. Prof. Tetsuichi Wazawa for his kindness, patience, generosity, valuable and constructive suggestions during the planning and development of this research work. This thesis would not be accomplished without him.

Besides, I would like to thank the rest of my thesis committee members: Prof. Masahiro Ueda (Graduate school of Frontier Biosciences (FBS), Osaka University), Prof. Yasushi Hiraoka (FBS, Osaka University), Prof. Masaru Ishii (FBS, Osaka University), for their insightful comments that would expand my understanding and knowledge.

I would also like to extend my thanks to Assoc. Prof. Tomoki Matsuda, Asst. Prof. Kenji Osabe, Asst. Prof. Mitsuru Hattori, Dr. Kai Lu, Dr. Kazunori Sugiura, Dr. Shun-ichi Fukushima, Dr. Takashi Kanadome at SANKEN, Osaka University for their helpful advice and encouragement, and to all the lab members for their support and helping. I also thank Asst. Prof. Masahiro Nakano for his teaching in the first year of my studying.

My sincere thanks also go to the secretaries, Mrs. Kazuyo Sakai, Mrs. Hiroko Inoue, and Ms. Asako Sakai for their kindness and warm-helping with all the document preparation. I also thank the Japan Government and the Ministry of Education, Culture, Sports, Science, and Technology (MEXT) for financial support by MEXT scholarship.

Finally, I must express my very profound gratitude to my family members, especially my grandpa Vũ Minh Đức who died on June 14th 2021 during my thesis writing, my dad Vũ Đình Hiền, my mom Nguyễn Thị Tin, my brothers Vũ Ngọc An, Vũ Cao Trí, Vũ Hoàng Nhật and sister Vũ Thị Hồng Vy, relatives, friends (particularly CF foundation, Chivas Mãi Mãi Tuổi 18), and my soulmate, Watcharaporn Hoisang, for always staying beside me with all the support and unstoppable encouragement throughout my years of studying and the progress of researching and writing this thesis. Thank you.

LIST OF ACADEMIC ACCOMPLISHMENTS

Publications

1. **Vu Q. C.**, Fukushima S., Wazawa T., and Nagai T., A highly-sensitive genetically encoded temperature indicator exploiting a temperature-responsive elastin-like polypeptide, *Sci. Rep.* **11**, 16519, doi:10.1038/s41598-021-96049-5 (2021).

2. Lu K., **Vu Q. C.**, Matsuda T., and Nagai T., Fluorescent protein-based indicators for functional super-resolution imaging of biomolecular activities in living cells. *Int. J. Mol. Sci.* **20**, 5784, doi:10.3390/ijms20225784 (2019).

Oral presentations

1. **Vu, Q, C.,** Wazawa T., Lu, K., *Nakano* M., and Nagai T., A red-shifted version of genetically encoded ratiometric fluorescent temperature indicator for live-cell imaging with low phototoxicity and high time resolution, *The 29th Annual Meeting of the Bioimaging Society of Japan*, November 20th–21st 2021, Japan
2. **Vu, Q, C.,** Wazawa T., Lu, K., *Nakano* M., and Nagai T., A red-shifted version of genetically encoded ratiometric fluorescent temperature indicator for live-cell imaging with low phototoxicity and high time resolution, 生理学研究所研究会「細胞システム理解のためのシグナル応答原理解明の最前線」, October 3rd–4th 2020, Japan

Poster presentations

1. **Vu, Q, C.,** Wazawa T., and Nagai T., Molecular thermometer based on elastin-like polypeptide, *The 57th Annual Meeting of the Biophysical Society of Japan*, September 24th–26th 2019, Japan
2. **Vu, Q, C.,** Wazawa T., and Nagai T., Intracellular temperature imaging using elastin-like polypeptide thermometer, *Proceedings of 44th Meeting of Japan Society for Laser Microscopy*, July 4th–5th 2019, Japan